

PERTURBATIVE QCD AND THE PARTON STRUCTURE OF THE NUCLEON[†]

WU-KI TUNG

*Michigan State University
E. Lansing, MI 07661, USA*

This review consists of two parts: (i) an introductory exposition of the foundation of perturbative QCD, which underpins the universally used QCD parton picture of high energy interactions; and (ii) a survey of recent progress on the parton structure of the nucleon – through global QCD analysis of a full range of hard scattering processes, using available theoretical tools and experimental measurements. The three key features of perturbative QCD – asymptotic freedom, infrared safety, and factorization – are discussed in some detail, using a pedagogical approach. The review of global QCD analysis emphasizes the non-trivial underlying issues, current uncertainties, and the challenges which await due to the demands of precision standard model studies and new physics searches in the next generation of experiments.

Contents

1	Introduction	3
2	Perturbative QCD and the Simple Parton Model	4
2.1	The experimental evidences of quarks and gluons	4
2.2	The electroweak properties of quark partons	6
2.3	How can the simple quark parton picture be true in a strongly interacting gauge field theory such as QCD?	7
	Asymptotic Freedom in QCD	7
	What is still missing?	8
3	Infrared Safety (IRS) and Basic Tests of QCD	9
3.1	Collinear and soft singularities	9
3.2	Singularities are due to long-distance space-time interactions	11
3.3	Infrared safety and cancellation of IR singularities	12
3.4	IRS quantities in e^+e^- collisions	13
3.5	More quantitative tests of QCD in e^+e^- collisions	14
4	Factorization and the QCD Parton Model	16
4.1	Essential ideas of Factorization in e^+e^- annihilation	17
	Factorization of partonic cross sections	17
	Hadronic cross sections and the QCD Parton Model	19
4.2	Renormalization, factorization, and scale transformations	21
4.3	Factorization in Deep inelastic scattering	22
	The perturbative structure functions	23
	A detailed look at collinear singularity and the physics of factorization – the gluon structure function	24

[†]Based on a contribution to *At the frontier of particle physics—Handbook of QCD*, vol. 2* 887-971, ed. M. Shifman, Pub. World Scientific Publisher, Singapore, New York, 2001; and on lecture notes given at past CTEQ Summer Schools. Some materials in Secs. 3 & 4 are adapted from Ref. 6, by permission from the author.

	Full factorization in NLO and beyond	28
4.4	Parton distribution functions	30
4.5	Scale-dependence of the factorization theorem based parton model	30
4.6	Three faces of the master formula of QCD parton model	31
5	Hard Processes in Hadron Interactions	31
5.1	Deep inelastic scattering	32
5.2	Hadron-hadron collisions in general	33
5.3	Lepton-pair and W/Z production (Drell-Yan processes)	34
5.4	Direct photon production	37
5.5	Inclusive jet production	40
5.6	Heavy quark production	41
	Why is heavy quark production a non-trivial problem in PQCD?	42
	Generalization of the zero-mass QCD parton formalism	43
	Lepto-production of charm and hadro-production of bottom	45
6	Global QCD Analysis and Parton Distributions	47
6.1	Common inputs and relevant issues	47
6.2	Global analysis strategies and procedures	50
6.3	Review of recent parton distribution functions of the nucleon	53
6.4	Uncertainties of PDFs and their predictions	55
	What are current uncertainties on PDFs?	56
	Quantifying uncertainties of PDFs and their physical predictions	59
6.5	Global QCD analysis and the future of HEP	63
	Importance of PDFs for future HEP programs	63
	How can future experiments help global QCD analysis?	65
7	Epilogue	66

1 Introduction

Quantum Chromodynamics (QCD) is the universally accepted theory of strong interaction physics. The theory of QCD has a remarkable simplicity and elegance at the classical level, with its underlying non-Abelian SU(3) color symmetry; and unmatched richness after quantization, as revealed by a whole spectrum of contrasting behaviors over a wide range of energy scales, from confinement to asymptotic freedom, in addition to various possible phase transitions under extreme conditions. But the faith in QCD as a true *physics theory* ultimately is founded, at least up to now, on the successes of perturbative quantum chromodynamics (PQCD) where its wide-ranging predictions are compared to the wealth of experimental data on high energy *hard processes*, accumulated in the last thirty years at a variety of experimental facilities, covering numerous physical processes in lepton-lepton, lepton-hadron, and hadron-hadron collisions.

In the first part of this contribution, we shall try to capture some of the highlights and spirits of this remarkably successful theory of PQCD. As is well known, the unique feature of the underlying quantum field theory which makes the perturbative approach useful in QCD, is *asymptotic freedom*. Equally important are the crucial concepts of *infrared safety* and *factorization*, without which it would not be possible to apply the results of perturbative calculations on partons (quark, gluons, vector bosons, . . . etc.) to the world of observed hadrons, electro-weak bosons, Higgs and other new physics particles. In fact, the proof of factorization establishes the theoretical foundation of the QCD parton model, which provides the basic language, and picture, for describing all high energy interactions involving hadrons nowadays in particle physics.

Because PQCD is already a mature field, there is no need to systematically review its basic formalism and its conventional implementation here. Good textbooks^{1,2,3,4} and reviews^{5,6,7,8} abound both for an introduction to the subject and for comprehensive references. In this part, we shall take an informal and pedagogical approach distinguished by: (i) integrating in the presentation some important experimental evidence and motivation for PQCD; and more importantly, (ii) emphasizing the key features of infrared safety and factorization, from angles different from the formal textbook approaches, with the help of graphical illustrations. We hope, this will complement the conventional, more formal, expositions and add to the understanding of the foundation of the factorization-theorem-based QCD parton model for nonexperts.

The QCD parton model has several interesting facets, all of which are important (cf. Sec. 4.6: *Three faces of . . .*). One of these is that it provides the basis for the *global QCD analysis* of a full range of hard scattering processes, using all available theoretical tools and experimental measurements, to determine the parton distribution functions (PDFs) of hadrons, particularly nucleons. These, in turn, are indispensable input to the wide range of calculations (predictions) on standard model and new physics processes. The second part of this article consists of a survey of current issues on the relevant hard scattering processes, as well as on global analysis of the parton structure of the nucleon. In addition to describing the current status, this part will emphasize the non-trivial underlying issues, the inherent uncertainties, and the challenges which await due to the demands of precision standard model studies and new physics searches in the next generation of experiments.

Together, these two parts aim to provide a useful background for the more adventurous topics on nonperturbative QCD which occupy most of these three volumes of *Handbook of QCD* in honor of Boris Ioffe. Because of the nature of this article, references are introduced only to add to or to extend the presentation; and, in general, more emphasis is put on review articles than on original papers.

2 Perturbative QCD and the Simple Parton Model

QCD is a quantum field theory of quarks and gluons endowed with a non-abelian gauge symmetry group – SU(3) of color. The classical Lagrangian which explicitly exhibits this symmetry is given by the Yang-Mills formula:

$$\mathcal{L}_{class} = \bar{\psi}(i\not{\partial} - gA \cdot t - m)\psi - \frac{1}{4}\text{Tr} G_{\mu\nu}G^{\mu\nu} \quad (1)$$

where ψ , A are the quark and gluon fields; $\{t\}$ are SU(3) group generators in the fundamental representation; \cdot denotes a sum over the index for the generators; g is the gauge coupling constant; m is the (diagonal) mass matrix of the quarks; and G , the gluon field strength tensor, is given by $G_{\mu\nu} \cdot t = (\partial_\mu A_\nu - \partial_\nu A_\mu) \cdot t - ig[A_\mu \cdot t, A_\nu \cdot t]$. The fundamental constants of this theory are:

- the gauge coupling constant g , or equivalently “alpha-strong” $\alpha_s \equiv g^2/4\pi$;
- the quark masses m_i , $i = 1, \dots, n_f$, where $n_f (= 6)$ is the number of quark flavors; and implicitly,
- the SU(3) group structure constants, $C_F (= \frac{4}{3})$, $C_A (= N_c = 3)$, and $T_R (= \frac{1}{2})$.

In order to quantize this theory, at least within the perturbative formalism, the classical Lagrangian has to be supplemented by a gauge-fixing term, and, in certain classes of gauges (e.g. covariant gauges), also a ghost Lagrangian

$$\mathcal{L}_{eff} = \mathcal{L}_{class} + \mathcal{L}_{gauge-fixing} + \mathcal{L}_{ghost} \cdot \quad (2)$$

The basic formalism of perturbative QCD, embodied in a set of Feynman rules for practical purposes, is well-established and covered in the textbooks and review articles cited in the Introduction.

In principle, the above Lagrangian begets the full richness of QCD physics, both perturbative and non-perturbative. But how do these abstract quantum fields relate to our real world of leptons, hadrons, and electroweak gauge bosons? The connection is provided, of course, by the *quark-parton picture* which phenomenologically describes all high energy processes. The following subsections very briefly highlight the experimental observations which underpin the quark parton model. This leads to asking the question the other way around: how could the quantum field theory of QCD give rise to such a simple picture of high energy interactions as the quark parton model? The answer to this question forms the bulk of the modern theory of PQCD and all its important applications.

2.1 The experimental evidences of quarks and gluons

The idea of quarks, and the glue which holds them together, originated from hadron spectroscopy. Since quarks and gluons have never been seen in the experimental world, the first logical question to ask, independent of any theory, is: how do we really know they exist? The answer turns out to be amazingly simple: although we have not seen single quarks or gluons,¹ their presence is routinely, and unmistakably, revealed in high energy interactions as distinctive “jets.” In addition, their couplings to the electroweak bosons $\{\gamma, W^\pm, Z\}$ have been extensively measured to be those specified in the Standard Model (SM). We very briefly summarize these remarkable results; and use these to motivate the deep theory issues to be explored in PQCD.

2-jet events in e^+e^- collisions and quarks Figure 1a shows a typical hadronic final state event in e^+e^- annihilation at 91 GeV center-of-mass energy (LEP). In comparison to a known 2-particle leptonic final state event $e^+e^- \rightarrow \mu^+\mu^-$, shown in Fig. 1b, it is clear that the 2 jets originate

¹Presumably because they are confined; but this has yet to be convincingly proven.

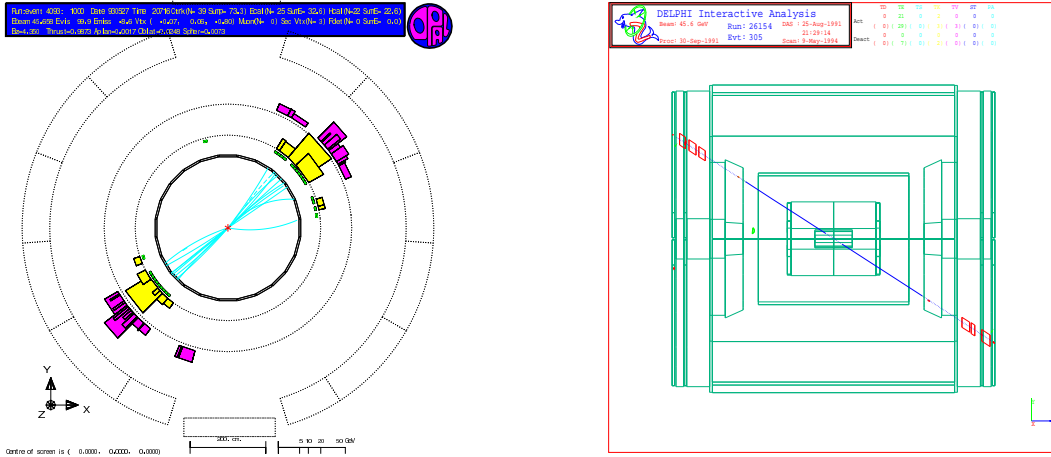


Figure 1: Typical event in $e^+e^- \rightarrow \text{hadrons}$ has 2-jets in the final state (left), compared to $e^+e^- \rightarrow \mu^+\mu^-$ events (right): clear evidence for $q\bar{q}$ creation.

from point-like parents very much like the leptons. The angular distribution of the axis defined by the back-to-back jets with respect to the incoming e^+e^- is measured to be of the familiar shape $\frac{d\sigma}{d\cos\theta} \propto (1 - \cos^2\theta)$ associated with spin- $\frac{1}{2}$ elementary particles. This is shown in Fig. 2.

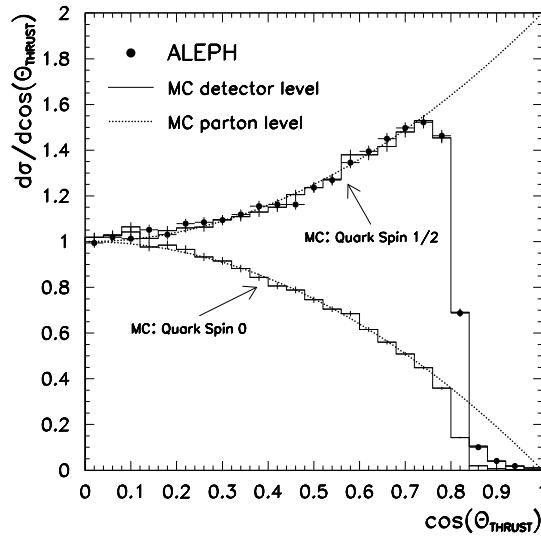


Figure 2: Angular distribution of the 2-jet axis implies spin = $\frac{1}{2}$ for quarks.

The interpretation of these results is inescapable: the e^+e^- annihilate into a quark-anti-quark pair which then “hadronize” into the observed pencil-like jets, as illustrated in Fig. 3.

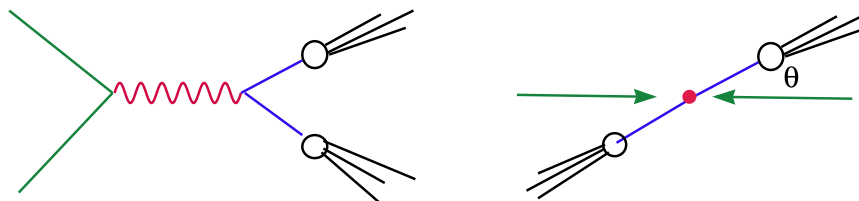


Figure 3: Feynman diagram and CM kinematics for $e^+e^- \rightarrow q\bar{q} \rightarrow 2 \text{ jets}$

3-jet events in e^+e^- collisions and gluons Although the gluon is a bit more elusive than the quarks, particularly since it does not directly couple to electroweak probes, the experimental evidence for the existence of gluon jets is equally convincing. The experimental plot in Fig. 4 shows a typical 3-jet event in e^+e^- annihilation at LEP which comprise about 10% of the hadronic events. The natural interpretation of these events, as due to a $q\bar{q}g$ partonic final state with

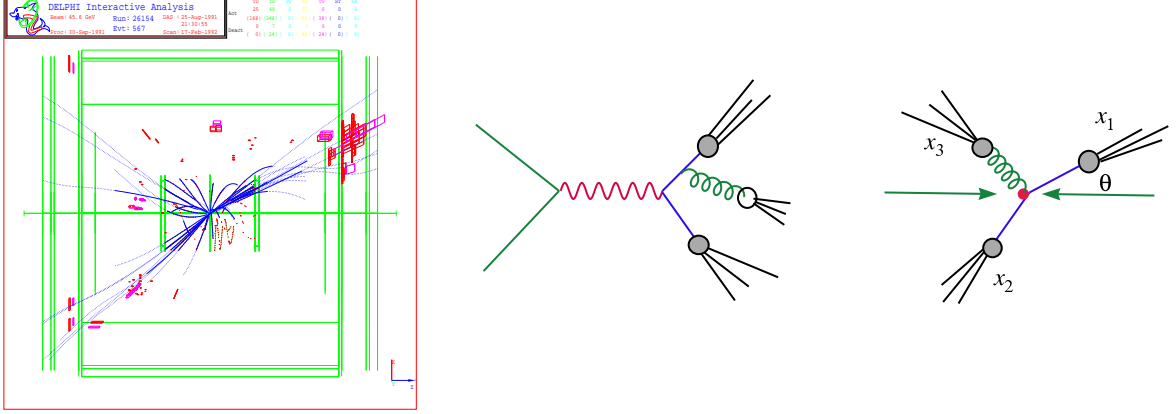


Figure 4: Typical 3-jet event in $e^+e^- \rightarrow \text{hadrons}$: clear evidence for $e^+e^- \rightarrow q\bar{q}g \rightarrow 3$ jets.

subsequent hadronization of the quarks and gluons into hadronic jets, is depicted at the right in the same figure. Detailed experimental study of the angular distributions of the three jets confirms this picture – the spin of the particle underlying the third jet has been shown to be consistent with 1, but inconsistent with 0 or 2 – i.e. the gluon parton is a vector boson. We will come back to discuss the theoretical issues related to the gluon radiation diagrams in the section on infrared safety.

2.2 The electroweak properties of quark partons

The couplings of the quark partons to the electroweak bosons have been extensively studied in lepton-lepton, lepton-hadron and hadron-hadron collisions as depicted in Fig. 5. Using a variety

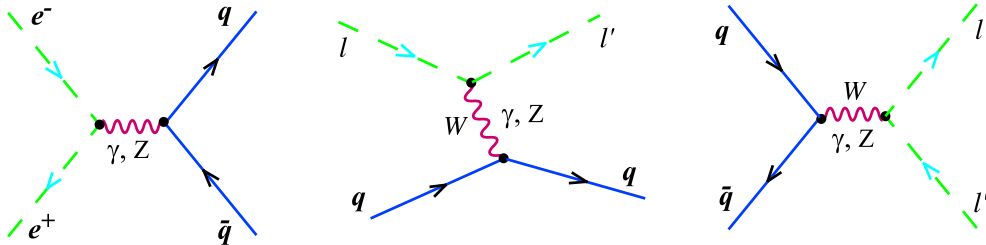


Figure 5: Leading order subprocesses probing the electroweak couplings of quarks to γ, W , and Z : $e^+e^- \rightarrow q\bar{q}$; $\ell q \rightarrow \ell' q$ (DIS); and $q\bar{q}' \rightarrow \ell\ell'$ (DY).

of initial and final states in e^+e^- , $e^\pm N$, $\mu^\pm N$, $\nu(\bar{\nu})N$, pN , $\bar{p}p$ interactions (cf. later sections), the electroweak charges and couplings of the quarks have been shown to follow the pattern of that of the 3 generations of leptons, and are given in Table 1.

Table 1: Quark flavors and their couplings to electroweak vector bosons. g_V and g_A are the vector and axial vector couplings; and V_{ij} is the CKM matrix.

quarks			Q	T_3	γ	Z	W^\pm
u	c	t	$\frac{2}{3}$	$\frac{1}{2}$	Q_i	$T_3^i - 2Q_i \sin^2 \theta_W$	$1 \cdot V_{ij}$
d	s	b	$\frac{1}{3}$	$-\frac{1}{2}$	0	T_3^i	$1 \cdot V_{ij}$

2.3 How can the simple quark parton picture be true in a strongly interacting gauge field theory such as QCD?

How can the simple quark parton picture, so clearly demonstrated by the experiments highlighted above, be true in a strongly interacting gauge field theory such as QCD? The obvious answer given usually is: because the QCD theory is *asymptotically free* – i.e. the quantum theory, after (ultra-violet) renormalization, is characterized by a running coupling $\alpha_s(\mu_r)$ which decreases logarithmically as a function of the renormalization scale μ_r ; thus, the effective coupling becomes small in high energy interactions where it is natural to set $\mu_r \sim Q$, with Q being a typical large physical scale. It is important to add, however, *asymptotic freedom is only a necessary condition* for the validity of the parton picture; it is not sufficient by itself. This is obvious: even with asymptotic freedom, one can only calculate “cross sections” for quarks and gluons; these have no obvious connection to physically measurable processes because quarks and gluons are confined. To make this crucial connection, thus establishing the full modern quark parton model from QCD, it is just as important to have the concept of *infrared safety* and *factorization*. We review the status of asymptotic freedom in this subsection, then explore the other two, more subtle, concepts in their own sections to follow.

Asymptotic Freedom in QCD

The conventional way of expressing asymptotic freedom is through the dependence of the linear coupling $g(\mu) = \sqrt{4\pi\alpha_s(\mu^2)}$,² as expressed in the basic renormalization group equation (RGE):

$$\mu \frac{dg(\mu)}{d\mu} = \beta(g(\mu)) , \quad (3)$$

where the *beta function* is a power series in g beginning at $O(g^3)$,

$$\beta(g) = -g \left(\frac{\alpha_s}{4\pi} \beta_1 + \left(\frac{\alpha_s}{4\pi} \right)^2 \beta_2 + \dots \right) . \quad (4)$$

β_1 can be obtained from a 1-loop calculation of any other physical quantity that depends on μ in perturbation theory. At leading order (LO), it is

$$\beta_1 = 11 - 2n_f/3 = (11N_c - 2n_f)/3 , \quad (5)$$

where n_f is the number of flavors of quarks and N_c the number of colors. The positive contribution, 11, comes mainly from the non-abelian diagrams, such as Fig. 6a in a quark-quark scattering process. The negative contribution, $-2n_f/3$, which weakens asymptotic freedom, comes from the fermion loop diagram in Fig. 6b. In these terms, the solution to the lowest order approximation to Eq. (3)

²We shall drop the subscript r (for *renormalization*) whenever this does not cause any confusion. Later, there will be another $\mu - \mu_f$ for factorization scale – which needs to be distinguished from μ_r .



Figure 6: Feynman diagrams for quark-quark scattering at 1-loop: (a) loops with non-abelian couplings; and (b) “QED-like” loop diagrams.

can be written in terms of a single constant Λ which characterizes its strength at any given scale,

$$\alpha_s(\mu^2) = \frac{4\pi}{\beta_1 \ln(\mu^2/\Lambda^2)} \quad (\text{lowest order}), \quad (6)$$

This scale constant is the famous “ Λ_{QCD} ”. It is of the order of 300 - 500 MeV, depending on the number of quark flavors, n_f .

The next-to-leading order (NLO) solution for $\alpha_s(\mu^2)$ is obtained by using the first two terms in the beta function. There is some freedom of choice in its precise definition at NLO. One conventionally writes $\alpha_s(\mu^2)$ in an expansion in powers of $1/\ln(\mu^2/\Lambda^2)$, where the coefficient of $[1/\ln(\mu^2/\Lambda^2)]^n$ is a polynomial in $\ln(\ln(\mu^2/\Lambda^2))$. Keeping β_1 and β_2 allows us to determine the coefficients of $[1/\ln(\mu^2/\Lambda^2)]^2$,

$$\frac{\alpha_s(\mu^2)}{4\pi} = \frac{1}{\beta_1 \ln(\mu^2/\Lambda^2)} - \frac{\beta_2 \ln(\ln(\mu^2/\Lambda^2))}{\beta_1^3 \ln^2(\mu^2/\Lambda^2)} + O\left(\frac{1}{\ln^3(\mu^2/\Lambda^2)}\right), \quad (7)$$

where $\beta_2 = 102 - 38n_f/3$. Notice that there is no contribution of the form $c/\ln^2(\mu^2/\Lambda^2)$. Such a contribution can be absorbed into a redefinition of Λ . One defines Λ by the condition that $c = 0$. If renormalization is carried out according to the $\overline{\text{MS}}$ scheme, then Λ here is called $\Lambda_{\overline{\text{MS}}}$.

Experimental evidence for asymptotic freedom Since the strong coupling enters into the calculation of all processes beyond the leading order, it can be measured, in principle, in all processes involving hadronic particles. The universality of the function $\alpha_s(\mu)$ provides the most powerful and decisive test of the validity of QCD. Fig. 7a shows a compilation of many measurements of $\alpha_s(\mu)$ made in a variety of physical processes, at energy scales ranging from just above 1 GeV to 200 GeV.³ The logarithmic decrease with the scale μ implied by Eqs. 6 and 7 is dramatically seen. The universality of these measurements of the running coupling at different scales can be tested by converting all the values to the same scale using the RGE 7. The standard scale is usually chosen to be $\mu = M_Z$. The result is shown in Fig. 7b. The agreement is clearly remarkable.

What is still missing?

All the “measurements” of $\alpha_s(\mu)$ shown in Fig. 7, of course, are obtained from comparing PQCD calculations with measured *physical* quantities. As mentioned earlier, the connection between the perturbatively calculable partonic cross sections and the physical variables involving hadrons requires much more than asymptotic freedom. The problem arises already at the parton level. When one calculates partonic processes beyond the leading order (tree graphs), traditional cross sections involving definite number of particles in the final states will be divergent near kinematic boundaries, even after renormalization, in the limit of high energy or vanishing mass of the partons. One can

³We thank S. Bethke and W. Gary for providing this, and other illuminating tables and figures in the following section, as well as helpful discussions concerning QCD studies in e^+e^- interactions.

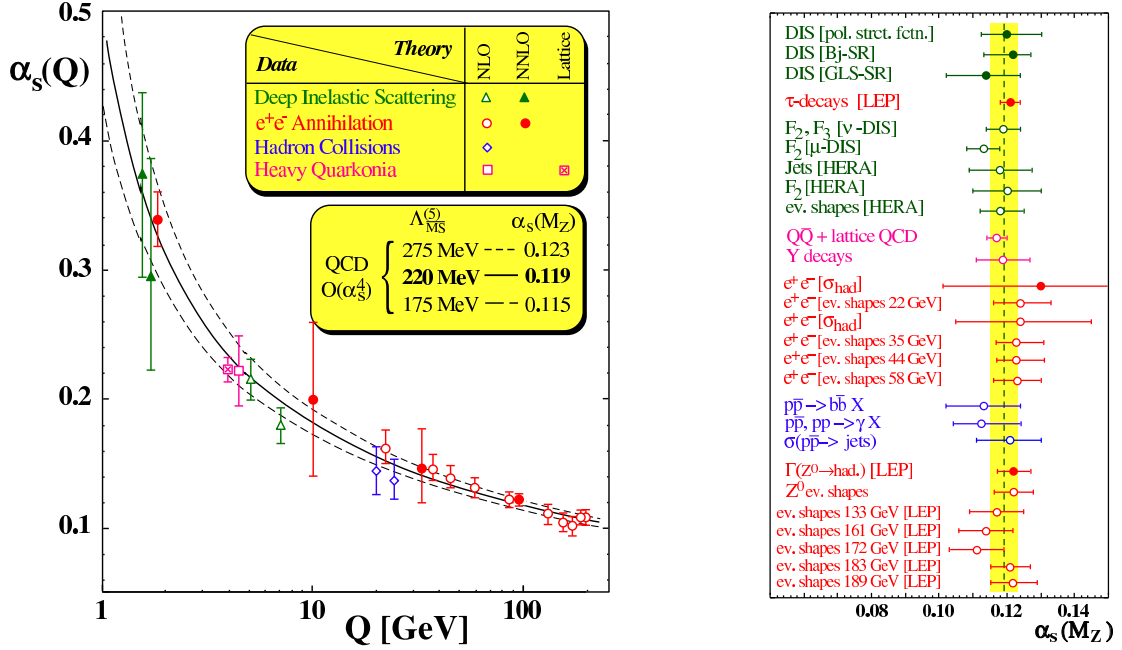


Figure 7: Experimental measurements of the universal QCD running coupling function $\alpha_s(Q)$: (a) as a function of Q ; (b) all measurements converted to an equivalent $\alpha_s(M_Z)$.

obtain finite meaningful answers only for certain classes of cross sections, generally of the *inclusive* type, which are either *infrared safe*, or that can be *factorized* into an infrared safe (short-distance) component and a non-perturbative (long-distance) component which are determined phenomenologically. These are the class of physical observables which can be readily interpreted in the (QCD-improved) quark parton model. We will explore these two important topics, both theoretically and phenomenologically, in the next two sections.

3 Infrared Safety (IRS) and Basic Tests of QCD

This section highlights the general features of infrared singularities, their (long-distance) space-time origin and the cancellation of these singularities in the class of observables which are *infrared safe*.⁴ It concludes with quantitative tests of PQCD based on comparing the predictions of these infrared safe quantities with experimental measurements. These comparisons also allow the determination of the SU(3) group constants for the underlying color symmetry. The physics issues will be illustrated mainly with the calculation of the total hadronic cross section of e^+e^- interaction.

3.1 Collinear and soft singularities

Up to NLO in PQCD, the total hadronic cross section for e^+e^- interaction, $e^+e^- \rightarrow hadrons$, is given by the underlying partonic process $e^+e^- \rightarrow q\bar{q}$ and $e^+e^- \rightarrow q\bar{q}g$. The relevant Feynman diagrams are shown in Fig. 8. The leading order graph, Fig. 8a, is trivial to calculate. The vertex correction to it, Fig. 8b, we will return to later. The essence of the interesting physics issues mentioned in the introductory paragraph can be brought out by examining the $2 \rightarrow 3$ gluon-radiation process represented by Fig. 8c.

⁴Parts of this section are adapted from ref. [6], thanks to permission by D. Soper. For a more theoretical exposition of infrared safety, see ref. [7].

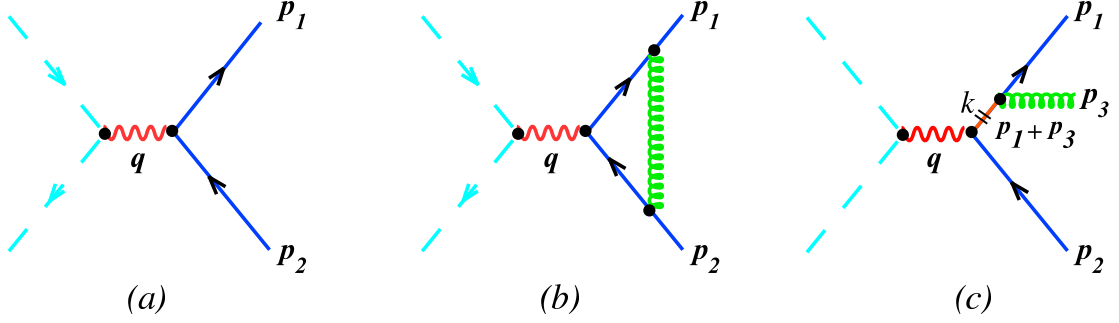


Figure 8: Feynman diagrams for $e^+e^- \rightarrow \text{hadrons}$ to NLO in α_s .

For the three particles in the final state, let $x_i = p_i^0/2\sqrt{s}$ be the fractional energy carried by the i th particle, $i = 1, 2, 3$. See Fig. 9a. As usual, at high energies, it is convenient to neglect the mass of the quark. It is easy to show that, kinematically,

$$\begin{aligned} \Sigma_i x_i &= 2 && \text{(energy conservation)} \\ 2(1 - x_1) &= x_2 x_3 (1 - \cos \theta_{23}) && \text{(and cyclicpermut.).} \end{aligned} \quad (8)$$

The phase space, in terms of the three variables $\{x_i\}$, consists of the inside of a triangle in a ‘‘Dalitz plot’’ shown in Fig. 9b which is important for the following discussion. Note that the sides of the triangle ($x_i = 1$; for some i) correspond to *collinear* configurations, where all momenta are along a line; and the corners of the triangle ($x_i = 0$; for some i) correspond to the *soft* configuration when one particle has vanishing energy and the other two are back-to-back. Both exceptional situations are explicitly depicted in Fig. 9b.

The differential cross section due to the $e^+e^- \rightarrow q\bar{q}g$ process, Fig. 8c, is given by

$$\frac{d\sigma}{\sigma_0 dx_1 dx_2} = \frac{\alpha_s}{2\pi} C_F \frac{x_1^2 + x_2^2}{(1 - x_1)(1 - x_2)}, \quad (9)$$

here σ_0 is the LO total cross section and C_F is one of the group constants.

It is easy to see that the differential cross section diverges near the boundaries of the phase space, when either $x_i = 0$ or $x_i = 1$, since either condition will cause the denominator in Eq. (9) to vanish, according to Eq. (8) and Fig. 9b. If we try to integrate Eq. (9) over the 3-particle phase space to calculate the ‘‘total cross section’’ for $e^+e^- \rightarrow q\bar{q}g$, we would get a logarithmically divergent answer – this quantity is *infrared singular*. In other words, the total cross section for

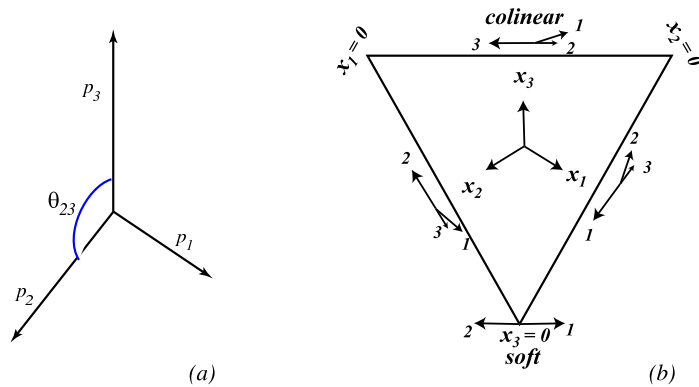


Figure 9: Kinematics of the 3-particle final state in $e^+e^- \rightarrow q\bar{q}g$ (a) momentum configuration; (b) the ‘‘Dalitz’’ plot.

this $2 \rightarrow 3$ process is *not infrared safe*. What is the origin of this singular behavior? We have already seen from Fig. 9b, these singularities are associated with collinear and soft configurations in momentum space. It can be easily deduced from Eq. (8) and Fig. 9b that in both degenerate kinematic situations, the “virtual particle” line, having 4-momentum $k = p_1 + p_3$ in the case of Fig. 8c, goes on mass-shell $-k^2 = 0$ (or $k^2 \simeq m^2$ if we had kept a small quark mass).

The singular region lies at the boundaries of the phase space, where the $2 \rightarrow 3$ kinematics reduce to that of an equivalent $2 \rightarrow 2$ process. This observation suggests that the proper interpretation and treatment of these apparent divergent results must involve simultaneous consideration of $e^+e^- \rightarrow q\bar{q}g$ with the $2 \rightarrow 2$ partonic process $e^+e^- \rightarrow q\bar{q}$ at the same order of α_s , as we will discuss in the subsection following the next.

First, it is instructive to find out the space-time picture associated with these singular configurations.

3.2 Singularities are due to long-distance space-time interactions

In the space-time picture, the collinear and soft singularities are associated with long-distance interactions. This can be seen as follows. We will examine the relation between the momentum space and space-time descriptions using the very convenient light-cone components of 4-vectors:

$$v^\pm = (v^0 \pm v^3)/\sqrt{2} \quad (10)$$

which implies

$$\begin{aligned} k^2 &= 2k^+k^- - k_T^2 \quad (\simeq m^2 \simeq 0, \text{ if on mass shell}) \\ x \cdot k &= x^-k^+ + x^+k^- - \vec{x}_T \cdot \vec{k}_T \end{aligned} \quad (11)$$

For the situation appropriate for examining collinear and soft singularities, let us choose the z -axis to be close to the direction of the collinear partons, \vec{k} , and opposite to the direction of \vec{p}_2 . Since the Green functions in the two spaces are related by the 4-dim Fourier transform $\int d^4k e^{ik \cdot x} S_F(k) \dots$, the momentum space conditions,

$$k^+ \simeq \sqrt{\frac{s}{2}} \quad (\text{very large } e) \quad ; \quad k^- = \frac{k_T^2 + m^2}{2k^+} \sim \frac{k_T^2 + m^2}{\sqrt{s}} \quad (\text{very small}), \quad (12)$$

translate to the conjugate space-time configuration

$$x^+ \sim \frac{\sqrt{s}}{k_T^2 + m^2} \quad (\text{very large } e) \quad ; \quad x^- \sim \frac{1}{\sqrt{s}} \quad (\text{very small}). \quad (13)$$

The k - space and x -space configurations are illustrated in Figs. 10a,b.

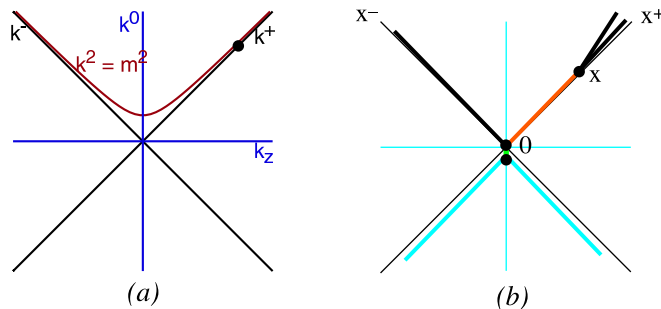


Figure 10: Important regions contributing to the infra-red singularities: (a) in momentum space; and (b) in space-time.

Figure 10b shows that the interaction region which gives rise to infrared singularities is at a long distance away from the creation of the quark-anti-quark pair (at the origin of the coordinate system in the picture). This fact is important for subsequent discussions. We note that these singular regions represent one of the simplest examples of solutions to the Landau equations for pinch surfaces of general Feynman diagram, supplemented by the Coleman-Norton theorem.²

3.3 Infrared safety and cancellation of IR singularities

What can, or should, be done with the IR singular contributions to the cross section calculation? Since physical cross sections are finite by definition, these singularities in the perturbative calculation of partonic cross section must be artificial. They should disappear when we ask the right physics questions, and make the proper connection between these and the partonic calculations. The fact that the relevant phase space region corresponds to configurations when the “virtual” quark line with momentum k almost goes on mass-shell (hence becomes “real”), that the kinematics of the $2 \rightarrow 3$ process is degenerate with that of an equivalent $2 \rightarrow 2$ one, and that the interaction happens at long distances away from the $e^+e^- \rightarrow q\bar{q}$ interaction vertex in space-time, all point to the fact that the relevant physics observables must be insensitive to long-distance interactions and to the indistinguishable $2 \rightarrow 2$ and $2 \rightarrow 3$ origin of the interaction. For example, if we are only interested in the total cross section, then what happens at long distances is unimportant. After the initial $q\bar{q}$ pair is created, the probability for them to turn into hadrons, even if happening at long-distances, is unity – whether one of the quarks split into two partons before hadronization is immaterial.

This intuitive argument rests on the principle of unitarity. Its validity is not confined to the total cross section, since there are a large variety of physical observables which combine the $2 \rightarrow 2$ and $2 \rightarrow 3$ partonic contributions in the proper way to yield finite answers in the degenerate configuration, but which are otherwise completely distinct away from the boundary of phase space. The common characteristic among all these infrared safe quantities is that they must be “inclusive”, so as to allow the proper combination of contributions from different orders of perturbative calculations in general. The basic idea behind infrared safety goes back to the Block-Nordsieck theorem in QED. The subject has become much richer and more sophisticated in the context of QCD, where it forms a key element in establishing the connection between physics predictions and calculations based on partons.²

The observations made above are only indicative of the direction toward, but does not constitute a proof of, infrared safety. In the simple case of the total cross section of $e^+e^- \rightarrow \text{hadrons}$ under discussion, it is well-known that the IR singularities in the cross section formula (9) for $e^+e^- \rightarrow q\bar{q}g$ are cancelled in a full NLO calculation by equal and opposite-sign singular contributions from the cross-term between the LO and the vertex correction graphs of Fig. 8a,b. The full result is infrared safe. To order α_s^2 , it is given by

$$\sigma_h^{\text{NNLO}}(s) = \sigma_h^{\text{LO}}(s) \left[1 + \frac{\alpha_s(\mu)}{\pi} + \left(\frac{\alpha_s(\mu)}{\pi} \right)^2 C_2\left(\frac{\mu^2}{s}\right) + \dots \right] \quad (14)$$

where

$$\begin{aligned} \sigma_h^{\text{LO}}(s) &= \frac{12\pi\alpha^2}{s} (\sum_f Q_f^2) \\ C_2\left(\frac{\mu^2}{s}\right) &= 1.4092 + 1.9167 \ln\left(\frac{\mu^2}{s}\right) \end{aligned} \quad (15)$$

This calculation has currently been carried out to order α_s^3 .⁹

Both the space-time interpretation of the singularities and their cancellation in the calculation of IRS physical quantities, such as the total cross section discussed here, represent general features of PQCD shared by a wide range of useful applications.

3.4 IRS quantities in e^+e^- collisions

The above example suggests that, in order to ensure the cancellation of apparent infrared singularities in partonic cross sections, we need to form inclusive quantities which do not distinguish between a partonic process with $n + 1$ particles in the final state under degenerate kinematic conditions, when some of the particles are collinear or soft, from similar ones with the same kinematics but fewer number of particles. Formally, one can show that¹⁰ an inclusive quantity

$$\begin{aligned} \mathcal{I} &= \frac{1}{2!} \int d\Omega_2 \frac{d\sigma[2]}{d\Omega_2} \mathcal{S}_2(p_1^\mu, p_2^\mu) \\ &+ \frac{1}{3!} \int d\Omega_2 dE_3 d\Omega_3 \frac{d\sigma[3]}{d\Omega_2 dE_3 d\Omega_3} \mathcal{S}_3(p_1^\mu, p_2^\mu, p_3^\mu) \\ &+ \dots \end{aligned} \quad (16)$$

is *infrared safe* provided the functions $\{\mathcal{S}\}$ which define this observable are symmetric functions of their arguments and

$$\mathcal{S}_{n+1}(p_1^\mu, \dots, (1-\lambda)p_n^\mu, \lambda p_n^\mu) = \mathcal{S}_n(p_1^\mu, \dots, p_n^\mu) \quad (17)$$

for $0 \leq \lambda \leq 1$. The simplest possible example of such an IRS quantity is obtained by choosing $\mathcal{S}_n = 1$ for all n – this gives the total hadronic cross section, i.e. $\mathcal{I} = \sigma_{tot}$.

An important feature of IRS quantities is that, not only are the partonic calculations finite, but also one expects the results to be applicable to the corresponding physical observables with the partons replaced by hadronic “jets.” This is intuitively reasonable, since soft particles are not resolvable in the detectors and collinear particles in jets can be combined to form the primitive partons. The hadronization of a parton into an observable jet is a long-distance space-time process. The cancellation of infrared singularities in IRS quantities means that the latter are insensitive to the details of how the hadronization takes place – as long as the details are not experimentally observed, unitarity ensures that hadronization occurs with the probability 1.

To study jet cross sections quantitatively, specific “jet algorithms” which satisfy Eq. (16) must be adopted, and they must be consistent between the theoretical calculation and the definition adopted in the experimental measurement. The original Serman-Weinberg definition of jet cross section¹¹ has since been supplanted by various cone and algebraic algorithms¹² in current applications.

Another class of IRS observables are “event shape” variables, of which the widely used *thrust*, is a good example

$$\mathcal{T}_n(p_1^\mu, \dots, p_n^\mu) = \max_{\vec{u}} \frac{\sum_{i=1}^n |\vec{p}_i \cdot \vec{u}|}{\sum_{i=1}^n |\vec{p}_i|} . \quad (18)$$

Here \vec{u} is a unit vector, which one varies to maximize the sum of the absolute values of the projections of \vec{p}_i on \vec{u} . Then the thrust distribution $(1/\sigma_{tot}) d\sigma/dT$ is defined by taking

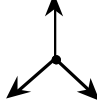
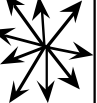
$$\mathcal{S}_n(p_1^\mu, \dots, p_n^\mu) = (1/\sigma_{tot}) \delta(T - \mathcal{T}_n(p_1^\mu, \dots, p_n^\mu)) . \quad (19)$$

It is a simple exercise to show that the thrust of an event is not affected by collinear parton splitting or by zero momentum partons. Therefore the thrust distribution is infrared safe. For more examples of IRS shape parameters, see Ref. [13].

3.5 More quantitative tests of QCD in e^+e^- collisions

The large number of proposed IRS quantities in e^+e^- collisions provide a fertile ground for comparison between theory and experiment. Such comparisons, on the one hand, test the validity of PQCD calculations; and on the other hand, provide many complementary ways to measure the fundamental QCD constants which enter the theoretical expressions. Among these are the group constants C_A, C_F , and T_R of the color SU(3) gauge group, in addition to the universal coupling α_s already described in Sec. 2.3.

The following table illustrates the wide scope of the endeavor to study IRS shape parameters in e^+e^- collision. These serve to test PQCD calculations and to measure the basic QCD parameters.¹³

Name of Observable	Definition	Typical Value for:			QCD calculation
					
Thrust	$T = \max_{\vec{n}} \left(\frac{\sum_i \vec{p}_i \vec{n} }{\sum_i \vec{p}_i } \right)$	1	$\geq 2/3$	$\geq 1/2$	(resummed) $O(\alpha_s^2)$
Thrust major	Like T, however T_{maj} and \vec{n}_{maj} in plane $\perp \vec{n}_T$	0	$\leq 1/3$	$\leq 1/\sqrt{2}$	$O(\alpha_s^2)$
Thrust minor	Like T, however T_{min} and \vec{n}_{min} in direction \perp to \vec{n}_T and \vec{n}_{maj}	0	0	$\leq 1/2$	$O(\alpha_s^2)$
Oblateness	$O = T_{\text{maj}} - T_{\text{min}}$	0	$\leq 1/3$	0	$O(\alpha_s^2)$
Sphericity	$S = 1.5 (Q_1 + Q_2)$; $Q_1 \leq \dots \leq Q_3$ are Eigenvalues of $S^{\alpha\beta} = \frac{\sum_i p_i^\alpha p_i^\beta}{\sum_i p_i^2}$	0	$\leq 3/4$	≤ 1	none (not infrared safe)
Aplanarity	$A = 1.5 Q_1$	0	0	$\leq 1/2$	none (not infrared safe)
Jet (Hemisphere) masses	$M_{\pm}^2 = (\sum_i E_i^2 - \sum_i \vec{p}_i^2)_{i \in S_{\pm}}$ (S_{\pm} : Hemispheres \perp to \vec{n}_T) $M_H^2 = \max(M_+^2, M_-^2)$ $M_D^2 = M_+^2 - M_-^2 $	0	$\leq 1/3$	$\leq 1/2$	(resummed) $O(\alpha_s^2)$
Jet broadening	$B_{\pm} = \frac{\sum_{i \in S_{\pm}} \vec{p}_i \times \vec{n}_T }{2 \sum_i \vec{p}_i }$; $B_T = B_+ + B_-$ $B_w = \max(B_+, B_-)$	0	$\leq 1/(2\sqrt{3})$	$\leq 1/(2\sqrt{2})$	(resummed) $O(\alpha_s^2)$
Energy-Energy Correlations	$EEC(\chi) = \sum_{\text{events}} \sum_{i,j} \frac{E_i E_j}{E_{\text{vis}}^2} \int_{\chi + \frac{\Delta\chi}{2}}^{\chi - \frac{\Delta\chi}{2}} \delta(\chi - \chi_{ij})$				(resummed) $O(\alpha_s^2)$
Asymmetry of EEC	$AEEC(\chi) = EEC(\pi - \chi) - EEC(\chi)$				$O(\alpha_s^2)$
Differential 2-jet rate	$D_2(y) = \frac{R_2(y - \Delta y) - R_2(y)}{\Delta y}$				(resummed) $O(\alpha_s^2)$

We shall only present the result of one of these studies, the thrust distribution, as an illustration. This will be followed by a brief summary of the measurement of the color factors resulting from many of these shape parameter studies.

The thrust distribution: Figure 11 shows the thrust distribution, defined in Eq. (19), as measured by the SLD experiment in e^+e^- collisions.¹⁴ The data is compared to NLO QCD calculations (order α_s^2 , solid line) and “resummed calculation” (dashed line). The horizontal axis is $\tau = 1 - T$. One sees that the NLO QCD calculation agrees well with experiment in the middle range of the thrust variable, confirming the validity of the perturbative approach. But noticeable deviation appears toward the $\tau \rightarrow 0$ ($T \rightarrow 1$) limit. The reason is: near this edge of the phase space, large logarithms of the form $\log(1/\tau)$ in the perturbative calculation spoil the convergence of the perturbation series. These large contributions must be brought under control by an re-organization of the perturbation expansion. This is referred to as “resummation.”⁷ In Fig. 11, the resummed calculation (dashed line) is seen to agree rather well with the measurement.

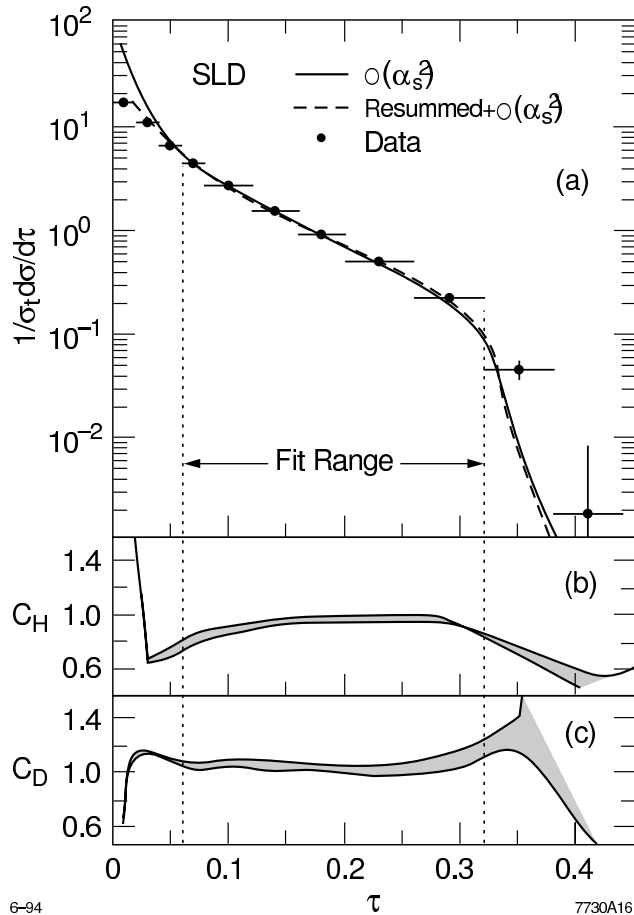


Figure 11: (a) The thrust distribution as measured by the SLD experiment, compared to NLO QCD calculation with a fixed choice of μ , and to the resummed QCD calculation. (b) and (c) show the hadronization and detector correction factors.

Measurement of the color $SU(3)$ group constants: Since the theoretical expressions for all IRS quantities depend on the the group constants of the underlying color symmetry group $SU(3)$, comparison of these expressions with experimental results of these quantities can be used to measure these constants, just like the measurement of the universal QCD coupling α_s discussed earlier. Figure 12 summarizes results of the measurements of C_A and C_F , obtained from several experiments on the various shape parameters.³ We can see that the results are in perfect agreement with the expected values for $SU(3)$.

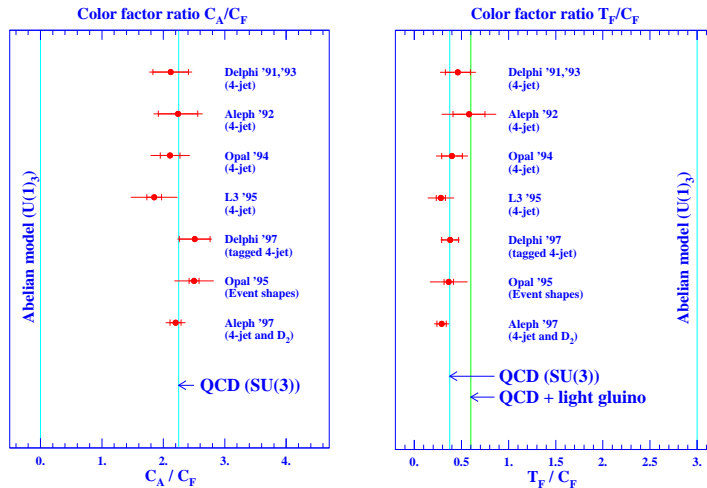


Figure 12: Measurements of the ratio of QCD group constants in e^+e^- collisions. This figure is compiled by W. Gary.³

4 Factorization and the QCD Parton Model

If predictions of PQCD were confined to IRS observables only, its scope would be rather limited. By invoking unitarity to sum over all long-distance effects, there would be no possibility of probing the partonic structure of hadrons; nor would it be possible to make *predictions* of high energy cross section processes based on existing knowledge of hadron structure. The fact that the scope of PQCD can be greatly expanded to provide the foundation for the powerful parton model is made possible by the remarkable property of *factorization*.^{6,7} From the perturbative point of view, factorization applies to a large class of inclusive partonic cross sections which, although not infrared safe by themselves, are nonetheless factorizable into a short-distance (hard) part which is IRS, and a long-distance (soft) part which is IR singular but has the virtue of being *universal*. This separation of short- and long-distance factors allows us to generalize from (calculable) partonic cross sections to (physically measurable) hadronic cross sections.

As an extension to the discussions of IRS of Sec. 3.3, we first introduce the key ideas of factorization for the one-particle inclusive cross section in e^+e^- annihilation. In addition to focusing on the physical ideas behind this important new feature, we emphasize close analogies between factorization of IR singularities and textbook ultra-violet (UV) renormalization theory. These analogies, as well as the key role of *scale transformation* in both cases, are summarized and highlighted in Sec. 4.2. We then turn to the phenomenologically important deep inelastic scattering (DIS) process in Sec. 4.3. There, we will examine factorization from a different perspective and work out a concrete example to show in detail how factorization of collinear singularity works, both analytically and physically. Sec. 4.4 describes the proper definition and use of the universal parton distributions. Sec. 4.5 discusses the scale dependence of PQCD predictions. This section concludes with a summary of the remarkable multi-facet roles played by the factorization theorem in the whole of the QCD parton model framework in Sec. 4.6. Our discussion will be based on lowest non-trivial order examples and heuristic arguments. For formal proofs of factorization, cf. Refs. [15,18,19].

4.1 Essential ideas of Factorization in e^+e^- annihilation

Consider the inclusive process $e^+e^- \rightarrow A(p) + X$, where $A(p)$ represents a parton (i.e. quark or gluon) or a hadron with momentum p and X stands for “anything.” For simplicity, we consider the exchange of a virtual photon only. The differential cross section for this process is given, in general, by

$$d\sigma = \frac{4\alpha^2}{sQ^2} \frac{d^3\mathbf{p}}{2|\mathbf{p}|} L^{\mu\nu} \cdot W_{\mu\nu}(q, p), \quad (20)$$

where $L^{\mu\nu}$ is the calculable lepton tensor, $J_\mu(x)$ is the electromagnetic current 4-vector, and $W_{\mu\nu}(q, p)$ is the parton or hadron tensor defined by

$$W_{\mu\nu}(q, p) = \frac{1}{4\pi} \int d^4x e^{iqx} \sum_X \langle 0 | J_\mu(0) | A(p), X \rangle \langle A(p), X | J_\nu^\dagger(x) | 0 \rangle. \quad (21)$$

It is the square of the hadronic amplitude $\gamma^* \rightarrow A(p) + X$, summed over the final states, with the exception of the detected particle $A(p)$. The pictorial representation of the amplitude and the $W_{\mu\nu}$ tensor are shown in Fig. 13.

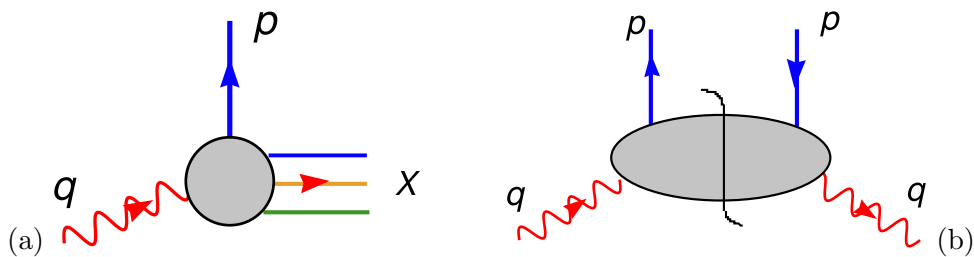


Figure 13: For the e^+e^- one particle inclusive process: (a) the hadronic amplitude; and (b) the hadronic tensor $W_{\mu\nu}$ or the corresponding structure functions $F^\lambda(z, Q)$.

It is convenient to introduce the helicity structure functions,

$$F_A^\lambda(x, Q) = \epsilon_\mu^{\lambda*}(q, p) \cdot W^{\mu\nu}(q, p) \cdot \epsilon_\nu^\lambda(q, p), \quad (22)$$

where $Q = \sqrt{s}$, x is the fractional energy carried by A ($x = 2p^0/Q$), ϵ_μ^λ is the polarization vector of the virtual photon with $\lambda = T, L$ for transverse and longitudinal polarizations respectively. Then the final cross section formula can be derived as

$$\frac{d\sigma}{dz d\cos\theta} = \frac{\pi\alpha^2}{2s} [F_A^T(x, Q)(1 + \cos^2\theta) + F_A^L(x, Q)\sin^2\theta] \quad (23)$$

where θ is the CM scattering angle of A . One can also define invariant structure functions $F_{\{1,2\}}$ by expanding $W_{\mu\nu}$ in terms of a set of independent tensors; and relate $F_{\{1,2\}}$ to $F^{\{T,L\}}$. We shall not do this here, since our primary interest is to discuss the physics of factorization, which applies to any of these structure functions. We will treat the kinematics in more detail for the analogous case of deep inelastic scattering later in Sec. 5.1 when we discuss the phenomenology of PQCD.

Factorization of partonic cross sections

In perturbation theory, we can only calculate the partonic structure function, with $A = \alpha$, a parton label. We shall suppress the helicity index λ , since all considerations apply to any λ . $F_\alpha(x, Q)$ is

calculated from summing all Feynman diagram contributions to the partonic processes $e^+e^- \rightarrow q\bar{q}$, $e^+e^- \rightarrow q\bar{q}g, \dots$ etc. – the same ones considered in the previous section on IRS, cf. Fig. 8; it depends on the kinematic variables (x, Q) , as well as on the basic QCD parameters (α_s, m_i) . We know from the previous section that at order α_s and beyond, the PQCD contributions contain IR singularities when some of the partons assume degenerate kinematic configurations. These singularities will remain, now that we consider a final state parton with a specific momentum p , rather than summing over all final states with some IRS prescription.

Factorization concerns isolating these singularities as universal factors (associated with long-distance interactions as described before) and absorbing them into non-perturbative (but eventually measurable) parton distribution and fragmentation functions – much in the same way UV divergences in these perturbative calculations (associated with short-distance interactions) are isolated into universal renormalization constants and absorbed into measurable physical constants in conventional renormalization theory.

Specifically, it can be established that,¹⁵ order-by-order in perturbation theory to arbitrary orders, all IR singular contributions to F_α are factorizable in the following way, cf. Fig. 14:

$$F_\alpha(Q, x, m) = \sum_a \int \frac{dz}{z} \hat{F}_a\left(\frac{x}{z}, \frac{Q}{\mu_f}, \alpha_s\right) \cdot D_\alpha^a\left(z, \frac{m}{\mu_f}, \alpha_s\right) + \mathcal{O}\left(\frac{m^2}{Q^2}\right) \quad (24)$$

where m represents a generic confinement scale (quark masses or Λ_{QCD}), \hat{F}_a is the perturbatively calculable (IRS) “hard” *partonic structure function* for producing a parton labeled “ a ”, $D_\alpha^a(z, m/\mu_f, \alpha_s)$ is the *fragmentation function* of parton “ a ” into parton α with momentum fraction z , and μ_f is the *factorization scale*.

The key features of this fundamental *Factorization Theorem* are:

- The factorized term on the right-hand-side consists of a convolution integral in the momentum fraction variable. It is accurate to “leading twist” (power) approximation: it includes all logarithmic effects ($\log(Q/\mu_f)$, $\log(\mu_f/m)$); but is subject to power-law corrections as indicated.
- The factorization refers to the separation of the functional dependence of the partonic (“bare”) structure function $F_\alpha(x, Q, m)$ into a long-distance physics factor D_α^a associated with the confinement scale m , and a short-distance physics factor \hat{F}_a associated with the large momentum scale Q . This is achieved with the introduction of a *factorization scale* μ_f which, qualitatively speaking, characterizes the boundary between the two distinct physical scales.
- The left-hand-side of the equation (F_α) is manifestly independent of μ_f . The individual factors in the factorized formula on the right-hand-side do depend on μ_f . Their convolution, however, should be independent of μ_f – but only to the order up to which the perturbative calculation has been carried out. In practice, in order to invoke asymptotic freedom and to keep the perturbative

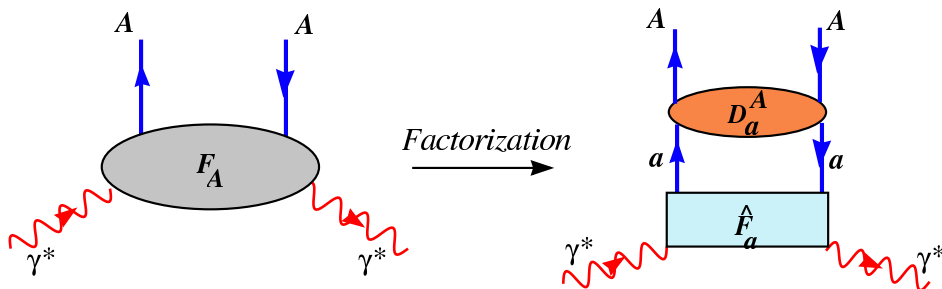


Figure 14: e^+e^- 1-particle inclusive: factorization theorem \Rightarrow QCD parton model.

expansion under control, μ_f should be of the order of the typical hard scale Q – just like in the case of the renormalization scale μ_r (which appears in $\alpha_s(\mu_r)$ and the renormalized quark masses $m_i(\mu_r)$). For this reason, it is common practice to set $\mu_f = \mu_r \equiv \mu$ for the sake of simplicity. We shall adopt this simplification except in situations where the distinction between the two becomes important.

- As mentioned above, the IR singularities which are factored into the partonic fragmentation functions $D_\alpha^a(z, m/\mu, \alpha_s)$ are universal. (Thus, they have implicit dependence on some regulator parameter, such as ε in dimensional regularization.) To define $D_\alpha^a(z, m/\mu, \alpha_s)$ precisely, one must also specify the finite terms which go along with the universal singular pieces. Each specific prescription for choosing the finite subtraction defines a distinct *factorization scheme* for $D_\alpha^a(z, m/\mu_f, \alpha_s)$, hence \hat{F}_a by implication. $\{D_\alpha^a\}$ are the analogue of renormalization constants in UV renormalization. The bare F_α , by definition, is scheme independent. (This fact will be made explicit in the example we present for the factorization of DIS structure functions, Sec. 4.3.)
- The μ -dependence of these functions is governed by a renormalization group equation (RGE)

$$\mu \frac{\partial}{\partial \mu} D_\alpha^a(z, m/\mu, \alpha_s(\mu)) = \sum_b \int \frac{dy}{y} P_b^a\left(\frac{z}{y}, \alpha_s\right) \cdot D_\alpha^b(y, m/\mu, \alpha_s) \quad (25)$$

where $P_b^a(x, \alpha_s)$ are elements of the (matrix) *splitting function*, or *evolution kernel*. They are, order-by-order, finite in PQCD. The (Mellin) moments of the evolution kernel are the analogue of the anomalous dimension coefficients in the UV RGE. Eq. (25) is the *QCD evolution equation* for the fragmentation functions $D_\alpha^a(z, m/\mu, \alpha_s)$ which plays a key role in the QCD parton model.

- Since all IR singularities of F_α have been separated and factored (subtracted) into the long-distance D_α^a factor, the “hard” structure functions $\hat{F}_a(x, Q/\mu, \alpha_s)$ are IRS, hence calculable (i.e. finite) order-by-order in PQCD.

These features permit the generalization of the factorization of bare partonic structure functions (and cross sections) to physical ones.

Hadronic cross sections and the QCD Parton Model

Now, consider the *physical* one-particle inclusive process $e^+e^- \rightarrow A(p)+X$ where A is a hadron (say, pion). The *factorization theorem* in this case is inferred from Eq. (24) by replacing the perturbative (IR singular) partonic fragmentation functions $D_\alpha^a(z, m/\mu_f, \alpha_s)$ by the non-perturbative (finite) *hadronic fragmentation functions* $D_A^a(z, \mu_f)$:⁵

$$F_A(z, Q) = \sum_a \hat{F}_a\left(z, \frac{Q}{\mu_f}, \alpha_s(\mu_r)\right) \otimes D_A^a(z, \mu_f) + \mathcal{O}\left(\frac{m^2}{Q^2}\right) \quad (26)$$

where F_A is the physical structure function (or cross section) for producing the hadron A , $z = 2p^0/Q$ is the fractional energy carried by the detected hadron, \hat{F}_a is the *same* IRS hard partonic structure function for producing a parton labeled “ a ” which enters the partonic factorization formula (Eq. (24), and $D_A^a(y, \mu_f)$ is the *fragmentation function* of parton “ a ” into hadron A with momentum fraction y . Here, a simplifying notation, \otimes , for the convolution integral has been introduced,

$$f(z) \otimes g(z) \equiv \int_x^1 \frac{dy}{y} f\left(\frac{z}{y}\right) g(y). \quad (27)$$

⁵We suppress the variable m (the hadron and quark mass scales of the problem) in D_A^a since, for these non-perturbative fragmentation functions, the dependence on parameters at the confinement scale is totally unknown.

The important features of this master equation (cf. also Sec. 4.6) are:

- The *factorization theorem* in the form of Eq. (26) provides the theoretical basis for the *QCD parton model*, as illustrated graphically in Fig. 14. Dropping the remainder term on the RHS of Eq. (26), it is accurate to the leading twist approximation, as in Eq. (24).
- The transition from the perturbative Eq. (24) to the physical Eq. (26), whereby the perturbatively calculable (but singular) partonic D_α^a are replaced by physical (but uncalculable) hadronic D_A^a , is analogous to that from bare Green functions to renormalized Green functions in UV renormalization theory where the (UV singular) renormalization constants are absorbed into bare constants to form the (finite but uncalculable) physical coupling and masses. In this case, D_A^a are not calculable in PQCD because they involve long-distance physics; but they can be determined from experimental measurements, as we will discuss in the remainder of this review.
- The remarks concerning the μ -dependence of the various factors made about the perturbative factorization of partonic cross sections, Eq. (24), in the previous subsection also apply to the hadronic case, Eq. (26).
- In particular, the fragmentation functions (henceforth abbreviated as FFs) satisfy the same RGE, Eq. (25), with the same IRS evolution kernels P_b^a , and the partonic D_α^a replaced by the hadronic D_A^a . Thus, if the FFs $D_A^a(x, \mu)$ are specified at a given scale $\mu = Q_0$, $D_A^a(x, Q_0)$, they are predicted by PQCD at all scales $\mu = Q$.

We shall see that, the same factorization theorem applies for hadrons in the *initial state*, with parton distribution functions (PDFs), $f_{b/A}^a(x, \mu)$, appearing in place of the FFs $D_{b/A}^a(x, \mu)$. The PDFs and the FFs together represent our knowledge of the partonic structure of hadrons. PDFs, in fact, play a more prominent role in particle physics phenomenology. We shall discuss the PDFs in the context of DIS in Sec. 4.3, after summarizing the similarities and differences of factorization and renormalization in the next subsection.

The **power of the factorization-theorem-based parton model** rests with its ability to enable a wide range of *predictions*:

- Using as inputs a set of experimental measurements in some limited energy range to the LHS of Eq. (26) $\{F_A\}$, the perturbatively calculated hard cross sections $\{\hat{F}_a\}$ on the RHS, together with the evolution equation as constraint, one can phenomenologically determine the universal functions $\{f_A^a(x, \mu)\}$ and $\{D_A^a(x, \mu)\}$;
- Once the PDFs and FFs are known in a limited energy range, they can be extended to arbitrary high energies by the same evolution equations;
- These universal PDFs and FFs can then be used with any theoretically calculated hard cross sections $\{\hat{F}_a\}$ as inputs to the RHS of Eq. (26) to *make predictions* of cross sections for *both Standard Model and new physics* processes at *arbitrary energies*.

This strategy has been used extensively in e^+e^- collider experiments to determine the FFs;¹⁶ and in lepton-hadron and hadron-hadron interactions to determine PDFs, cf. Sec. 6. The resulting PDFs and FFs are essential input to all calculations of high energy processes.

4.2 Renormalization, factorization, and scale transformations

In introducing the essential features of IR factorization which form the foundation of the QCD parton model, we have emphasized the analogies to the well-known UV renormalization theory. The concept of scale transformation, controlled by renormalization group equations, is fundamental in both cases. We are interested in physical phenomena at some energy range, say 1 GeV to 10 TeV. In UV renormalization, the renormalized coupling $\alpha_s(\mu)$ and masses $m_i(\mu)$ absorb the apparent singularities at ultra-high energies which plague the perturbation series (due to inaccessible short-distance interactions). Likewise, in IR factorization discussed in the previous subsection, the hadronic PDFs and FFs absorb the apparent collinear and soft singularities which arise in perturbative calculations (due to long-distance interactions at the confinement energy scale, beyond the reach of PQCD). Thus renormalization and factorization play similar roles – at the opposite ends of the applicable energy range of the PQCD theory. The underlying ideas of these scale transformations are summarized in the following illustration.

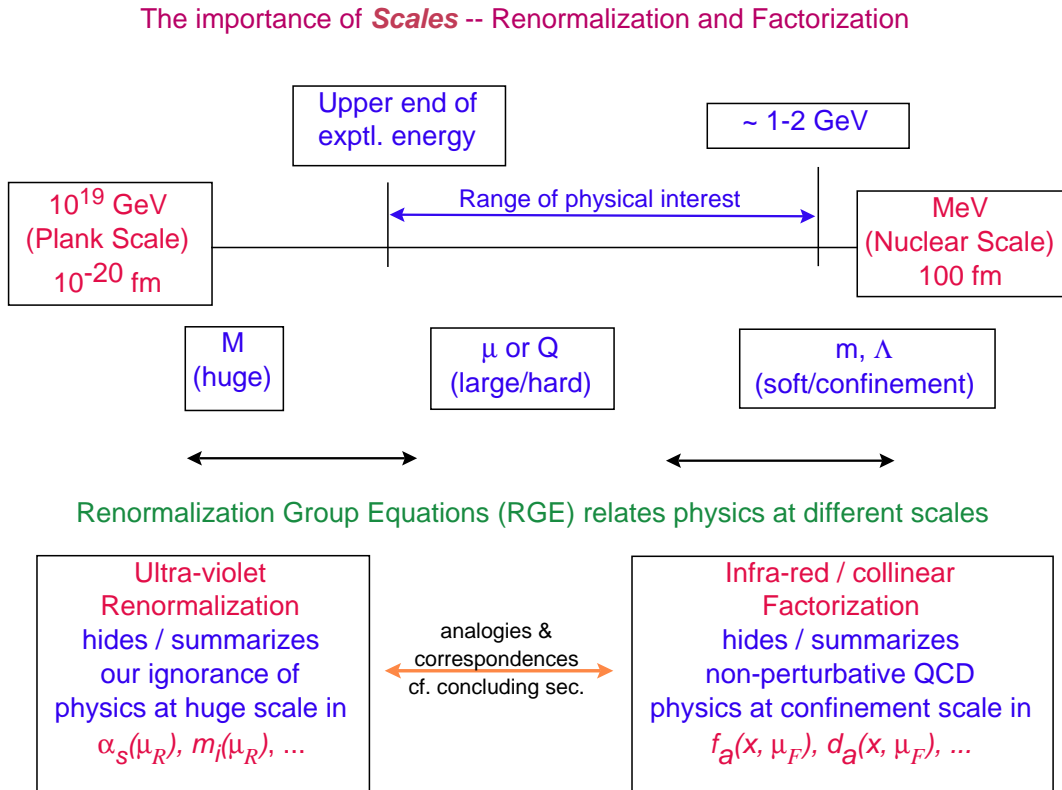


Figure 15: Graphic illustration of the importance of scale transformations, governed by renormalization groups, both for controlling the ultra-violet divergences in renormalization theory, and for the factorization of soft and collinear singularities, which is essential for the validity of the QCD parton model.

To help understand the underlying physics, it is interesting to note the exact correspondences between the bare (partonic) and renormalized (physical) quantities in UV renormalization and IR factorization in the PQCD formalism. They are explicitly displayed in the following table, using the generic notation $f_{b/A}^a(\mu)$ for both PDFs and FFs in the right column.

“Renormalization” and “Factorization”

UV renormalization		Collinear/soft factorization	
A:	Bare Green Func.	$G_0(\alpha_0, m_0, \dots)$	Partonic X-sect F_a
B:	Ren. constants	$Z_i(\mu)$	Pert. parton dist. $f_a^b(\mu)$
C:	Ren. Green Fun.	$G_R = G_0/Z$	Hard X-sect $\hat{F} = F / f$
D:	Anomalous dim.	$\gamma = \frac{\mu}{Z} \frac{d}{d\mu} Z$	Splitting fun. $P = \frac{\mu}{f} \frac{d}{d\mu} f$
E:	Phys. para. α, m	$\alpha_0 Z_i \dots$	Had. parton dist. f_A resummed
F:	Phys sc. amp.	$\alpha(\mu) G_R(m, \mu)$	Hadronic S.F.'s F_A $f_A(\mu) \times \hat{F}(\mu)$

Some common features:

A : divergent; but, independent of “scheme” and scale μ ;

B : divergent; scale and scheme dependent;
universal; absorbs all ultra-violet/soft/collinear divergences;

C & D : finite; scheme-dependent;
D controls the μ dependence of E & F;

E : physical parameters to be obtained from experiment;

F : Theoretical “prediction”; μ -indep. to all orders,
but μ -dep. at finite order n ; $\mu \frac{d}{d\mu} \sim \mathcal{O}(\alpha^{n+1})$

Note: “Renormalization” is factorization (of UV divergences);
“factorization” is renormalization (of soft/collinear div.)

It is interesting to note that, just as the (divergent) renormalization constants are indispensable in the calculation of (finite) renormalized Green functions and anomalous dimension coefficients (which control the RGEs) in renormalization theory, so are the (IR singular) perturbative parton distributions in the calculation of the (IRS) hard cross sections and the splitting functions (which control the evolution equations) in the QCD-based parton model formalism.

4.3 Factorization in Deep inelastic scattering

The crucial role played by deep inelastic scattering (DIS) of leptons on hadrons in the development of the parton model and QCD is well-known. Currently, high precision DIS experiments remain as the mainstay of global QCD analysis. The conventional treatment of DIS in the zero-mass parton formalism can be found in all modern textbooks and reviews. We shall, instead, try to reinforce the important ideas behind IRS and factorization as introduced in the previous section by presenting an unconventional approach to the DIS process in which we keep a small quark mass. A particularly simple calculation in this case provides a concrete and clear physical picture of the factorization of collinear singularities which is quite complementary to the formal textbook approaches and to the discussions of Secs. 4.1-4.2.

Consider the generic leptonproduction process depicted in Fig. 16:

$$\ell_1 + A \longrightarrow \ell_2 + X, \quad (28)$$

where A is a hadron, $\ell_{1,2}$ are leptons, and X represents the summed-over final state hadronic particles. After the calculable leptonic part of the cross section has been factored out, as done in Sec. 4.1, we work with the hadronic process induced by the virtual vector boson γ^* of momentum q and polarization λ :

$$\gamma^*(q, \lambda) + A(P) \longrightarrow X(P_X). \quad (29)$$

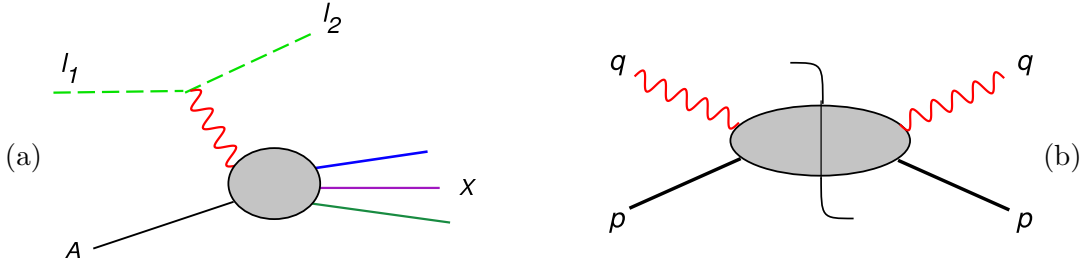


Figure 16: (a) Amplitude for the generic inclusive lepto-production process; (b) The structure functions: squared $\gamma^* + A \rightarrow X$ amplitudes, summed over all final states X .

For the sake of concreteness, we shall explicitly refer to the neutral current interaction with the exchange of a virtual photon γ^* , although our considerations apply to DIS processes induced by W and Z as well. In order to focus on the principles of factorization in this section, we shall skip the details on kinematics, including relations between the cross sections and the structure functions, until Sec. 5.1 when phenomenological issues are discussed. We shall work with the helicity structure functions $F_A^\lambda(x, Q)$, illustrated in Fig. 16b, which are the exact analogue of those of the one-particle inclusive e^+e^- interaction, cf. Fig. 13b and Eq. (22).

The factorization theorem,⁶ states that the inclusive cross section can be written as a convolution:

$$F_A^\lambda(Q^2, x) = \sum_a f_A^a(x, \mu) \otimes \hat{F}_a^\lambda(x, \frac{Q}{\mu}, \frac{Q}{m}, \alpha_s(\mu)) + \mathcal{O}(\Lambda/Q)^r \quad (30)$$

where f_A^a is the distribution of parton a inside the hadron A , \hat{F}_a^λ is the perturbatively calculable hard cross section for $\gamma^* + a \rightarrow X$, r is some positive number, μ denotes collectively the renormalization and factorization scales.

In the real world, we have three “light” quarks (u, d, s) with negligible masses and three “heavy” quarks (c, b, t). The precise definitions of the PDFs and the formulation of factorization will depend on considerations about the relative magnitudes of the factorization scale μ with respect to the quark masses (m_c, m_b, m_t), hence are necessarily non-trivial. We shall examine the relevant issues in Sec. 5.6 on heavy quarks. For the discussion of basic concepts in this section, we shall consider the simplified case of one quark-parton flavor. We keep a non-zero but *small* quark mass m (say, the renormalized \overline{MS} mass $m_r(\mu)$) which serves as a useful cutoff for the collinear and soft singularities associated with quark partons. We will examine the high energy limit as $Q/m \rightarrow \infty$, and study how the singularities arise, and how are they brought under control by factorization.

The perturbative structure functions

Let us examine the first few terms of the perturbative series for the partonic structure functions in DIS. The contributing Feynman diagrams are shown in Fig. 17. To LO (i.e. order α_s^0), the gluon structure functions F_g^λ vanish; and the quark structure functions F_q^λ are calculated from the

⁶In this form, with m also appearing in \hat{F} , it is generalized from the conventional zero-mass one, Eq. (26), to the case including non-zero quark masses (generically denoted by m).^{17,18} Cf. Sec. 5.6.

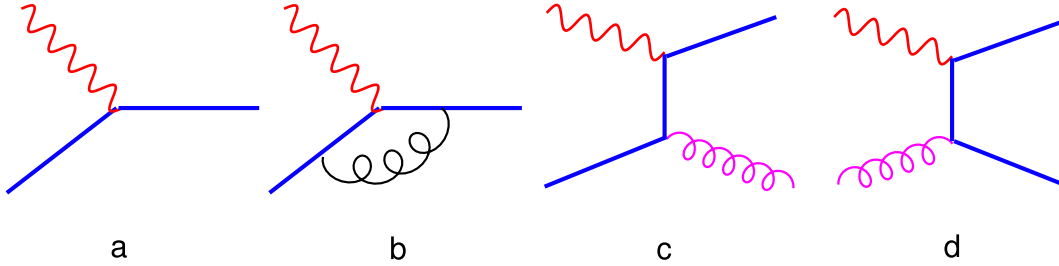


Figure 17: Feynman diagrams contributing to DIS to order α_s : (a) LO quark scattering; (b) NLO vertex correction; (c) NLO quark scattering; and (d) NLO gluon fusion.

square of the simple diagram Fig. 17a. The results are:⁷

$$\begin{aligned}
{}^0F_g^\lambda(x, Q^2) &= 0, \\
{}^0F_q^T(x, Q^2) &= \delta(x-1), \\
{}^0F_q^L(x, Q^2) &= {}^0F_q^{PV}(x, Q^2) = 0,
\end{aligned}
\tag{31}$$

where the superscript ${}^0\{\}$ denotes LO perturbative results. The perturbative PDFs at this order are

$${}^0f_a^b(x, Q^2) = \delta_a^b \delta(x-1), \quad (a, b = q, g). \tag{32}$$

Therefore, the factorization formula, Eq. (30) reduces to the trivial result:

$${}^0F_a^\lambda(x, Q^2) = {}^0\hat{F}_a^\lambda(x, Q^2) \tag{33}$$

with the LHS being given by Eq. (31).

A detailed look at collinear singularity and the physics of factorization – the gluon structure function

In NLO (order α_s), two real ($2 \rightarrow 2$) processes, Fig. 17c,d, and one virtual ($2 \rightarrow 1$) correction term, Fig. 17b, contribute. The two real processes involve different final states, hence don't interfere with each other. We consider the gluon-fusion process, Fig. 17d, first. The calculation is elementary; and the results are simple. These contain illuminating ideas about the physics of collinear singularities and factorization when examined in the proper light. These are what we would like to highlight.

The center-of-mass frame kinematics of the partonic process $\gamma^*(q) + g(k) \rightarrow \bar{q}_1(p_1) + q_2(p_2)$ is illustrated in Fig. 18a and given by the simple formulas:

$$\begin{aligned}
k^\mu &: (k, 0, 0, k), \\
q^\mu &: (E_q, 0, 0, -k), \\
p_1^\mu &: (E, p_T, 0, p_L), \\
p_2^\mu &: (E, -p_T, 0, -p_L),
\end{aligned}
\tag{34}$$

where

$$\begin{aligned}
k &= (s + Q^2)/(2\sqrt{s}), \\
E_q &= (s - Q^2)/(2\sqrt{s}).
\end{aligned}$$

.

⁷An overall constant factor relating to the specific EW couplings, such as e_q^2 (the electric charge squared), has been suppressed for simplicity.

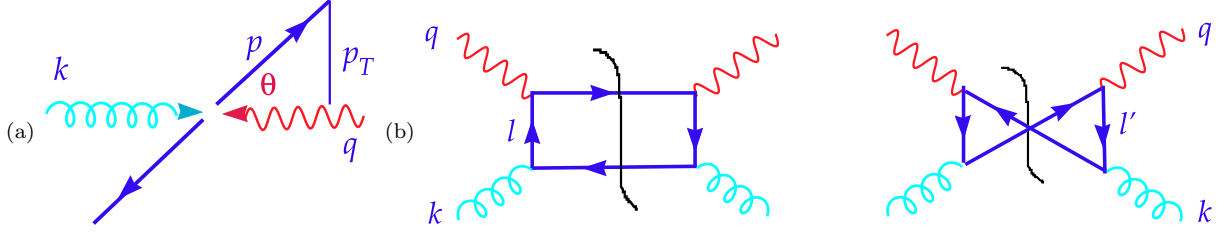


Figure 18: (a) CM kinematics; and (b) Cut diagrams for the gluon fusion process.

The perturbative calculation consists of evaluating the cut diagram Fig. 18b, which involves the integral

$${}^1F_g^\lambda(Q^2, s, m^2) = \frac{\alpha_s}{4\pi} \sum_i \int d\Gamma_2 \frac{\epsilon_\mu^{(\lambda)*}(q, k) \cdot N_i^{\mu\nu} \cdot \epsilon_\nu^{(\lambda)}(q, k)}{(\ell_1^2 - m^2)(\ell_2^2 - m^2)} \quad (35)$$

where

$$\begin{aligned} N_i^{\mu\nu} &= N_i^{\mu\nu}(k, q, p) && \text{(Dirac traces),} \\ \ell_i^2 - m^2 &= (k - p_i)^2 - m^2 = -2k \cdot p_i = 2k(E \mp p_L) = 2k p_i^-, && (36) \\ \int d\Gamma_2 &\approx \int \delta^4(k + q - p_1 - p_2) d^3p_1 d^3p_2 = \int d\cos\theta \text{ or } \int dp_T^2. \end{aligned}$$

The results for this calculation (available in textbooks of QED) are *finite*, — there is *no* UV or IR *divergences* to distract us!⁸ They are, modulo an overall factor of $\alpha_s/2\pi$,

$$\begin{aligned} {}^1F_g^T(Q^2, s, m^2) &= L \frac{(Q^4 + s^2)}{(Q^2 + s)^2} - \frac{2(s - Q^2)^2 p}{(Q^2 + s)^2 \sqrt{s}}, \\ {}^1F_g^L(Q^2, s, m^2) &= \frac{8(Q^2 - m^2)p}{(Q^2 + s)^2 \sqrt{s}} + \mathcal{O}\left(\frac{m^2}{Q^2} L\right), && (37) \\ \text{where } L &= 2 \log\left[\frac{\sqrt{s} + \sqrt{s - 4m^2}}{2m}\right]. \end{aligned}$$

We are interested in these results in the **Bjorken limit**, hence will assume:

$$Q^2 \gg m^2, \quad s \gg m^2, \quad x = \frac{Q^2}{2k \cdot q} = \frac{Q^2}{s + Q^2} \approx \mathcal{O}(1). \quad (38)$$

In this limit, the “finite” partonic structure function ${}^1F_g^T(x, Q^2, m/Q)$ contains the *large logarithm*

$$L = 2 \log\left[\frac{\sqrt{s} + \sqrt{s - 4m^2}}{2m}\right] \longrightarrow \log \frac{s}{m^2} = \log \frac{Q^2}{m^2} \left(\frac{1}{x} - 1\right). \quad (39)$$

Since $\alpha_s L \sim \log(Q/m)/\log(Q/\Lambda) \sim \mathcal{O}(1)$ in the Bjorken limit, this will render the perturbative expansion useless for sufficiently large Q/m . Thus the (bare) partonic structure function ${}^1F_g^T(Q^2, s, m^2)$ is *not IRS*. We see the emergence of the IR “singularity” in a different guise — in the IR unsafe large logarithm $\log(Q/m)$. (We note that ${}^1F_g^L(x, Q^2, m/Q)$ is finite in the limit $m/Q \rightarrow 0$.)

The key question is therefore: Can the potentially troublesome large logarithms be isolated and controlled? The answer is *yes*. The ideas underlying this answer echo those of the zero-mass theory outlined in the previous subsections.

- The large logarithm is due to the collinear region of the momentum phase space, hence is associated with long-distance physics in coordinate space;

⁸That is the reason for choosing to discuss this example.

- The long-distance part is universal; it can be systematically separated (factorized) and resummed into parton distributions;
- After this part is factored out, the remainder (the short-distance part) is free of large logarithms in the $\log(Q/m) \rightarrow \infty$ limit: it becomes the IRS hard-scattering cross section (or Wilson coefficient, in historical parlance).

We show how this works from the analytical results, and present the physical picture behind these results. For this purpose, let us examine the integral of Eq. (35),

$$\begin{aligned}
{}^1F_g^T(x, \frac{m}{Q}) &= \int d\Gamma_2 \frac{N}{(\ell_1^2 - m^2)(\ell_2^2 - m^2)} = \int dp_T^2 \frac{N}{(2k \cdot p_1)(2k \cdot p_2)} \\
&= \int dp_T^2 \frac{N'}{(E - p_L)(E + p_L)} = \int dp_T^2 \frac{1}{E^2 - p_L^2} N' \\
&= \int_0^p \frac{dp_T^2}{p_T^2 + m^2} N'(p_T, x \dots) = \int_0^{\log(s/4m^2)} d\eta N'(\eta, x \dots)
\end{aligned} \tag{40}$$

where $\eta = \log(p_T^2 + m^2)/m^2$, and N' is well behaved in the limits $p_T, \eta \rightarrow 0$ and $m \rightarrow 0$. To see the underlying physics, examine the integrand as a function of p_T and of η , as shown in Fig. 19. The sharp peak at $p_T = 0$ ($p_T \sim m$) is transformed into a broad plateau in η space. We can now

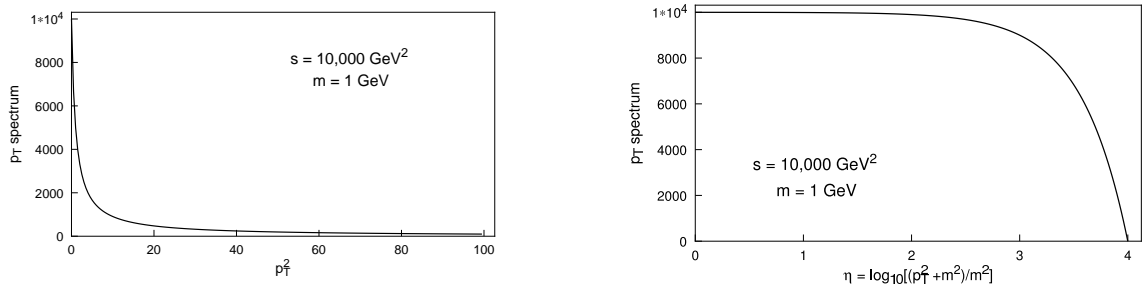


Figure 19: Behavior of the integrand of Eq. (40) as a function of p_T (a), and η (b).

see **the origin of the large logarithm** $\log(Q/m)$. First expand the regular function N' around $\eta = 0$ ($p_T = 0$) and $m = 0$,

$$\begin{aligned}
{}^1F_g^T(x, \frac{m}{Q}) &= N'(x, 0, 0) \int_0^{\log(s/4m^2)} d\eta + \tilde{F}(x, \frac{m}{Q}) \\
&= \frac{\alpha_s}{2\pi} P_g^q(x) \log \frac{s}{4m^2} + \tilde{F}_g^T(x, \frac{m}{Q})
\end{aligned} \tag{41}$$

where one can easily verify $P_g^q(x) = x^2 + (1-x)^2$. The remainder $\tilde{F}_g^T(x, \frac{m}{Q})$ is well-behaved in the Bjorken limit $\frac{m}{Q} \rightarrow 0$. The large logarithm term is seen to originate from the $p_T \sim m$ peak (the collinear kinematic configuration) which corresponds to long-distance interactions in space-time. In the η variable, the large logarithm manifests itself simply as the available kinematic range – the plateau gives the major contribution to the integral.

The **separation of long- and short-distance physics and the meaning of the factorization scale** μ_f is particularly easy to understand in this picture. This is illustrated in Fig. 20. As shown in this picture, the boundary of the two regions is naturally chosen to be at $p_T = \mu_f \sim cQ$ where c is an arbitrary constant of order 1. We note:

- If $Q/m \gg 1$, the plateau is flat and wide – of the order $\log(Q/m)$. The boundary can be chosen anywhere near the upper end of the plateau.
- A shift of the value of μ_f results in shifting a finite term between the long/short distance pieces; the sum, i.e. the bare (or “physical”) structure function, is independent of the choice of μ_f by

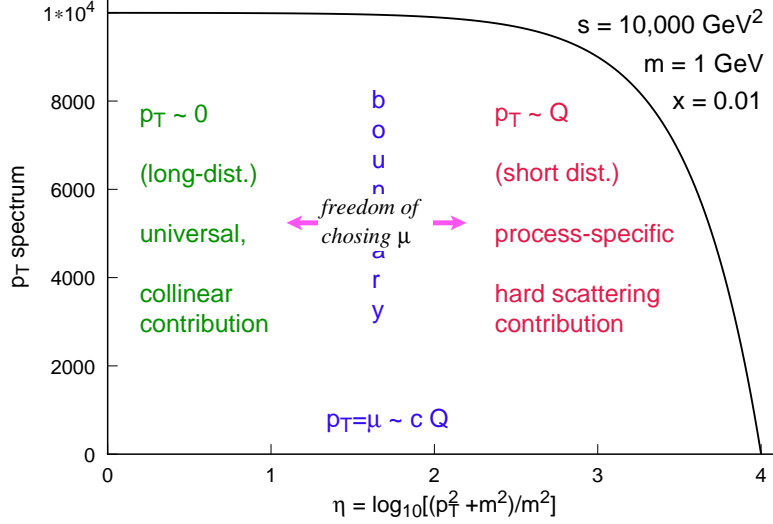


Figure 20: Large $\log(Q/m)$ arises from the width of the plateau, which corresponds to the collinear, $p_T \sim m$, region in p_T space. $p_T = \mu_f \sim cQ$ separates the collinear region from the hard-scattering region. A finite shift in μ_f does not affect the factorization of long- and short-distance physics.

definition. That is, the long/short distance factors are scale (and scheme) dependent; but the net result is scale (and scheme) independent.

- The long-distance ($p_T \sim m$) piece is *universal* – as seen from Eq. (41) and the above illustration, it arises from integrating over the featureless plateau and is independent of details of the NLO process.
- The short-distance ($p_T \sim Q$) piece reflects the specific dynamics of the NLO process. But, with the plateau (collinear region) subtracted, it is free from the large logarithm $\log(Q/m)$ which plague the perturbative expansion when $Q \gg m$ – i.e. *it is IRS*.

The ideas represented by Fig. 20 can be implemented analytically by rewriting Eq. (41) as

$$\begin{aligned}
 {}^1F_g^T(x, \frac{m}{Q}) &= P_g^q(x) \log \frac{\mu_f^2}{m^2} + P_g^q(x) \log \frac{s}{4\mu_f^2} + \tilde{F}_g^T(x, \frac{m}{Q}) \\
 &= P_g^q(x) \log \frac{\mu_f^2}{m^2} + {}^1\hat{F}_g^T(x, \frac{Q}{\mu_f}, \frac{m}{\mu_f}).
 \end{aligned}
 \tag{42}$$

The difference between Eq. (42) and Eq. (41) appears to be slight, but it is far-reaching in principle. Only with the introduction of the intermediate factorization scale μ_f , the two terms on the RHS of Eq. (42) acquire the properties discussed in the above list; and this feature is crucial for the validity of the factorization theorem in general, to all orders of perturbation theory. We also see from Eq. (42) that

- The μ -dependence of the long-distance piece is given by the universal function $P_g^q(x)$ which is the familiar $g \rightarrow q$ splitting function.
- The short-distance piece has a finite limit as m/Q approaches zero; indeed, in this limit it reproduces the conventional zero-mass theory (say, \overline{MS} result), provided attention is given to match the schemes: ${}^1\hat{F}_g^T(x, m/\mu_f, Q/\mu_f) \rightarrow {}^1\hat{F}_g^T(x, Q/\mu_f)|_{m=0}$.⁹

We can now collect the results obtained so far and write them in a form suitable for identifying the perturbative parton distributions and hard cross sections. To order α_s , the perturbative version

⁹For light quarks, it is natural to set $m = 0$ at this stage (or to simply use the zero-mass formalism). For heavy quarks, it is useful to *not* set $m = 0$ in the hard cross section, cf. Sec. 5.6.

of Eq. (30) (cf. also Eq. (24)) for the partonic process $\gamma g \rightarrow q\bar{q}$ suggests that we write

$${}^1F_g^\lambda(x, \frac{Q}{m}) = {}^1f_g^q \otimes {}^0\hat{F}_q^\lambda + {}^0f_g^g(x) \otimes {}^1\hat{F}_g^\lambda. \quad (43)$$

With ${}^0\hat{F}_q^\lambda$ and ${}^0f_g^g(x)$ given by Eqs. 31 and 32, we can identify the NLO parton distribution

$${}^1f_g^q(x, \frac{m}{\mu}, \mu) = \frac{\alpha_s(\mu)}{2\pi} P_g^q(x) \log(\frac{\mu^2}{m^2}). \quad (44)$$

And the formula for the IRS hard cross section is given by

$${}^1\hat{F}_g^\lambda(x, \frac{Q}{\mu}, \frac{m}{Q}) = {}^1F_g^\lambda(x, \frac{Q}{m}) - {}^1f_g^q \otimes {}^0\hat{F}_q^\lambda. \quad (45)$$

Since ${}^0\hat{F}_q^L = 0$, this implies ${}^1\hat{F}_g^L = {}^1F_g^L$ (cf. Eq. (37)). For $\lambda = T$, we reproduce Eq. (42).

Combining the LO formulas (31)–(33) with the NLO Eq. (43), we obtain the multiplicative factorization formula to order α_s :

$$F_g^\lambda(x, \frac{Q}{m}, \alpha_s(\mu)) = f_g^a(x, \frac{m}{\mu}, \alpha_s(\mu)) \otimes \hat{F}_a^\lambda(x, \frac{Q}{\mu}, \frac{m}{\mu}, \alpha_s(\mu)), \quad (a = q, g), \quad (46)$$

where a summation over the repeated index “ a ” is implied, i.e. the RHS of Eq. (46) should be interpreted as a generalized matrix multiplication in parton label space as well as in the convolution integral variable.

Full factorization in NLO and beyond

We need to extend the results obtained for the gluon-fusion contribution (to the DIS structure function) to the general case. Having seen the most basic ideas illustrated by the above example, we shall discuss the rest of the program only in qualitative terms.

At order α_s , one still needs to calculate the contributions from the vertex correction and the quark-scattering diagrams (Fig. 17b,c) to the partonic structure function ${}^1F_q^\lambda(x, \frac{Q}{m}, \alpha_s(\mu))$. The results are more complicated than above: in addition to mass-logarithms, they contain UV and IR singularities. These can be treated in the standard way: one applies UV renormalization (say, using dimensional regularization and \overline{MS} subtraction) to absorb the UV divergences into renormalized masses and coupling; then combines the virtual and real contributions to cancel the IR singularities. The net results are similar to ${}^1F_g^\lambda(x, \frac{Q}{m}, \alpha_s(\mu))$ for the gluon case, except that, in addition to the logs of quark mass m , one also encounters singularities (in the form of $\frac{1}{\epsilon}$ in dimensional regularization) due to long-distance interaction of the massless gluon. For the same physical reasons described above (and in Sec. 4.1-4.2), both of these long-distance contributions are universal, hence can be written in the factorized form, just as for $F_g^\lambda(x, \frac{Q}{m}, \alpha_s(\mu))$, Eqs. (42) and (43).

Going beyond order α_s , one can show that **factorization**, in the sense described above, **holds to all orders of perturbative theory**, for the DIS structure functions.¹⁹ The proof involves showing that a set of *universal* parton distributions exists which will absorb all the collinear and soft singularities encountered in the calculation of the relevant partonic (bare) structure functions $F_a^\lambda(x, \frac{Q}{m}, \alpha_s(\mu))$ ($a =$ all parton flavors). Although the underlying physical ideas are relatively simple, as emphasized in the last two sections, the mathematical proofs are technically very demanding.^{7,15,19} For this reason, actual proofs of factorization only exist for a few hard processes; and certain proofs (e.g. that for the Drell-Yan process) stayed controversial for some time before

a consensus were reached.¹⁵ Because of the general character of the physical ideas and the mathematical methods involved, however, it is generally *assumed* that the attractive *quark-parton model does apply to all high energy interactions* with at least one large energy scale.

The perturbative factorization theorem, *valid to all orders of α_s and for any number of quark flavors*, is thus a simple generalization of Eq. (46). In the case of DIS structure functions:

$$F_b^\lambda(x, \frac{Q}{m}, \alpha_s(\mu)) = f_b^a(x, \frac{m}{\mu}, \alpha_s(\mu)) \otimes \hat{F}_a^\lambda(x, \frac{Q}{\mu}, \frac{m}{\mu}, \alpha_s(\mu)) \quad (a, b = q_i, g). \quad (47)$$

The first factor on the RHS, $\{f_b^a(x, \frac{m}{\mu}, \alpha_s(\mu))\}$, contains all the collinear and soft singularities of the original partonic structure functions $\{F_b^\lambda(x, \frac{Q}{m}, \alpha_s(\mu))\}$, in particular, all large logarithms of the form $\alpha_s^n \log^n(m/\mu)$ to arbitrary order n . This infinite tower of large logarithms are said to have been **resummed** into the parton distributions $\{f_b^a\}$.

As mentioned in Sec. 4.1, the perturbative factorization theorem provides the theoretical basis for the QCD parton model formula used in physics applications. For DIS, we simply *replace the resummed partonic distribution function by the hadronic parton distribution functions*, and obtain:

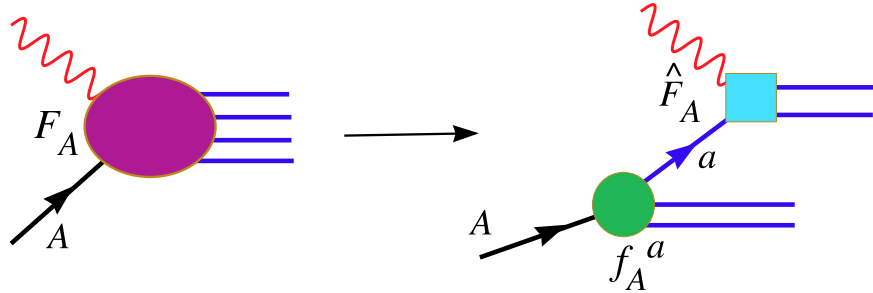


Figure 21: DIS structure functions at high energies: factorization theorem \Rightarrow QCD parton model. See text for comparison with Fig. 14.

$$F_A^\lambda(x, Q, \alpha_s(\mu)) = f_A^a(x, \mu, \alpha_s(\mu)) \otimes \hat{F}_a^\lambda(x, \frac{Q}{\mu}, \alpha_s(\mu)), \quad (a = q_i, g). \quad (48)$$

This provides the basis for the QCD parton picture which is often shown as in Fig. 21. This representation, while conveying the basic ideas conveniently, leaves implicit the squaring of the $\gamma^*A \rightarrow X$ amplitude and the summing over X . The complete picture should be like Fig. 14 in Sec. 4.1.

To use this formula, one needs the perturbative hard cross section $\hat{F}_a^\lambda(x, \frac{Q}{\mu}, \alpha_s)$ (“Wilson coefficients”). To calculate these, one reverts back to the partonic cross section formula, such as Eq. (46), which can be written, in matrix notation:

$$\{\hat{F}^\lambda\}(x, \frac{Q}{\mu}, \alpha_s(\mu)) = f^{-1}(x, \frac{m}{\mu}, \alpha_s(\mu))|_{\text{PQCD}} \otimes F^\lambda(x, \frac{Q}{m}, \alpha_s(\mu))|_{\text{PQCD}} \quad (49)$$

where we used $\{\}$ to denote a matrix in the suppressed parton flavor label. Both perturbative factors on the RHS are to be calculated, independently, to the same order of perturbation theory, using the same renormalization scheme. As mentioned earlier, $F^\lambda(x, \frac{Q}{m}, \alpha_s(\mu))$ is, by definition, independent of the choice of factorization scheme and scale. These only come in when one defines the perturbative partonic parton distributions $f_b^a(x, \frac{m}{\mu}, \alpha_s(\mu))$. Equation (49) shows explicitly that the hard cross section $\hat{F}_b^\lambda(x, \frac{Q}{\mu}, \alpha_s(\mu))$ inherits the choices of factorization scheme and scale made for the parton distributions. Thus, we need to discuss the general definition of the universal parton distributions, independent of any specific process.

4.4 Parton distribution functions

Historically, factorization was formulated first in *moment space*, in terms of Mellin transforms of the structure functions, using Wilson’s operator product expansion. In that formulation, parton distribution functions are the inverse Mellin transform of the matrix elements of an infinite tower of local operators. In the more physical (Bjorken) x -space formulation we are adopting, an equivalent definition of PDFs can be given in terms of matrix elements of bi-local operators on the light-cone.²⁰ The distribution of quark “ a ” in a parent “ A ” (either a hadron or another parton) is defined as

$$f_A^a(\xi, \mu) \equiv \frac{1}{2} \int \frac{dy^-}{2\pi} e^{-i\xi p^+ y^-} \langle A | \bar{\psi}_a(0, y^-, \mathbf{0}) \gamma^+ F \psi_a(0) | A \rangle. \quad (50)$$

$|A\rangle$ represents the parent state A , with the momenta aligned so that $p_a^T = p_A^T = 0$ and $p_a^+ / p_A^+ = \xi$. The operator in the middle,

$$F = \mathcal{P} \exp(-ig \int_0^{y^-} dz^- A_a^+(0, z^-, \mathbf{0}) t_a),$$

ensures the gauge invariance of the definition. In the physical gauge, $A^+ = 0$, F becomes the identity operator, and $f_A^a(\xi)$ becomes manifestly the matrix element of the *number operator* for finding quark “ a ” in A with momentum $p_a^+ = \xi p_A^+$ and $p_a^T = 0$.

The definition for the gluon distribution is similar; one replaces the quark field by suitable combinations of the gluon field A^μ , cf. Ref. 20. The μ dependence, shown on the LHS, arises from the need to regulate the divergences encountered in the perturbative calculation of the “bare” matrix element on the RHS. For the conventional zero-mass quark formalism, it is convenient to use dimensional regularization and \overline{MS} subtraction which regulate both the UV and the IR singularities at once. In that case, one obtains PDFs defined in the \overline{MS} scheme, and μ is just the scale variable introduced by dimensional regularization. As emphasized in our general discussions about factorization, in principle, one is free to choose any well-defined scheme in defining PDFs, as long as consistency is maintained with the hard cross section. Any such choice is related to the \overline{MS} scheme by a finite renormalization.

The PDFs, like the fragmentation functions, satisfy a RGE – the *QCD evolution* (or DGLAP) equation,

$$\frac{d}{d \ln \mu} f_A^a(x, \mu) = \sum_b \int_x^1 \frac{d\xi}{\xi} P_b^a\left(\frac{x}{\xi}, \alpha_s(\mu)\right) f_A^b(\xi, \mu). \quad (51)$$

Because P_b^a is independent of the target A , it can be calculated order-by-order in perturbation theory from the partonic PDFs,

$$P_{ab}(z, \alpha_s(\mu)) = P_{ab}^{(1)}(z) \frac{\alpha_s(\mu)}{\pi} + P_{ab}^{(2)}(z) \left(\frac{\alpha_s(\mu)}{\pi}\right)^2 + \dots \quad (52)$$

$P_{ab}^{(1)}(z)$ and $P_{ab}^{(2)}(z)$ have been known for a long time. $P_{ab}^{(3)}(z)$ has not yet been completely calculated, but its large and small x limits, as well as many moments are known.²¹ These results have been used extensively in determining the μ dependence of the non-perturbative hadronic PDFs and FFs.

4.5 Scale-dependence of the factorization theorem based parton model

Although, in principle, the factorized formula for $F_A^\lambda(x, Q)$ should be independent of the scale μ , this is *not* true if \hat{F}_A^λ and P_{ab} are only calculated to some finite order in the perturbative expansion.

In other words, at finite order, F_A^λ is actually a function of μ , in addition to (x, Q) . For the perturbative results to be reliable, the variation with respect to μ has to be under control. It is easy to see that, if the calculation has been carried out to order α_s^n , then

$$\mu \frac{d}{d\mu} F_A^{(n)}(x, Q, \mu) \sim \mathcal{O}(\alpha_s^{n+1}). \quad (53)$$

Equation (53) can be used as a tool: when the order α_s^{n+1} calculation is not available, the μ -dependence of the order α_s^n result, $F_A^{(n)}(x, Q, \mu)$, gives an indication of the size of the next order term. In practice, the size of the μ -dependence of NLO calculations of various hard processes vary greatly. It is small for DIS and DY processes, indicating these results are likely to be reliable. But, it turns out to be quite large for direct photon and heavy quark production, indicating that, for these processes, important contributions to the cross sections are still missing from the two leading terms in the expansion. On one hand, these results clearly have important phenomenological consequences, as we will discuss in the later sections. On the other hand, they pose interesting theoretical challenges to understand the source of these shortcomings.

4.6 Three faces of the master formula of QCD parton model

As mentioned in Sec. 4, the applications of PQCD largely rely on the factorization-theorem-based parton model of high energy interactions. On one hand, by applying this picture to a set of SM processes at currently available energies, it allows us to probe hadron structure and determine the universal PDFs and FFs. This is represented by writing the factorization formula, Eq. (48), in the generalized matrix notation, as

$$\{f_A\}(x, \mu) = \{\hat{F}_\lambda\}^{-1}(x, \frac{Q}{\mu}, \alpha_s(\mu))|_{\text{PQCD}} \otimes F_A^\lambda(x, Q)|_{\text{expt}} \quad (54)$$

where the sum over λ on the RHS symbolizes the use of a set of complementary experimentally measured quantities, such as DIS structure functions and hadron-hadron hard scattering cross sections. We shall refer to this program as *global QCD analysis*.

On the other hand, making use of the universal PDFs and FFs so determined, we can predict the cross sections for both SM and New Physics processes at any energy that may be of interest now or in the future, using the original Eq. (48).

To summarize: the **significance of the factorization theorem** is underlined in the remarkable fact that all three facets of the same equation play an important role in our physics program:

- Applications: in the form Eq. (48), to predict all SM and New Physics processes, using theoretical hard cross sections and the phenomenological PDFs and FFs as input;
- Theory: in the form Eq. (49), to derive the IRS hard cross sections, using calculations of the partonic cross sections and partonic PDFs (the latter as “subtractions” to remove the collinear and soft singularities), in perturbative QCD, to some order of α_s ; and
- Phenomenology: in the form Eq. (54), to determine the PDFs and FFs in global QCD analysis, using the hard cross sections and experimental data as input.

Thus, the factorization theorem formula deserves the alternative name: the *master formula of the QCD parton model*.

5 Hard Processes in Hadron Interactions

We shall briefly survey in this section the common SM hard processes in lepton-hadron and hadron-hadron collisions. Treatment of these processes in the traditional zero-mass QCD parton model can

be found in Refs. [4,5,6]. We will therefore limit ourselves to a relatively informal perusal of issues either of historical significance, or of unusual physical interest, or of particular relevance to current PQCD research – all to lay the ground work for the review of the phenomenological program of global QCD analysis in the next section.

5.1 Deep inelastic scattering

The most important of the hard processes, both conceptually and phenomenologically, is inclusive DIS of charged and neutral leptons on hadrons,

$$\ell_1(k) + A(p) \rightarrow \ell_2(k') + X$$

with the exchange of a vector boson V . Cf. Fig. 16a. The conceptual aspect has already been discussed in Sec. 4.3 in the context of the principle of factorization. We shall address the relevant phenomenological issues in this section.

Preliminaries The standard variables used to describe this process are:

$$\begin{aligned} q^\mu &= k^\mu - k'^\mu & ; & & Q^2 &= -q^2, \\ x &= Q^2/2p \cdot q & ; & & y &= p \cdot q/p \cdot k = E - E', \\ \nu &= q \cdot p & ; & & W^2 &= (q + p)^2 = \frac{1-x}{x}Q^2 + m_A^2. \end{aligned} \quad (55)$$

The cross section is expressed in terms of the leptonic and hadronic tensors as:

$$d\sigma = \frac{4\alpha^2}{s} \frac{d^3\mathbf{k}'}{2|\mathbf{k}'|} \frac{1}{(q^2 - M_V^2)^2} L^{\mu\nu}(k, q) W_{\mu\nu}(p, q) \quad (56)$$

where M_V is the mass of the exchanged vector boson. For current lepton-hadron scattering phenomenology, we need only to consider $V = \gamma^*, W^+, W^-$. Then there is no interference term in any of the neutral current (γ^*) or charged current (W^\pm) interaction channels. The lepton tensor $L^{\mu\nu}$ as well as the hadron tensor $W_{\mu\nu}$, expressed in terms of invariant structure functions $F_i(x, Q)$, $i = 1, 2, 3$, are given in all standard references. We shall use the helicity basis which is more physical and somewhat less familiar. In this basis,

$$W_{\lambda\sigma}(q, P) = \frac{1}{4\pi} \sum_X \langle P | \epsilon_\lambda^* \cdot J^\dagger | P_X \rangle (2\pi)^4 \delta^{(4)}(P + q - P_X) \langle P_X | \epsilon_\sigma \cdot J | P \rangle \quad (57)$$

where \sum implies a sum over all final hadronic states as well as averaging over the initial target spin, and ϵ_λ represents the polarization 4-vector of the vector boson with helicity λ . In most cases, only the diagonal elements of the tensor $F^\lambda \equiv W_{\lambda\lambda}(q, P)$ contribute to the measured cross section. In analogy to Eq. (23), the cross section formula for the DIS process acquires an elegant and precise form (valid at all energies):

$$\begin{aligned} \frac{d\sigma}{dx dy} &= N \left\{ g_+^2 [F_T (1 + \cosh^2 \psi) + F_L \sinh^2 \psi] + g_-^2 [F_{PV} \cosh \psi] \right\}, \\ N &= \frac{yQ^2}{2\pi n_\ell} \frac{g_V^4}{(Q^2 - M_V)^2}, \end{aligned} \quad (58)$$

where $F_T = \frac{1}{2}(F_{\lambda=+} + F_{\lambda=-})$, $F_L = F_{\lambda=0}$, and $F_{PV} = F_- - F_+$, $n_\ell = \{2, 1\}$ for incident {charged lepton, neutrino} respectively, g_V is the gauge coupling of the vector boson V , M_V is its mass, $g_{+/-}^2$ are the lepton parity conserving/violating electroweak coupling combinations $g_\pm^2 = g_L^2 \pm g_R^2$

(R/L = right/left-handed). And ψ is the hyperbolic angle of the Lorentz boost connecting the lepton vertex to the hadron vertex in the Breit frame (“rest frame” of the space-like vector boson, $q^0 = q_T = 0, q_3 = Q$), which is the analogue of the angle of rotation θ between the lepton and hadron vertices in the rest frame of the time-like vector boson in e^+e^- scattering, as seen in Sec. 4.1. The hyperbolic angle ψ is related to the familiar kinematic variables by

$$\cosh \psi = \frac{E_1 + E_2}{\sqrt{Q^2 + \nu^2}} \xrightarrow{m_A \rightarrow 0} \frac{(2-y)}{y}. \quad (59)$$

The relations between the helicity and invariant structure functions are relatively simple:

$$\begin{aligned} \textit{Transverse} : \quad F_T &= F_1, \\ \textit{Longitudinal} : \quad F_L &= -F_1 + (1 + Q^2/\nu^2) \frac{F_2}{2x} \sim -F_1 + \frac{F_2}{2x}, \\ \textit{Parity violating} : \quad F_{PV} &= \sqrt{1 + Q^2/\nu^2} F_3 \sim F_3, \end{aligned} \quad (60)$$

where the last column is valid only in the Bjorken limit.

Phenomenology Extensive deep inelastic scattering experimental data have been accumulated from all major laboratories (SLAC, Fermilab, CERN, HERA), using electron, muon, neutrino, and anti-neutrino beams on a wide variety of targets.²² The accuracy of these data has steadily improved; and the kinematic range they cover has steadily expanded. (Cf. Sec. 6.) These data form the bedrock on which global QCD analysis is built.

On the theory side, the hard cross section has been calculated to NNLO (2 loop). As mentioned in Sec. 4.5, although the corresponding calculation for the evolution kernel has not yet been completed, much of its behavior is known. The important thing is that the available theoretical results show that the perturbative results are very well-behaved. Except at very small x (where the process becomes effectively a two-scale problem because of the large $\log(1/x)$ terms), the convergence of the perturbative expansion is good, and the scale-dependence is small.

Although PQCD cannot predict the x -dependence of the PDFs, the evolution equation, Eq. (53), does allow us to calculate the Q -dependence, with some input PDFs at a given Q_0 . This Q -dependence has been verified by experiment to a very high degree of accuracy. Figure 22 gives an illustration of the quality of this remarkable agreement in neutral current $F_2(x, Q)$ structure function measured over a large range of x and Q by fixed target experiments SLAC, BCDMS, NMC and collider experiments H1, ZEUS; as well as in charged current $F_3(x, Q)$ measured by the CCFR neutrino experiment.

With precision data covering a wide kinematic range and reliable theoretical predictions, PQCD phenomenology in DIS is a very rich subject. In addition to the example given above, one can test a number of QCD sum rules; make precision measurements of the fundamental coupling α_s ; study semi-inclusive final state channels; as well as the best known application – as the main input to global QCD analysis in order to determine the quark and gluon content of hadrons, in particular the nucleon. For a review of DIS phenomenology, cf. Ref. 22.

5.2 Hadron-hadron collisions in general

For hadron-hadron collisions, we consider the inclusive production of massive vector bosons $\gamma^*/W/Z$, heavy quarks Q , high p_T direct photons γ , and high p_T Jets. These processes can be generically represented by $A(p_A) + B(p_B) \rightarrow H(q) + X$, where H is the detected “hard” particle, X is “anything,” and the arguments are the associated moment variables. In these processes, it is convenient

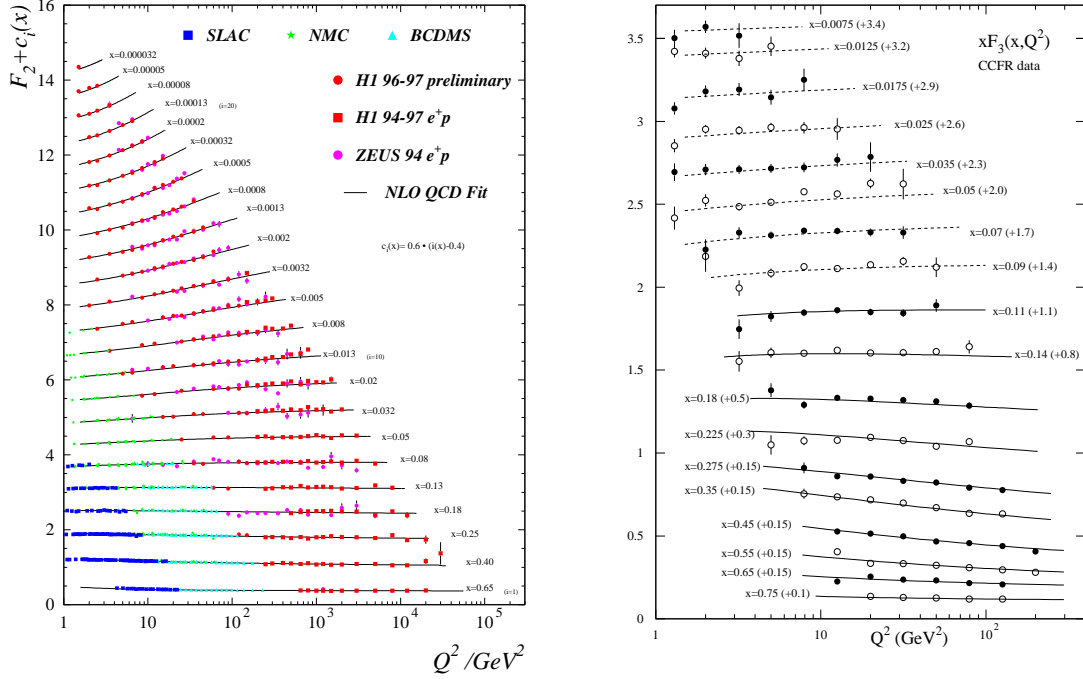


Figure 22: Comparison of DIS data with NLO PQCD calculations: (a) F_2 data from several neutral-current experiments; (b) xF_3 data from the CCFR experiment.

to start with the CM frame with z-axis along the beam of the colliding hadrons, and adopt the light-cone momentum components (cf. Eq. (10)). For a particle with mass M and momentum q : $q^\mu = (q^+, q^-, \mathbf{q})$, define the rapidity variable

$$y = \frac{1}{2} \log \left(\frac{q^+}{q^-} \right), \quad (61)$$

then

$$q^\mu = (e^y \sqrt{(\mathbf{q}^2 + M^2)/2}, e^{-y} \sqrt{(\mathbf{q}^2 + M^2)/2}, \mathbf{q}). \quad (62)$$

Transformation under a boost along the z-axis ($q^+ \rightarrow e^\omega q^+$, $q^- \rightarrow e^{-\omega} q^-$, $\mathbf{q} \rightarrow \mathbf{q}$) results in a uniform translation in the rapidity variable $y \rightarrow y + \omega$. This is convenient, since the boost invariance of many physical quantities is simply expressed as the independence of those variables with respect to the absolute value of y (i.e. only rapidity differences matter).

Now we turn to the individual processes.

5.3 Lepton-pair and W/Z production (Drell-Yan processes)

The Drell-Yan process $A + B \rightarrow \gamma^*/W/Z + X$ is depicted in Fig. 23, along with the associated factorization-based parton picture at higher energies. We shall use the symbol V to represent the (virtual and real) vector bosons collectively. Let M be the mass of the vector boson W/Z or the invariant mass of the lepton pair ($M^2 = q^2$), $x_A = e^y \sqrt{M^2/s}$, $x_B = e^{-y} \sqrt{M^2/s}$, then the factorization formula reads

$$\frac{d\sigma}{dy} = \sum_{a,b} \int_{x_A}^1 d\xi_A \int_{x_B}^1 d\xi_B f_A^a(\xi_A, \mu) f_B^b(\xi_B, \mu) \frac{d\hat{\sigma}_{ab}(\mu)}{dy} + \mathcal{O}\left(\left(\frac{m}{M}\right)^p\right). \quad (63)$$

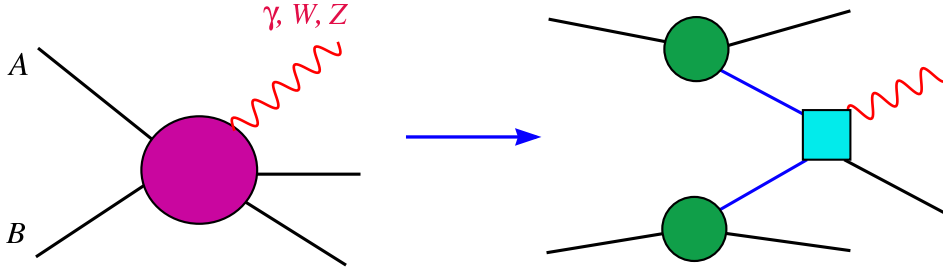
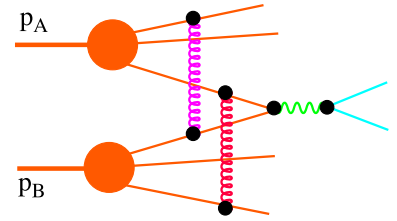


Figure 23: Factorization-based parton picture for the Drell-Yan process.

The **factorization formula for the DY process** is among the few hadron-hadron process which has actually been proved.

The complication (over those for lepton-lepton and lepton-hadron processes) arises from initial state strong interactions, as illustrated in the figure to the right – factorization does not hold graph-by-graph, as shown in the example of Sec. 4.3. The validity of factorization is, however, saved by the intricate interplay between different graphs connected by soft gluons which reflect the physical requirements of unitarity, causality, and gauge invariance of the underlying theory.¹⁵



The DY process has been pivotal in the development of the QCD parton model. The dominant contribution to the DY cross section comes from the LO quark-anti-quark annihilation partonic process $q\bar{q} \rightarrow V$, Fig. 24a. The qualitative agreement between the measured DY cross sections with

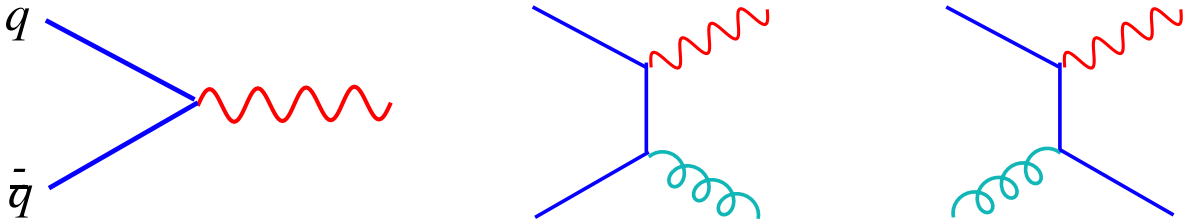


Figure 24: Feynman diagrams for (a) LO, and (b) NLO partonic processes contributing to the physical DY process.

the predictions of the LO (**simple parton model**) formula (Eq. (63) in order α_s^0), using PDFs determined from DIS experiments, was considered a major success for the original parton model idea, since it was *decisive experimental evidence* for the idea of factorization involving universal parton distributions in two entirely different processes.

The **NLO partonic processes** are $q\bar{q} \rightarrow Vg$ and $gq \rightarrow Vq$ (“Compton scattering”), as shown in Fig. 24b,c. Their contribution to the physical cross section turned out to be rather large – the “K-factor” $\equiv \frac{NLO}{LO}$ (a common measure of the relative significance of the NLO contribution) is of the order ~ 2.0 . This posed two potential problems for the QCD parton model:

- (i) doubt was cast on the trustworthiness of the perturbation expansion;
- (ii) the “agreement” between the first naive prediction and experiment mentioned above was put in jeopardy by including the NLO contribution.

These problems were resolved: (i) the origin of the large NLO contribution was identified, and understood not to be a problem for higher order terms (this has been confirmed both by the actual calculation of the NNLO term, and by the fact that the NLO results are relatively insensitive to

variations of the factorization scale, cf. Sec. 4.5); and (ii) the “disagreement” turned out to be actually closer to a factor of 3 – which was, however, exactly what was needed to bring theory and experiment into *agreement*, since the initial prediction predated the advent of the color degree of freedom. In other words, the comparison of theory with experiment in DY turned out to be one of the crucial elements in support of the color quantum number!

Current NLO and NNLO calculations of DY cross sections are in perfect agreement with the most recent data; and these play an important role in the global QCD analysis program, cf. Sec. 6. In Fig. 25, we show some typical results: the comparison between two lepton-pair production

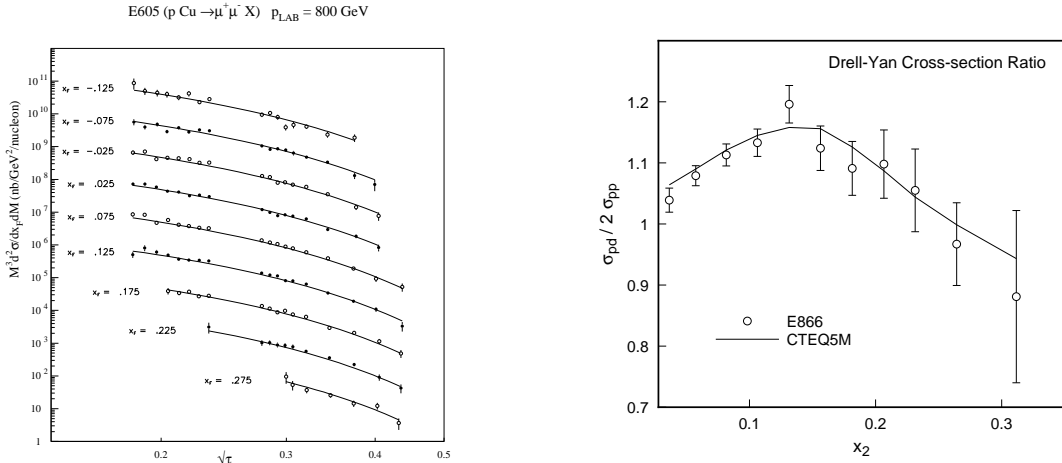


Figure 25: Comparison of two Fermilab lepton-pair production experiments with PQCD: (a) $d\sigma/dy dQ^2$ (E605) vs. MRST98 curves; and (b) $\sigma^{pd}/2\sigma^{pp}$ (E866) vs. CTEQ5 curve.

experiments from Fermilab, E605 on $d\sigma/dy dQ^2$ and E866 on $2\sigma^{pp}/\sigma^{pd}$, with a NLO QCD global fit.²³

In addition to the rapidity distribution (Eq. (63)) one can calculate the q_T distribution of the produced vector boson. Since the naive Drell-Yan mechanism produces only $q_T = 0$ vector bosons, the leading contribution at finite q_T comes in at order α_s , due to the diagrams of Fig. 24b,c. The perturbatively calculated results for these contributions, however, diverge as $q_T \rightarrow 0$. This kind of singularity appears as logarithm terms of the form $\log(q_T/M)$, which becomes large when the two physical energy scales q_T and M become very disparate, e.g. when $q_T/M \ll 1$ ($q_T \ll M$). The possible ways to control this apparent singularity are rooted on ideas discussed in the previous sections:

- By integrating over q_T , and combining with the contributions from virtual corrections to the $q\bar{q}$ annihilation subprocess, the $d\sigma/dy$ distribution is finite. This is reminiscent of the cancellation of collinear and soft divergences in IRS quantities in $e + e -$ collision discussed in Sec. 3.3.
- On the other hand, if we are actually interested in the q_T distribution at values of $q_T \ll M$, the large logarithm terms (of the form $\alpha_s^n \log^{2n-m}(q_T/M)$ at the n-loop level) must be brought under control by resummation.¹⁰ This was the first example of the need for **resummation in a multi-scales problem**. The theory and phenomenology of Q_T -resummation for the DY process are, by now, well established.²⁴ Figure 26 shows the comparison of the W p_T distribution measured at the Tevatron collider compared with resummed QCD calculations. We have encountered a different

¹⁰This reminds us of the resummation of large logs of the type $\alpha_s^n \log^n(m/\mu)$ to obtain the parton distributions, cf. Sec. 4.3. The general idea may be similar, but the underlying physics is different. In this case, these large logs resum into the Sudakov form factor.²⁴

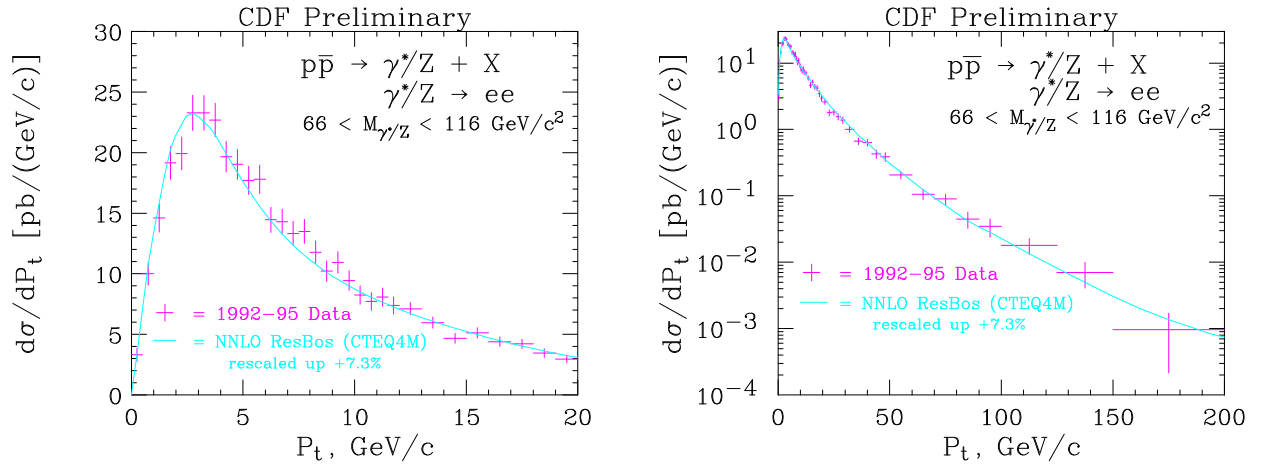


Figure 26: Comparison of Z q_T distribution at the Tevatron with p_T -resummed PQCD calculations: (a) low q_T region; (b) full q_T range. Figure by C. Balas in Ref. 29

type of resummation – the threshold resummation – in our brief discussion of the thrust distribution in Sec. 3.4; the issue will also return in the next subsection.

5.4 Direct photon production

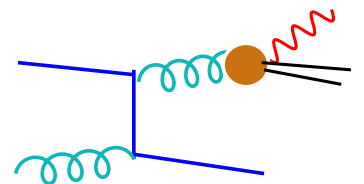
Direct photon production, $A + B \rightarrow \gamma + X$, is an interesting process for PQCD, provided the (real, zero-mass) photon is observed at high transverse momentum, $q_T \gg \Lambda_{QCD}$.



In principle, then, q_T provides the hard scale which makes asymptotic freedom and factorization applicable. The leading order partonic processes for this reaction are shown in the diagrams to the left. They are the same ones shown as Fig. 24b,c for the DY process.

Historically, direct photon production has been regarded as a primary process to probe the gluon parton distribution of the nucleon, because the cross section is directly proportional the initial state gluon *at leading order* – in contrast to the situation in DIS and DY where the gluon is involved only at NLO. Unfortunately, as we have learned over the past 15 years, there are a number of special circumstances that complicate the situation; hence the original expectation remains an unfulfilled goal. We mention three of these.

- Since we are discussing *inclusive* photon production, in addition to the partonic processes involving a point-like (“direct”) photon shown above, there is an additional contribution from hadronic (quark and gluon) subprocess with one of the final state partons *fragmenting* into a photon, such as shown in the accompanying graph.



This *hadron-like* component of the produced photon is sometimes called by the (rather confusing) name “resolved photon”; and the contribution from this new mechanism is called the **bremstrahlung contribution**. It can be shown that, at higher orders, the distinction between the two components is not unique; they are inter-related and dependent on the factorization scheme and scale choices. The presence of this additional contribution complicates both the theory and the phenomenology.

- Calculations show that, in energy ranges relevant for current fixed-target experiments, the NLO contribution to the direct photon cross section is quite large relative to the LO one; the K-factor is of the order ~ 2 . In addition, the scale-dependence of the results, even at NLO, is quite significant, indicating that important contributions to the perturbation series are still missing (cf. Sec. 4.5). Both imply that the NLO calculation does not provide a reliable theoretical basis for quantitative phenomenology. Recent calculations indicate that the scale-dependence is reduced by resummation.²⁵ That is still an evolving field of research.

- The q_T spectrum, both theoretically and experimentally, has a very steep dependence on q_T . In the QCD parton model, this fact makes the theoretical prediction extremely sensitive to small broadening of the initial state parton transverse momentum (usually denoted by k_T) away from the parton-model value of $k_T = 0$. This effect is shown in the accompanying illustration. The net effect on the p_T of the γ is to lift and steepen the curve by an amount depending on the steepness of the original spectrum and on the amount of k_T broadening applied to the parton. Phenomenologically, it was noticed a few years ago²⁶ that measured p_T spectra from fixed-target to collider experiments exhibit a systematic pattern of deviation from those expected from NLO PQCD calculations, in a manner consistent with k_T broadening effect. This pattern is shown in Fig. 27a.

A recent high statistics experiment, E706 at Fermilab, reinforced this observation. The measured cross section is approximately a factor of 3 larger than the NLO calculation; and a k_T broadening effect of the order of 1.3 GeV convoluted with the NLO calculation brings about a good agreement, as shown in Fig. 27b.

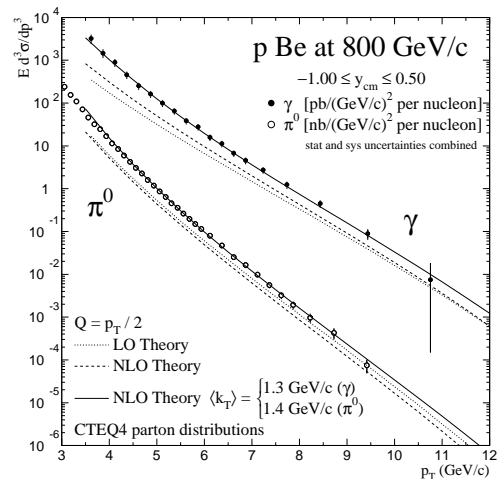
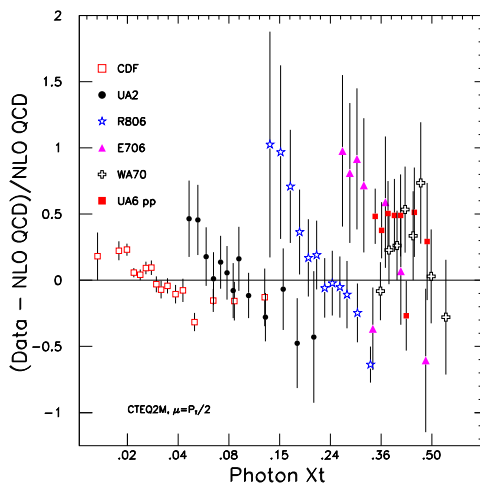
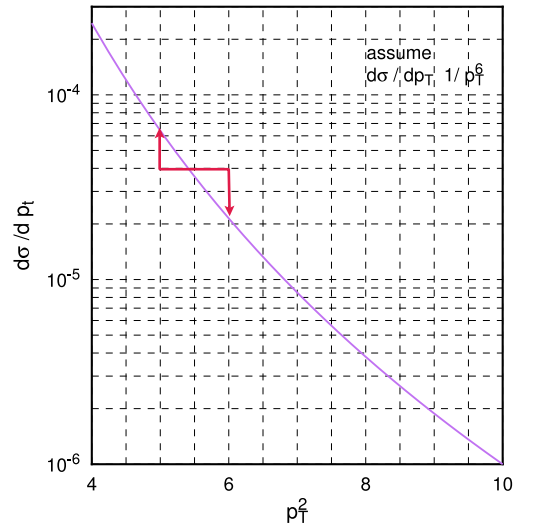


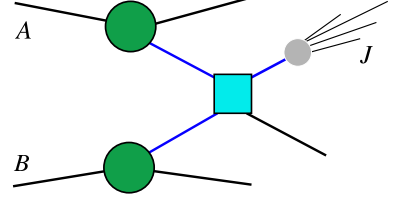
Figure 27: (a) Global comparison between direct photon production data with NLO calculation in terms of their ratio, exhibiting the systematic pattern of stiffening of the measured q_t spectrum;²⁶ (b) Recent E706 data compared to NLO calculation, with and without k_T broadening effect.²⁷

It is natural to think of a k_T broadening effects, as proposed in Ref. 26, since the parton model value $k_T = 0$ is only an idealization brought about by factorization — recall Eqs. (41) and

(42) and Fig. 20. In particular, it is well-known that multi-soft-gluon emissions can produce just such an effect. Theoretically, it is precisely these effects that give rise to the q_T -resummation. This realization has stimulated a great deal of theoretical activity in recent years on putting resummation theory for direct photon production on a firmer basis.²⁵ The theory and phenomenology both remain as one of the most active areas of current QCD research.

5.5 Inclusive jet production

The inclusive jet production process, $A + B \rightarrow jet + X$, can be represented by the parton model picture as shown here. Although, at high energies, the appearance of “jets” in the experimental detectors appears to be obvious to the eye as shown in Sec. 2.1, for quantitative comparison between theory and experiment, one must adopt specific *jet algorithms* which are IRS (hence calculable in PQCD). The corresponding formula is



$$\frac{d\sigma}{dE_T d\eta} \approx \sum_{a,b} \int_{x_A}^1 d\xi_A \int_{x_B}^1 d\xi_B f_A^a(\xi_A, \mu) f_B^b(\xi_B, \mu) \frac{d\hat{\sigma}^{ab}(\mu)}{dE_T d\eta} \quad (64)$$

where η is the *pseudorapidity* defined as $\eta = -\log(\tan(\theta/2)) \approx y$ if q^+ (or q^-) $\gg m$.

There are many viable definitions of jet algorithms. Historically, they fall into two broad categories:^{4,28} (i) cone algorithms, based on energy deposition in specified solid angle areas; and (ii) cluster algorithms, based on combining particle momenta with appropriate IRS recipes. In the former category, in addition to the original Serman-Weinberg prescription, the “Snowmass accord” algorithm (and modified versions of it) have been used extensively in hadron-hadron collision studies. In the latter category, the JADE algorithm and its modern variants, such as the k_T (Durham) algorithm, have been the most used in e^+e^- jet studies. Although all IRS jet algorithms are equally valid in principle, the modern definitions have been designed to be more “physical” (e.g. jet separations agree more with intuitive pictures of jets) and more efficient to implement (so that, e.g. higher-order corrections are minimized, or resummations are easier to formulate, ...).

The NLO PQCD calculation of the one jet inclusive cross section is known to be quite reliable. Scale dependence of the calculated results are mild over most of the kinematic range. Experimentally, inclusive jet production at the Tevatron provides the highest reach in momentum scale, ~ 500 GeV, of all high energy hard scattering, hence probes hadron structure at the shortest distance scale. Figure 28 shows the comparison of data from the CDF experiment with PQCD calculations based on the CTEQ parton distributions. The bottom part compares the data with two sets of candidate parton distributions. Considering the systematic errors on the experimental data points, indicated near the bottom of the plot, both are consistent with data. This is generally reassuring.

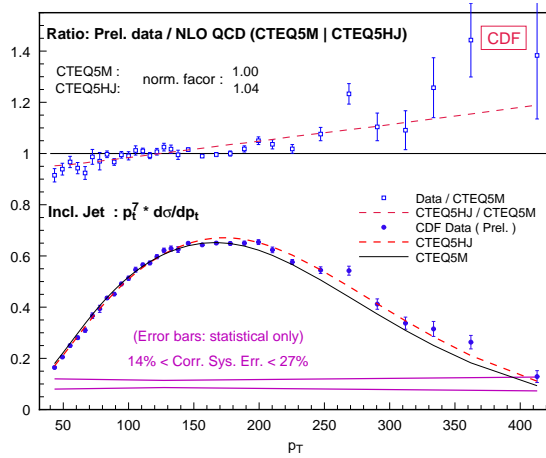


Figure 28: Comparison of one jet inclusive cross-section from the CDF experiment with two CTEQ5 calculations.

On the other hand, it was noticed that the trend of the data shows an “excess” over the

CTEQ5M curve which has a conventional type of gluon distribution. This is highlighted in the top part of the plot in the form of the ratio of Data/Theory. This excess initially caused a great deal of excitement in the HEP community, because, if true, it would indicate the emergence of some new physics signal at the highest energy scale explored by HEP experiments. However, the existence of an alternate set of PDFs, CTEQ5HJ, which can bring about better agreement between theory and experiment (dashed lines), means that we need more constraints on the PDFs before signals for new physics can be unambiguously established. Figure 29 shows more recent measurements on inclusive jet p_T distributions at several different η bins (double differential cross-section) by the D0 collaboration. This data set is very precise, and the comparison to NLO QCD calculations based on the CTEQ4HJ PDFs (which are very similar to CTEQ5HJ) shows impressive agreement.

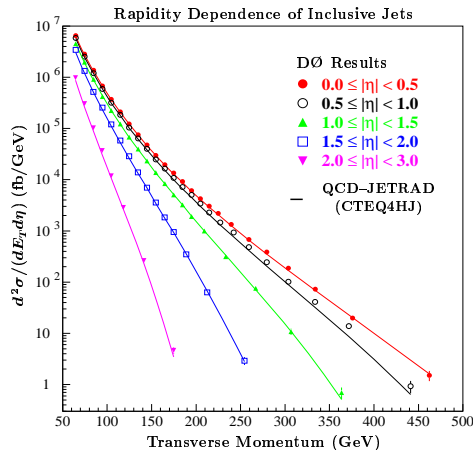


Figure 29: Double differential inclusive jet cross-section from the D0 experiment in five η bins, plotted against p_T . The curves are NLO QCD calculations based on the CTEQ4HJ distributions.

In addition to one-jet inclusive cross section, PQCD can make predictions on jet shapes, and multi-jet cross sections. Much progress has been made in this direction with extensive experimental measurements (at e^+e^- , ep , and $p\bar{p}$ colliders) and ever-higher order perturbative calculations.^{29,30,31}

Due to the increasing demands on precision and efficiency for jet studies in current and future collider programs, a great deal of effort has been devoted to improved jet algorithms. Many of the relevant issues and proposed solutions can be found in Refs. [28-31].

5.6 Heavy quark production

Heavy flavor production is of considerable interest both theoretically and experimentally. The total cross sections for producing charm and bottom particles in e^+e^- colliders provide important tests of the standard model. One heavy flavor particle inclusive distributions in the same experiments allow the determination of heavy flavor particle fragmentation functions, as described in Sec. 4.1. These are needed in interpreting the results of heavy flavor production in lepton-hadron and hadron-hadron collisions.

Current understanding of heavy flavor production is still not complete. We first discuss the theoretical issues, then the phenomenological ones.

Why is heavy quark production a non-trivial problem in PQCD?

Conventional PQCD was developed for hard processes depending on one hard scale, say Q .¹¹ Heavy quark production presents a challenge in PQCD because the heavy quark mass, m_H ($H = c, b, t$), provides an additional hard scale which complicates the situation. It requires *different ways to organize the perturbative series* – according to the relative magnitudes of m_H and Q .

Conventional Approaches

To see the basic physics ideas, let us focus on the simpler case of production of charm ($H = c$) in deep inelastic scattering in a world with three light flavors of quarks. All considerations apply to a generic heavy quark, and to hadro-production processes. Consider the PQCD calculation of the $F_2(x, Q)$ structure function which receives substantial contribution from charm production (about 25% at small x , as measured at HERA). The two standard methods for PQCD calculation of heavy quark processes represent two diametrically opposite ways of reducing the two-scale problem to an effective (hence approximate) one-scale problem.

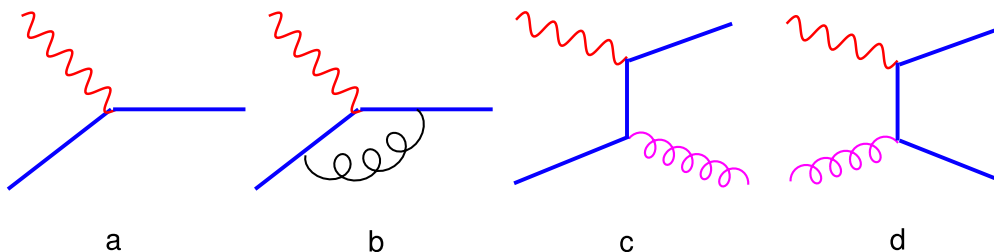
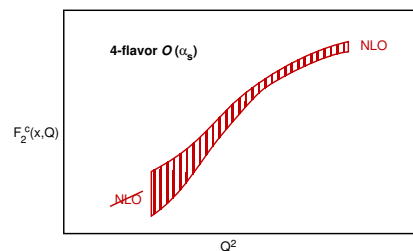


Figure 30: Partonic processes for charm production to NLO in the 4-flavor scheme.

Four-flavor Zero-mass Scheme: In the conventional *parton model approach* used in many global QCD analyses of parton distributions (e.g. MRS, CTEQ) and Monte Carlo programs (e.g. ISAJET, PYTHIA, HERWIG), the zero-mass parton approximation is applied to a heavy quark calculation as soon as the typical energy scale of the physical process Q is above the mass threshold m_c . This leaves Q as the only apparent hard scale in the problem. The LO and NLO production mechanisms for charm are given by Fig. 30, where the solid lines represent the charm quark. Note that the NLO diagrams are of order α_s , just as for the familiar case of total inclusive DIS structure functions. This is the most natural calculational scheme to adopt at high energies when $Q \gg m_c$. However, as we go down the energy scale toward the charm production threshold region, it becomes unreliable because the approximation $m_c = 0$ deteriorates as $Q \rightarrow m_c$. This point is illustrated qualitatively in the accompanying figure as an uncertainty band marked by vertical hashes which is narrow at large Q but is expected to widen as $Q \rightarrow m_c$.



Three (Fixed) Flavor Scheme: In the *heavy quark approach* which played a dominant role in “NLO calculations” of the production of heavy quarks,³² the quark is always treated as a “heavy” particle and never as a parton. The mass parameter m_c is explicitly kept along with Q as if they are of the same order, *irrespective of their real relative magnitudes*. This is usually referred to as the fixed flavor-number (FFN) scheme. The LO and NLO partonic processes in this scheme

¹¹We use Q as the generic name for a typical kinematic physical scale. It could be Q , W , or p_T , depending on the process.

are exemplified by the type of diagrams shown in Fig. 31. In this case, the NLO diagrams are

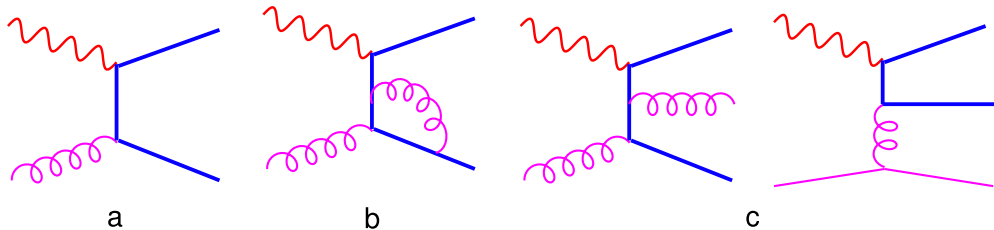
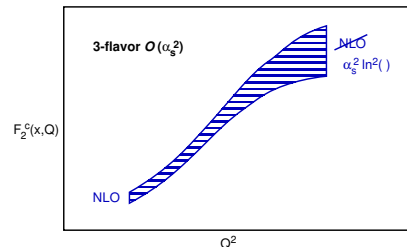


Figure 31: Partonic processes for charm production to NLO in the 3-flavor scheme.

of order α_s^2 , which are much more complicated to calculate! Near the threshold $Q \sim m_c$, it is natural to consider the charm quark as a heavy particle, hence the NLO calculation in this scheme is reliable. However, as Q becomes large compared to m_c , the FFN approach becomes unreliable since the perturbative expansion contains terms of the form $\alpha_s^n \log^n(m_c^2/Q^2)$ at any order n , which ruin the convergence of the series—these terms are *not infrared safe* as $m_c \rightarrow 0$ or $Q \rightarrow \infty$. This is precisely the situation discussed in Sec. 4.3 where we described how such large logarithms must be resummed to all orders in order to bring the perturbation series under control. Thus the uncertainty of the 3-flavor calculation grows as Q/m_c becomes large – it is no longer NLO in accuracy, in spite of the hard order α_s^2 calculation! This is illustrated in the accompanying figure as an uncertainty band marked by horizontal hashes which is narrow near threshold but is expected to widen as Q/m_c increases.



Generalization of the zero-mass QCD parton formalism

It should be obvious from the two figures illustrating the behavior of the 3- and 4-flavor schemes that: (i) these two conventional approaches are individually unsatisfactory over the full energy range, but are mutually complementary; and (ii) the most reliable PQCD prediction for the physical $F_2(x, Q)$ overall, can be obtained by combining the two, utilizing the most appropriate scheme at that energy scale Q , resulting in a composite scheme, as represented by the cross-hatched region in Fig. 32a, which is simply a composite of the two figures of the previous subsection. The use of a composite scheme consisting of different numbers of flavors in different energy ranges, rather than a fixed number of flavors, is familiar in the conventional zero-mass parton picture. The new formalism espoused in Refs. 17 provides a quantum field theoretical basis¹⁸ for this intuitive picture in the presence of non-zero quark mass. The 4-flavor scheme component of the general formalism *includes the full charm quark effects after the infrared unsafe part has been resummed*. It represents a substantial improvement over the conventional 4-flavor formalism in the region where $\log^2(Q/m_c)$ is not very large, which includes a substantial fraction of the current experimental range. This general approach has now been adopted, in different guises, by most recent papers on heavy quark production in PQCD.^{33,34}

The intuitively “obvious” general formalism is also technically precise: the order-by-order rules of calculation can be stated succinctly,³⁵ and the validity of the factorization theorem which underlies it can be established to all orders of perturbation theory.¹⁸ The essential ingredients of this formalism are:

- 3-flavor scheme at physical scales $Q \sim m_c$ and extending up;

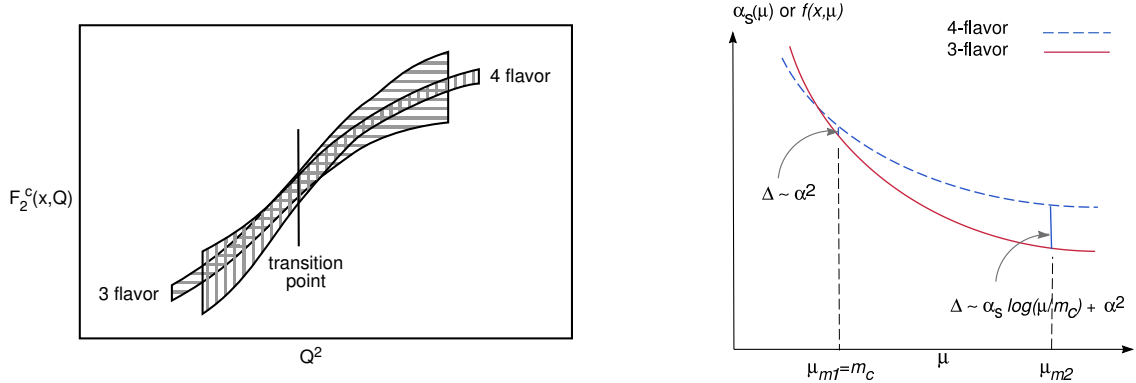


Figure 32: (a) Intuitive picture of the general formalism (a composite scheme); (b) Matching between the 3-flavor and 4-flavor calculations in the general formalism; the matching point can, in principle be chosen anywhere provided $\log(m_c/\mu)$ is not large.

- 4-flavor $m_c \neq 0$ scheme at asymptotic $Q \gg m_c$ and extending down;
- a set of matching conditions which relate the corresponding field-theoretic quantities, such as $\alpha_s(\mu)$ and the parton distribution functions $f_A^a(s, \mu)$, of the two schemes at some scale μ_m (the discontinuities are finite and calculable);
- a suitably chosen transition scale μ_t at which one switches from one scheme to the other in order to achieve efficiency and accuracy (as discussed above) when one makes physics predictions.

There is considerable inherent flexibility in the choice of μ_m and μ_t , which partially accounts for the apparent differences in recent papers on this subject. Some of the subtleties associated with choosing the matching point can be gleaned from Fig. 32b, where we show the matching between the 2 component schemes for the function $\alpha_s(\mu)$. At LO, the 3- and 4-flavor $\alpha_s(\mu)$'s are known to match without discontinuity at $\mu = m_c$ (as also are the PDFs). Thus, for the choice $\mu_m = m_c$, the discontinuity is of higher order; but for a different choice of matching point, such as μ_{m2} , the (calculable) discontinuity will be $\Delta\alpha_s \sim \alpha_s \log(\mu/m_c) + \alpha_s^2$. For more detailed discussion, see Refs. [35,18].

We conclude from this discussion that:

- The natural theory of heavy quark production (using charm as a specific example), valid at all energy scales, must combine 3-flv and 4-flv schemes ($m_c \neq 0$); this can be done in a seamless way. The same can be done across the b-quark threshold when one makes the transition from the 4-flv scheme to the 5-flv scheme. The general framework will then be a composite scheme consisting of three (3-, 4- and 5-flv) schemes.
- Simplistic labels “LO” & “NLO” can be misleading: the power of α_s (# of loops) alone does not determine the accuracy of the calculation in a multi-scale problem, due to the presence of potentially large logarithms, e.g. $\ln(Q^2/m_c^2)$, and other physical considerations. True LO & NLO results depend on the scheme and on the kinematic range of the process. In particular, for charm production, both order α_s 4-flavor calculation and order α_s^2 3-flavor calculation are in principle NLO in their respective scheme. The effectiveness of these “NLO” calculations, however, depends on the relative magnitude of the physical variable Q with respect to m_c , as explicitly illustrated in figures shown in the “conventional approach” subsection, under 3-flavor and 4-flavor schemes.

Lepto-production of charm and hadro-production of bottom

The status of the phenomenology of heavy quark production in lepton-hadron and hadron-hadron scattering are somewhat different. We briefly summarize each.

Lepto-production of charm

Measurement of charm production in DIS has come of age with the advent of the HERA experiments because of their reach into the small x region. In this region, where gluons dominate, one expects the ratios of final states containing various quark flavors to be simply proportional to the squares of the charges. The measured fraction of events containing charm at small x at HERA – around 25% – is quite consistent with this simple parton model expectation. Quantitatively, one can measure the one-particle inclusive cross section for a given charm meson (say D^*) at some 3-momentum \mathbf{p} ; or attempt to obtain an inclusive structure function for producing charm, say F_2^c , by summing over all final states which contain at least one charm particle.

To compare the experimental measurements with theory, one encounters somewhat of a dilemma. Experimentally, the one-charm-meson inclusive measurement is the more direct of the two. But the theoretical calculation of this cross section involves a lot of uncertainty associated with the fragmentation functions of the partons into the heavy meson. On the other hand, the inclusive structure function may appear to be simpler theoretically;¹² but its experimental determination requires both extrapolation outside the measured region and estimates of unmeasured channels.

Given these caveats, let us consider the inclusive case first. Previous comparison between the NLO 3-flavor calculation³⁶ (which is supposed to be good near threshold but questionable at high energies) with the recent Zeus data³⁷ showed good agreement (with the qualification that the experimental extrapolation actually makes use of the same theory, hence there is some circularity involved in this comparison). This indicates that, in spite of the cautionary notes about the theoretical shortcomings of the fixed-flavor scheme at high energies, the range of accuracy of the 3-flavor calculation may be enough to cover the available experimental region.

Recently, the same data have been compared with the complementary NLO 4-flavor calculation³⁵ (which is expected to be good at high energies, but becoming questionable near threshold). The agreement turns out to be just as good over the entire measured range. This is shown in Fig. 33a. For detailed discussions on choice of scale and other relevant issues, cf. Ref. 35.

Thus, we have the remarkable situation that both the simple (order α_s) NLO 4-flavor calculation and the more elaborate NLO 3-flavor (order α_s^2) calculations are robust in the currently available experimental energy range. Within the general framework described in the previous subsection, this means the overlap region between the two schemes is extensive: both descriptions are valid, hence there is no real need to make a transition from one to the other in current phenomenology. From the practical viewpoint, the (order α_s) NLO 4-flavor scheme does have the advantage of being computationally much simpler.

As mentioned earlier, the experimental results are on firmer ground for the differential distributions of the produced charm meson; but the theory is less reliable because: (i) uncertainties on the fragmentation function are large; and (ii) as is quite well-known for other processes, the NLO calculation for the inclusive cross sections becomes effectively LO for differential distributions (loops are opened up)! For the latter reason, the order α_s 4-flavor calculation becomes less reliable than the α_s^2 3-flavor calculation because the resummation of logarithm terms into the charm parton

¹²Actually, the theoretical definition of F_2^c itself is subject to some subtlety on the question of IRS, which we shall not go into here, cf. Refs. [35,34].

distribution function involves simplification of the kinematics of almost collinear charm partons in the final state. In order to obtain accurate predictions for the differential distributions, one needs to carry out the 4-flavor calculation also to order α_s^2 .

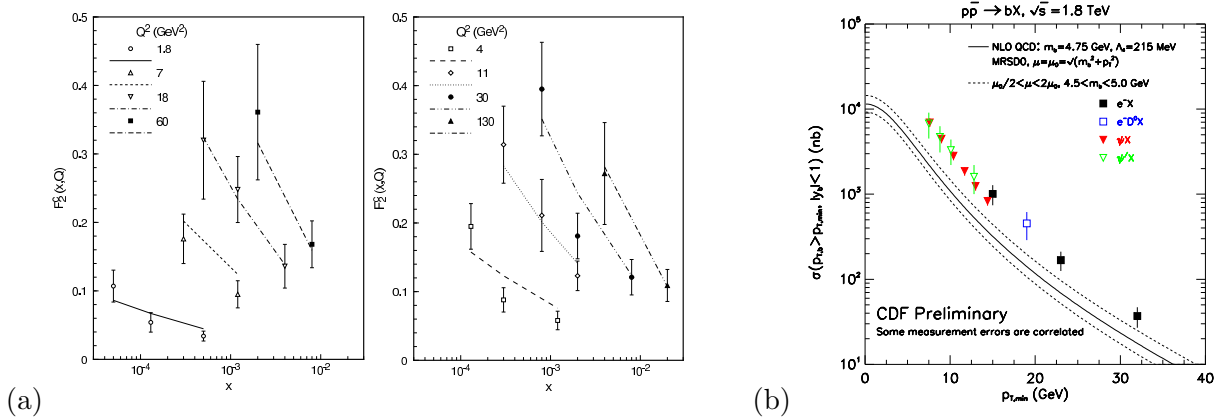


Figure 33: (a) Comparison of 4-flavor calculation with ZEUS DIS charm production data; (b) Comparison of 4-flavor calculation with CDF inclusive hadron-production of b .

Hadro-production (of bottom, mostly)

Heavy quark production in hadron-hadron collisions, from fixed-target to collider experiments, has been extensively reviewed.³⁸ Most of the theoretical calculations have been carried out in the fixed-flavor-number (FFN) scheme. Overall, the phenomenological status is not as satisfactory as in the case of lepto-production.

The simplest case is top production in hadron colliders. The top quark mass is so large that there is no doubt about what scheme to use in the theoretical calculation: 5-flavor QCD partons. The NLO calculation has been supplemented by threshold resummation corrections (which are not large). The phenomenology is quite satisfactory.

The situation with charm and bottom production is rather different. Even from the purely theoretical viewpoint, the reliability of the FFN scheme is questionable because of two related facts, known since the first NLO calculations were completed: (i) the NLO term is of the same numerical size as the LO term (with no obvious understanding of why); and (ii) the scale dependence of the NLO result is as strong as the LO one (in sharp contrast to the well-behaved cases of DIS and DY processes). Phenomenologically, this results in a large range of uncertainty in the predicted cross section, both for charm and bottom production. The measurement of the charm cross section in hadron-hadron scattering is very challenging; the phenomenological status is not clear. Cf. Ref. 38. The measurement of b production at the Tevatron collider is more revealing. Figure 33b shows the comparison of data from the CDF experiment with the NLO 4-flavor calculation. We see that the theory curves lie about a factor of two above the experimental measurements, even allowing for the wide band of theoretical uncertainties.

One possible way to improve the fixed 4-flavor calculation is to use the 5-flavor scheme, taking into account the b -parton, since the mass m_b parameter is small compared to the typical energy scale for the Tevatron experiments. Two recent studies found that this approach does not substantially improve the agreement between theory and experiment.³⁹ Another possibility is that large $\log(1/x) \sim \log(q_T/m_b)$ terms could substantially increase the theoretical prediction if they are resummed.⁴⁰ The problem remains open at present, and, along with direct photon production, it

represents an important challenge to PQCD theory.

6 Global QCD Analysis and Parton Distributions

With the factorization theorem as its foundation, the QCD parton model provides us with the framework to interpret experimental results from all hard processes involving hadrons, and to make a wide range of predictions on SM and new physics processes. Applications to the individual processes were examined in the last section. This section concerns the global analysis of hard scattering data in order to

- (i) test the validity of the PQCD formalism;
- (ii) determine the fundamental parameters of the theory – the coupling $\alpha_s(\mu)$, and the quark masses $m_i(\mu)$;
- (iii) extract the non-perturbative PDFs and FFs from experiments which involve hadronic initial and/or final states.

The emphasis will be on parton distributions of the nucleon, both because of their paramount importance and because, by far, the most progress has been made on this front. All the issues we discuss are in fact general, so they apply to the other cases too.

As already mentioned in Sec. 4.6, the determination of PDFs in a global analysis is conceptually simple: on the RHS of Eq. (54), one inputs a set of suitable experimental data, along with the perturbatively calculated hard cross sections to some order in α_s , then one obtains (on the LHS) the PDFs of interest – provided, of course, the set of inputs is “complete” and mutually consistent.

In practice, the task is far from being straightforward because of a large number of theoretical, experimental, and phenomenological complications. We first summarize the various inputs to current global analyses, and discuss the potential complications, in order to put the subsequent review of recent results and future prospects in the proper perspective.

6.1 Common inputs and relevant issues

Experimental input

In principle, we would like to include as many experimental data sets as possible in the global analysis. To give an idea of the wide range of potential experiments available for global QCD analysis, we list the physical processes and relevant experiments by their common names without elaboration:

- DIS – Neutral Current (e, μ on p,d)
SLAC, BCDMS, NMC, E665, H1, ZEUS
- DIS – Charged Current ($\nu, \bar{\nu}$ on nucleus)
CDHSW, CCFR, CHARM, CHORUS
- Drell-Yan – continuum (lepton-pair)
E605, NA51, E866
- Drell-Yan – W and Z
CDF, D0
- Direct Photon Production
WA70, UA6, E706, ISR, UA2, CDF, D0
- Inclusive Jet Production
CDF, D0
- Lepto-production of Heavy Quark (c)
H1, ZEUS

· Hadro-production of Heavy Quark (b)

CDF, D0

The DIS experiments are high statistics, high precision, mature experiments. They typically consisting of many hundreds of data points with statistical and systematic errors at the order of only a few percent. By comparison, direct photon, jet and heavy quark production experiments have much fewer data points with considerably lower statistics, and often with large systematic errors. The complexity of individual data sets as well as the diversity of the collective data sets pose a great deal of challenge for global analysis. Some specific issues are:

- Because of the complexity of modern experiments, the errors on most experimental data sets are only approximate; e.g. many sources of systematic error are often combined into a single effective uncorrelated error for each data point. Even when more detailed information on systematic errors are available, they may not behave as expected for ideal experiments in textbook statistics (e.g. in a high statistics experiment, the χ^2 per data point may deviate significantly from unity even for the best of fits, rendering the data set nominally very improbable in a strict statistical interpretation). These facts make the application of standard statistical tools difficult.
- When different experimental data sets on the same, or similar, physical processes are included in the global analysis, they may or may not be consistent by standard statistical tests, even if individual ones appear to be self-consistent. In practice, it is not uncommon to find high precision experiments being “inconsistent” with each other according to strict statistical rules.
- When some data sets consist of many hundreds of data points, while others only a few points (or even a single point, as NA51 in the above list does), how should these data sets be relatively weighed in a global analysis, particularly if the latter is found to carry negligible statistical weight in a naive combined analysis, but is known to provide some crucial physical constraints to PDFs?¹³
- Some important experiments (such as neutrino DIS) are performed on nuclear, rather than nucleon, targets. Although the assumption of incoherent scattering off individual nucleons inside the nucleus is a good first approximation, it has been known experimentally that nuclear shadowing and anti-shadowing (the EMC effect) can significantly affect the quantitative analysis. Heavy nuclear target correction factors have been measured for incident charged leptons; but not for neutrinos. Deuteron target corrections, needed for extracting neutron structure functions, are certainly not available. Theoretical calculations on nuclear correction factors are model-dependent, hence often controversial.

Theory input

The main theoretical input to the global analysis is the perturbatively calculated hard cross sections, along with the QCD evolution equations which control the scale dependence of the PDFs. The hard cross sections and the evolution kernel must be calculated to the same order in PQCD, in order to obtain consistent results from the factorization formula – e.g. as pointed out in Sec. 4.5, the uncertainty due to the choice of scale is formally of higher order only if this condition is met.

Sources of possible large corrections to the standard QCD parton model formula can come from:

1. Higher-order contributions in α_s which happen to be large, such as in direct photon production at fixed target energies and b quark production at hadron colliders;
2. Significant corrections due to (p_T , small- x , threshold) resummation of logarithms arising from multi-scale problems which occur near boundaries of the kinematic space;
3. Power-law corrections (higher-twists, renormalons, target-mass corrections ... etc.);

¹³This would not be a problem if all input experimental data sets, including errors, are perfect. But in reality they are not.

4. Nuclear correction, if applicable, as mentioned above.

In practice, as described in our survey of hard processes in the last section, the reliability of the PQCD calculation varies widely from process to process. How can the theoretical uncertainties in PQCD be assessed and included in the analysis? This is a difficult question to answer. The varied behavior in different processes necessitates a flexible approach on a case by case basis.

Parametrization of non-perturbative PDFs

To proceed with a global QCD analysis, one needs to provide a set of initial PDFs at some scale $\mu = Q_0$. This is done usually in terms of a set of functions, say $f_p^a(x, Q_0)$, with adjustable parameters which are eventually optimized to fit the global data. In principle, since these functions represent our ignorance of the non-perturbative nucleon structure at the confinement scale, there should be complete freedom in choosing their parametric form. In practice, we do have some handle on their behavior, and the most commonly used form is

$$f(x, Q_0) = A_0 x^{A_1} (1-x)^{A_2} P(x) \quad (65)$$

where the parton flavor label “ a ”, as well as the hadron label, on f , $P(x)$, and the coefficients $\{A_i\}$ have been suppressed; and $P(x)$ is assumed to be a smooth function.

- The factor x^{A_1} is motivated by physics considerations in the small x limit (high energy for fixed Q^2) where the power A_1 has a Regge interpretation.
- The factor $(1-x)^{A_2}$ is motivated by physics considerations in the $x \rightarrow 1$ limit (resonance region, when $Q \sim Q_0$), where the power A_2 can be related to valence quark wave functions and counting rules.
- The factor $P(x)$ is purely phenomenological, in order to accommodate any smooth behavior required to represent adequately the unknown non-perturbative PDFs. The form varies in the literature — examples include $(1 + A_3\sqrt{x} + A_4x)$ (MRS), $(1 + A_3x^{A_4})$ (CTEQ), ... etc.

In a systematic global analysis, there are two concrete issues concerning this parametrization which need to be addressed.

1. How much flexibility should be built into $P^a(x)$ – how many independent parameters $\{A_i^a\}$ are needed? The number cannot be too small, so that there is not enough flexibility to accommodate observed experimental phenomena.¹⁴ On the other hand, the number cannot be too large, so that there is too much freedom, beyond that which can be meaningfully constrained by existing data.¹⁵
2. How do we determine the dependence of the results of the global analysis on the choice of the parametric form; and how do we quantify the uncertainties of PDFs due to this choice? Any specific choice of the parametrization form will introduce *some* artificial correlations in the behavior of the PDFs in different x ranges – e.g. the factor x^{A_1} will influence the behavior of the PDF over the entire x range, even if the value of A_1 is primarily determined by data at small x , and likewise for the other factors. The question is *how much*? The polynomial form for the initial distribution functions can also introduce artificial nodes in the PDF.

To avoid some of these problems, a radical approach would be to abandon using parametrized functional forms completely, and treat the input functions as sets of independent points (as in the mathematical definition of a “function”). This strategy clearly suffers from the problem of having too many degrees of freedom, as mentioned above. Attempts to reduce the number of degrees of

¹⁴Historically, this situation happened when initial PDFs were assumed to have SU(2) or SU(3) flavor symmetry. New experimental data then required the expansion of the number of parameters to allow for flavor symmetry violation.

¹⁵Artificial and unphysical structures in the PDFs can result from such a situation.

freedom (e.g. by imposing smoothness) will probably bring back the same problems this strategy is meant to cure!

6.2 Global analysis strategies and procedures

In the face of such a collection of tough (and sometimes subtle) experimental, theoretical, and phenomenological problems summarized above, conventional global QCD analyses have to adopt corresponding practical strategies based on physical intuition, experience, and common sense, rather than strict statistical prescriptions. We mention some of the common strategies and choices adopted in the latest works, such as those of the widely used MRS and CTEQ efforts.

Theory: Practically all current global QCD analysis work is still based on NLO QCD. Although some NNLO hard cross sections are available, the corresponding evolution kernel is not. Besides, the size of the NNLO correction in those cases where they are available, tends to be small (compared to, say current experimental errors); hence the practical need for their inclusion is unclear. The place where NNLO corrections seem to become noticeable is usually near the boundaries of the phase space (e.g. at small x), but these are multi-scale regions where the more relevant approach would be to incorporate the appropriate resummation instead.

Within NLO QCD, an issue which has attracted some attention in recent years is the choice of scheme in relation to the treatment of the heavy quarks c and b . This problem was discussed in some detail in Sec. 5.6. Historically, the zero-mass parton formalism was usually adopted, superimposed with incrementing the number of effective quark flavors by one each time a heavy quark threshold is crossed. This is relatively simple, and practical – since the hard cross section calculation for most processes has only been done in this scheme. As mentioned in Sec. 5.6, however, recent measurements of sizable contributions of charm production in DIS has prompted many groups to adopt variants of the more general formalism of Collins *et al.*, which combines the various schemes with different number of flavors while keeping relevant quark mass effects. The MRST²³ distributions employ such a new scheme. The use of these distributions with hard cross sections calculated in the conventional scheme is somewhat questionable. For the sake of maintaining consistency, the CTEQ distributions⁴¹ offer two alternatives, one in the conventional zero-mass scheme and one in the non-zero mass scheme.

Experimental input: In spite of the wide range of experiments available, the selection of which data sets to use in a global QCD analysis is non-trivial, because of the complex experimental and theoretical issues discussed earlier. We mention a few illustrative examples.

- Should direct photon production data be used at all; if so, which ones? The reasons for raising these questions are:

1. The theoretical uncertainty for this process is not under control, as discussed earlier; even though, phenomenologically, the historical idea of constraining the gluon distribution by direct photon production is extremely appealing. Without introducing k_T broadening, theoretical predictions are a factor of 3 smaller than the latest experiment; with k_T broadening, one can fit data, but the experiment hardly provides any constraint because the theory now depends sensitively on the amount of smearing introduced.

2. Independent of the theoretical dilemma, there appears to be an inconsistency between the two most prominent fixed-target experiments, WA70 and E706. For details, cf. Refs. [27,45].

In the face of these problems, the CTEQ5 analysis does not use direct photon data. MRST98²³ and MRST99⁴² used these data, and obtained very different gluon distributions, depending directly on the amount of k_T smearing assumed. In the more recent MRST2000 study,⁴³ the direct photon data were dropped.

- Should experimental errors be taken at their face value; if so, what should be done when strict statistical tests rule out individual experiments or some combination of experiments?

As already mentioned earlier, real experiments seldom produce perfectly behaved errors. Therefore, this question has to be faced in any global analysis effort. In a purist’s approach, one ends up with only one or two sets of data which are statistically compatible. The effort ceases to be a *global* analysis.

In practice, most groups take a more flexible interpretation of the errors; and include all relevant experiments which are not in “obvious conflict” with each other. This practice inevitably introduces subjective judgements. Table 2 lists the experiments included in the CTEQ5 analysis; it serves

Experiment	Process	# Data pts	Reference
BCDMS	DIS μp	168	CERN
BCDMS	DIS μd	156	CERN
H1	DIS ep	172	HERA
ZEUS	DIS ep	186	HERA
NMC	DIS μp	104	CERN
NMC	DIS $\mu p/\mu n$	123	CERN
CCFR	DIS $\nu p F_2$	87	FNAL
CCFR	DIS $\nu p F_3$	87	FNAL
E605	D-Y pp	119	FNAL
NA51	D-Y pd/pp	1	CERN
E866	D-Y pd/pp	11	FNAL
CDF	$W_{lep-asym.}$	11	FNAL
D0	$\bar{p}p \rightarrow jet X$	24	FNAL
CDF	$\bar{p}p \rightarrow jet X$	33	FNAL

Table 2: List of data sets used in the global analysis.

as an illustration of the scope of experimental input in a typical modern global QCD analysis of PDFs. The experimental data sets used by the MRS group are similar, but not identical (as the discussion of direct photon experiments already implies).

- In what range of kinematic variables (x, Q) should the global analysis be performed?

Although, in principle one would like to have as wide a range as possible, there are reasons to be judicious in restricting the range in practice. For instance, one should compare theory with experiment only where the theory is expected to be reliable. This rules out the low Q^2 region, where there are large amounts of data but where one does not expect the twist-two PQCD calculations to be good. Thus, one typically imposes kinematic cuts of $Q > 2$ GeV and $W > 4$ GeV in DIS. The latter is designed to steer away from the resonance region which does not properly belong to DIS. For inclusive jet production, because of problems of jet definitions (both experimental and theoretical), a cut as high as $p_T > 30 \sim 50$ GeV is required.

Figure 34 gives the kinematic map of the range of (x, Q) variables covered in a typical modern global analysis. We observe the many orders of magnitude probed by these analysis, with DIS data at HERA reaching into the very small x region, and the hadron collider data on jet production

extending to the highest Q (hence shortest distance in space-time) values.

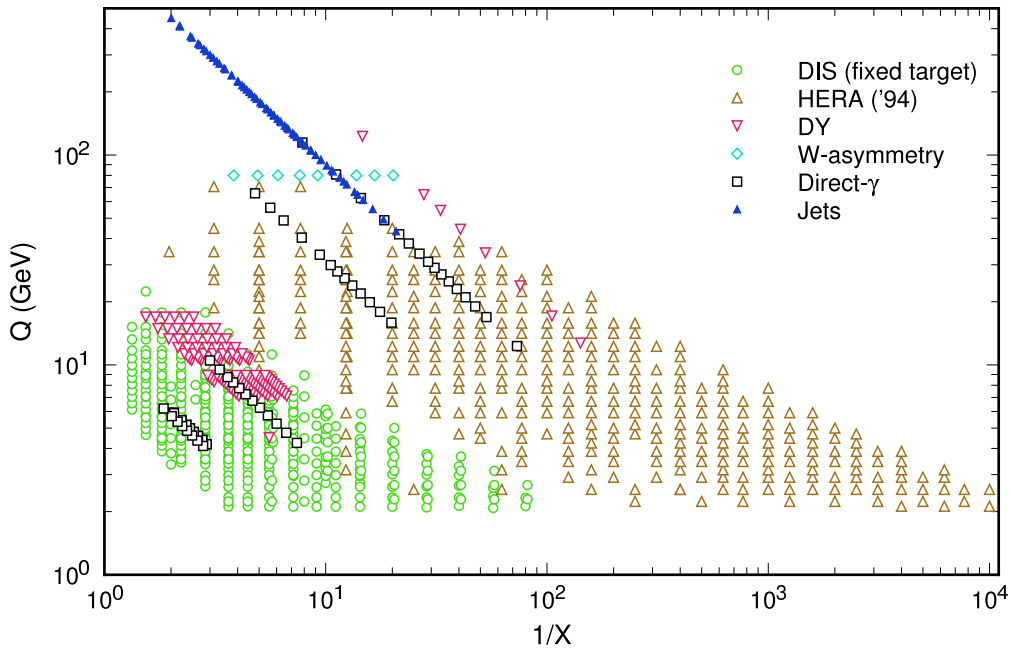


Figure 34: Kinematic map of the (x, Q) range covered by the data sets used in CTEQ global analysis. The complementary roles of the fixed-target, HERA, and Tevatron experiments are clearly seen.

Global fitting procedure Given that sensible choices of strategies and compromises need to be made on many issues in a realistic global analysis, the most practical way to determine the PDF parameters by comparing theory to a large number of diverse experiments is by the method of least χ^2 fits.

In the CTEQ analysis, one adopts the following *effective global χ^2 function* to represent known experimental inputs:

$$\begin{aligned}\chi_g^2 &= \sum_n \chi_n^2 \quad (n \text{ labels the experiments}), \\ \chi_n^2 &= \left(\frac{1-N_n}{\sigma_n^N}\right)^2 + \sum_I w_n \left(\frac{N_n D_{nI} - T_{nI}(a)}{\sigma_{nI}^D}\right)^2,\end{aligned}\tag{66}$$

For the n^{th} experiment, D_{nI} , σ_{nI}^D , and $T_{nI}(A)$ denote the data value, measurement uncertainty, and theoretical value (dependent on the theory parameters $\{A\}$) for the I^{th} data point; σ_n^N is the experimental normalization uncertainty; N_n is a relative normalization factor for that experiment in the global analysis; and w_n is a “prior” weighting factor based on physics considerations or on information derived from existing work. This χ_g^2 function provides an effective way of searching for global minimum solutions of the PDF parameters $\{A_i\}$, which incorporates all experimental constraints in a uniform manner while allowing some flexibility for physics input. It is particularly practical since most experiments used in the global analysis only publish an effective point-to-point (i.e. uncorrelated) systematic error along with the statistical errors.

By minimizing this χ_g^2 function with respect to $\{A_i\}$, one obtains candidate solutions to the PDFs at the scale $\mu = Q_0$. QCD evolution then allows the generation of the PDFs over the entire (x, Q) plane.

6.3 Review of recent parton distribution functions of the nucleon

Based on considerations summarized in the previous sections, and using strategies similar to that described above, the global QCD analysis of parton distributions has made steady progress in the last twenty years, keeping pace with advances in QCD calculations as well as ever more extensive and accurate experimental measurements. The most widely used MRS²³ and CTEQ⁴¹ parton distribution sets represent independent work, using comparable theoretical and experimental inputs but different strategies and procedures.¹⁶

It is important to point out that the published PDF sets are, at best, *representative or candidate PDFs*. They are not unique or “best” sets, even for a given set of inputs – because of the complications discussed above, and the subjective choices which affect their determination and selection (for circulation purposes). The uncertainties of these PDFs will be discussed in the next section.

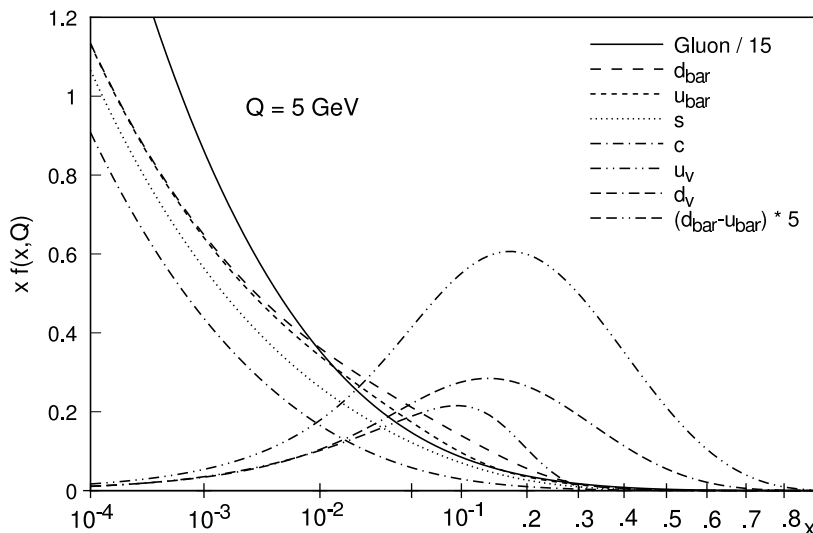


Figure 35: Overview of the parton distribution functions of the proton at a scale of 5 GeV, as represented by the CTEQ5M PDF set.

Representative results Figure 35 shows an overview of the parton distribution functions of the proton at a scale of $\mu = 5$ GeV, as represented by the CTEQ5M PDF set. The gluon distribution is scaled down by a factor of 1/15, while the flavor SU(2) breaking combination $\bar{d} - \bar{u}$ is scaled up by a factor of 5, in order to make the respective functional dependence discernible in the plot. For the same purpose, the small- and large- x behavior of these functions have been made more apparent by adopting a horizontal scale which is $\log(1/x)$ -like at small x and x -like at large x respectively.

Flavor dependence We can see that the gluon distribution is, by far, the dominant parton at small x ; while the valence d and u quarks are the dominant ones at large x . The sea quark distributions are definitely neither flavor SU(3) nor SU(2) symmetric, as naively expected in the early days of the QCD parton model phenomenology. The strange quark distribution is about 50% that

¹⁶On the other hand, the GRV series⁴⁴ of PDFs is based on a rather different approach: (i) it emphasizes “radiatively generated partons,” especially at small x , by starting the QCD evolution from a very low energy scale, say 300-500 MeV; (ii) it uses the 3-flavor fixed flavor number scheme, hence does not include the heavy quark partons; and (iii) phenomenologically, the fit to data other than DIS is not as comprehensive as the other two.

of the average $(\bar{d} + \bar{u})/2$ as the result of an input assumption, based on some experimental evidence. (Cf. more discussions in the next section on uncertainties.) The SU(2) breaking combination $\bar{d} - \bar{u}$, which is relatively well-established by now, has a distinct structure as shown.

Q dependence The shape of the PDFs depends sensitively on the scale at which the nucleon is probed, especially in the relatively low energy region. Fig. 36 shows the Q -evolution of the gluon distribution from 2 GeV to 80 GeV. (The function has been scaled vertically by the factor shown in order to exhibit its behavior at large and small x .) As can be seen, the softening of the x dependence over this range of Q is very substantial.

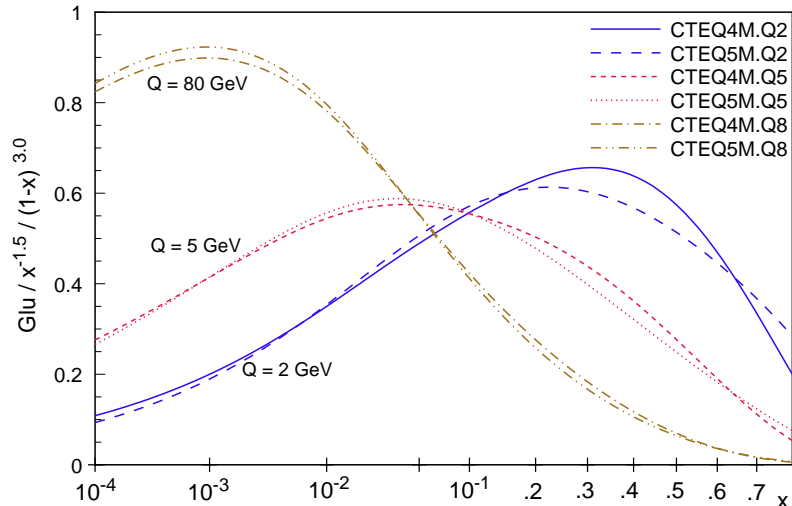


Figure 36: The changing shape of the gluon distribution from $Q = 2$ GeV to 80 GeV, as the result of QCD evolution.

Comparison of representative PDF sets The quark distributions are generally well determined by the extensive precision DIS data, within some uncertainties about the flavor dependence to be discussed in the next section. On the other hand, because the gluon does not couple directly to the electroweak gauge bosons (which are used to probe the parton structure in lepton-hadron processes), there is still a fair range of flexibility for the behavior of the function $G(x, Q)$ ($f^g(x, Q)$ in earlier notation). This range is highlighted in Fig. 37 which consists of a comparison of some CTEQ5 and MRST98 gluon distributions. The interpretation of these results also serves to illustrate (or make concrete) some common issues discussed earlier concerning global QCD analysis.

- The large range of variation between the MRST sets (labeled MRS98-n in the graph) in the region around $x \sim 0.3$ reflects the freedom of choice of the k_T -broadening parameter $\langle k_T \rangle$ which produces a very significant correction factor to the theoretical cross section (recall this factor needs to be of the order of $2 \sim 3$ for E706 to agree with data), in addition to the well-known large scale dependence for NLO QCD predictions.^{26,45} The narrower apparent range seen between the two CTEQ5 sets in this x span is due to the constraints on the shape of $G(x, Q)$ imposed by the inclusive jet cross section (which has rather stable NLO QCD theory predictions). The MRST-G \uparrow set (MRS98-2 in the figure) uses no k_T broadening; thus, its $G(x, Q)$ is closest to that of CTEQ5M.¹⁷

¹⁷The same is true for the new MRST gluons,⁴³ since direct photon data are no longer used.

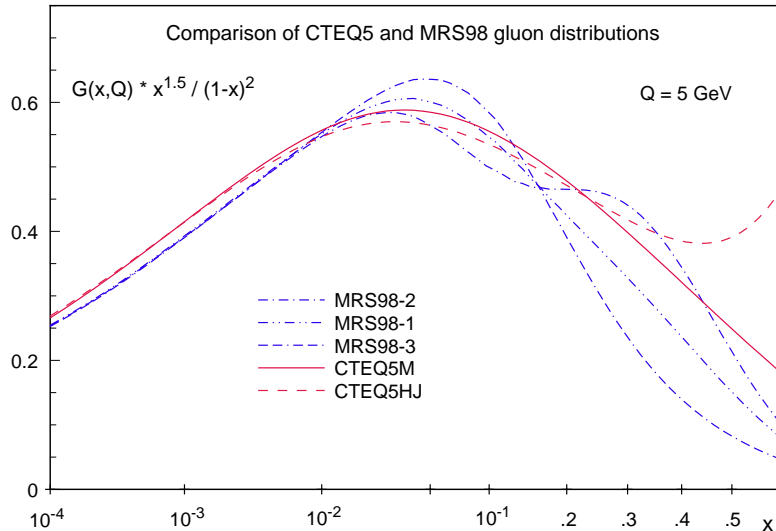


Figure 37: Comparison of some CTEQ5 and MRST98 gluon distributions. The results are explained in the text.

- For the $x > 0.5$ region, the wide range of variation of the CTEQ5 sets reflects the lack of experimental constraints on $G(x, Q)$ at large x . The relative “rise” of the CTEQ5HJ gluon at large x is the consequence of requiring the fit to agree with the highest p_T inclusive jet data points. On the other hand, the convergence of the MRST gluons in this region appears to be due to choosing the same parametrization at large x for all these sets.
- The differences between the two series in the range $0.01 < x < 0.1$ are most likely the indirect consequence of the differences in the large x range, $0.1 < x < 0.6$, due to the momentum sum rule constraint. Finally, the “node” exhibited by the MRST distributions near $x = 0.15$ is probably an example of artifacts which result from a specific choice of functional form, coupled with the sum rule requirement, as discussed earlier.

One of the phenomenological consequences of these differences can be seen in Fig. 38, where the CDF data on inclusive jet production are compared to calculations based on the CTEQ5 and MRST98 distributions.

The moral of this comparison: results from global analyses must be understood in the context of the relevant inputs; they can be significantly driven by subjective choices built into the analysis. Here we have seen several dramatic effects due to the use of, or emphasis on, data (direct photon, high p_T jet); theoretical assumption (k_T broadening); and choice of functional form for the initial distributions.

6.4 Uncertainties of PDFs and their predictions

Parton distribution functions are used in all calculations of cross sections for high energy interactions involving hadrons. Although much progress has been achieved in narrowing down the PDFs in several generations of global QCD analysis, it is important to know the uncertainties of the PDFs and, more importantly, their physics predictions, in order to meet the increasing demands of precision standard model studies and new particle search predictions. Figure 39 shows the results of a recent study of “errors” on the PDFs, as the result of propagating experimental errors from a collection of DIS experiments. The LHS plot shows all the parton flavors; the RHS plot shows the percentage uncertainties for the gluon and the sum of all the quark flavors. Whereas these

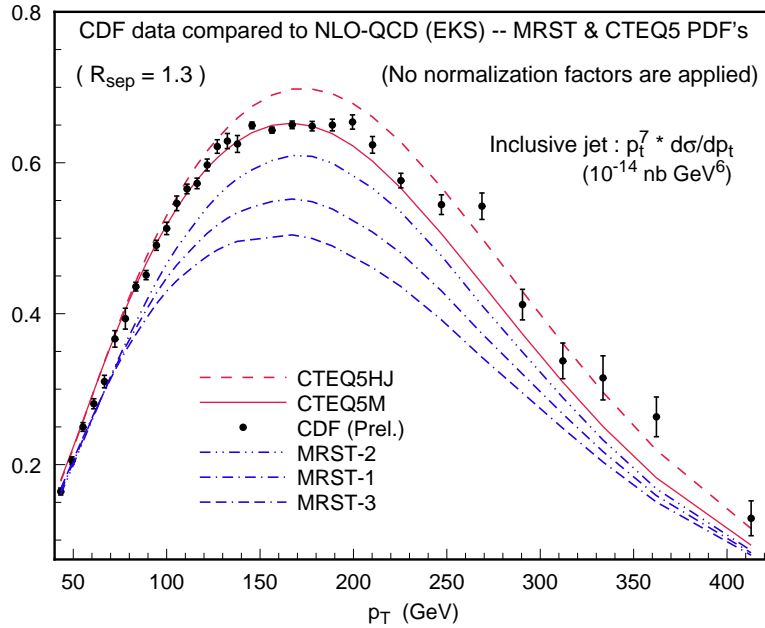


Figure 38: Comparison of the D0 inclusive jet production cross-section to NLO QCD calculations based on the PDFs of Fig. 37.

plots underline the existence of substantial uncertainties, they do exaggerate the errors because the various flavors of PDFs are highly correlated (which cannot be seen from these plots) – as one flavor goes up, the others will compensate by moving down as constrained by data and by sum rules.

We first survey what aspects of the nucleon PDFs are still uncertain, and then describe recent new efforts to quantify these uncertainties in a systematic manner.

What are current uncertainties on PDFs?

The Gluon Distribution

The gluon distribution contributes to all high energy processes. It is important for all SM, SUSY, and other new physics calculations. Yet, as already indicated in previous sections, it is among the least well determined of the parton distributions. The most relevant measurements for its determination are: $dF_2(x, Q)/d \ln Q$ in DIS; inclusive and differential jet production cross sections; direct photon production; and heavy quark production. Comprehensive analysis of the Q^2 dependence of the DIS structure functions, with the aim of determining $G(x, Q)$, has been carried out by the experimental groups, particularly BCDMS, NMC, H1, ZEUS and CCFR. Bands of uncertainties on $G(x, Q)$ have been obtained by all groups; the results shown in Fig. 39 are representative of such efforts. The inclusive jet production cross section which is directly sensitive to $G(x, Q)$ has been used by the CTEQ collaboration in their global analysis of PDFs. This is useful in the $0.05 < x < 0.3$ region, but there are still uncertainties for $x > 0.3$, as we have seen in Fig. 39.

In contrast, the “classic” process for gluon determination – direct photon production – has been beset with uncontrolled theoretical uncertainties as has already been described. In principle, heavy quark production cross sections at hadron colliders are also very sensitive to $G(x, Q)$. Unfortunately, the theoretical uncertainty in NLO QCD for this process also considerable, not to mention the

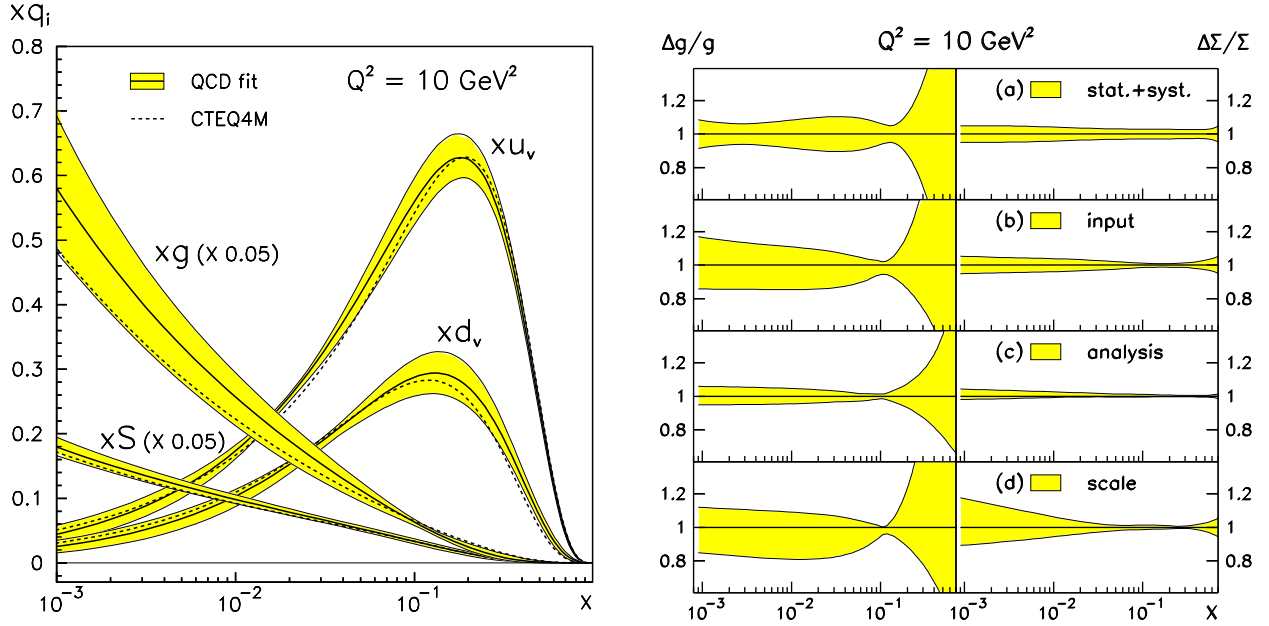


Figure 39: Uncertainty bands of PDFs obtained by M. Botje⁴⁶: (a) the valence quarks, the gluon and the sea quarks; (b) fractional uncertainties of the gluon distribution (left column) and the sum of all quark distributions (right column).

currently unresolved discrepancy between theory and experiment for b production, cf. Sec. 5.6. In the end, pinning down of the gluon distribution will take the combined constraints from many processes, and it will depend on much needed improvements in theory, as well as in expanded experimental input.

Strange Sea Size, Shape and Charge Symmetry

Two combinations of total inclusive DIS structure function measurements are sensitive to the strange quark distribution. At the naive parton level,

$$\Delta F_3^{CC} = F_3^{\nu N} - F_3^{\bar{\nu} N} \approx 4(s - c) \quad \text{and} \quad \frac{5}{6}F_2^{CC} - 3F_2^{NC} \approx (s - c).$$

In addition, a *direct* measurement of the inclusive structure function with tagged charm yields naively $F_2^{\text{charm}} \approx s$. These relations must be supplemented by “NLO” contributions from subprocesses involving a gluon initial state, such as $g + \gamma^*/w \rightarrow q/c$ to be well-defined in the QCD framework, cf. detailed discussions about LO/NLO interplay in Sec. 5.6.

Most current global analyses use as input the relation, $s(x) = 2\kappa * (\bar{u}(x) + \bar{d}(x))$ with $\kappa \simeq 0.5$, inferred from analysis of the charm production cross section, primarily from the CCFR experiment. There is no clear evidence that this result is consistent with the two combinations of total inclusive structure functions given above. In fact, there are recent re-analyses of the earlier CDHS and CHARM data which reached different conclusions.⁴⁷ The challenge here is to present the neutrino charm production data in the model-independent form of F_2^{charm} , so that they can be incorporated into the general global analysis. Then one can conclusively test the consistency of all available data, and determine the strange quark distribution independent of assumptions. Another open question is whether the commonly accepted assumption $s(x) = \bar{s}(x)$ is valid or not.⁴⁷ This too can be tested experimentally if all available data are incorporated in a comprehensive analysis.

Breaking of SU(2) flavor symmetry

For studying the breaking of SU(2) flavor symmetry – the u vs. d and \bar{u} vs. \bar{d} differences

– the relevant experiments are: DIS: $F_2^n - F_2^p$, F_2^n/F_2^p , F_2^{nc}/F_2^{cc} ; Drell-Yan charge asymmetry: $\sigma^{pd}/2\sigma^{pp}$; and lepton y -asymmetry in W -production and decay. The unresolved issues are: “correct” deuteron correction (relevant for $F^d \rightarrow F^n$ conversion); heavy nuclear target corrections (relevant for extracting $F_{2,3}^{\nu N}$ from $F_{2,3}^{\nu A}$); other power-law (e.g. target mass) corrections; small x : what is the origin of SU(2) flavor symmetry breaking of the sea?; large x : should the ratio $d(x)/u(x) \rightarrow 0$ as $x \rightarrow 1$?; and charge symmetry violation: is there any evidence for $u_p(x) \neq d_n(x)$? As an example, Fig. 40 shows the uncertainty on ratio $d(x)/u(x)$ based on analysis of current DIS data. There are

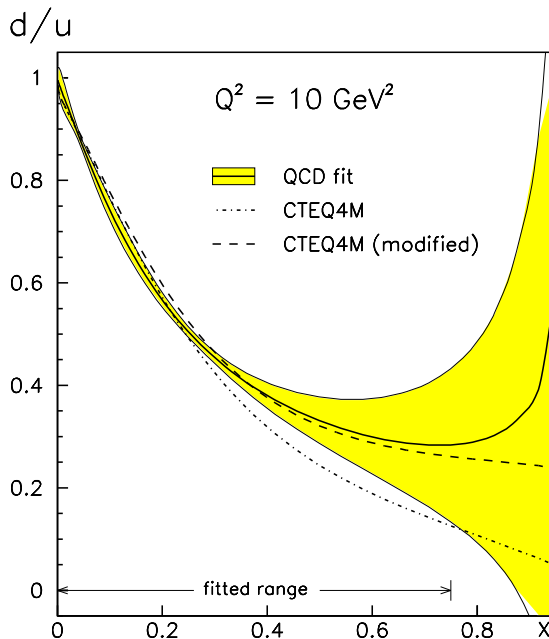


Figure 40: Uncertainties on the parton distribution ratio $d(x)/u(x)$ inferred from current errors on DIS experiments.⁴⁶

extensive discussions of these issues in the literature.^{48,49} There is currently no clear consensus on most of them.

The unambiguous way to clear up the situation is to avoid the uncertainties of nuclear corrections by focusing on nucleon targets as much as possible, e.g. use neutral and charged current events at HERA, utilizing both electron and positron beams.⁴⁹ (With progress along this line, we can learn nuclear physics from the measurements on nuclear targets, rather than invoking nuclear model calculations to extract PDFs.)

Heavy Quarks

An independent question concerns the heavy quark distributions $c(x, Q)$ and $b(x, Q)$. Are they purely “radiatively generated” by gluon splitting, or are there “intrinsic” charm and bottom partons inside the nucleon? In order to ask this question in a meaningful way, one needs the generalized PQCD framework discussed in Sec. 5.6. The phenomenological problem encountered in comparing theory with the b production cross section from the hadron collider, cf. Sec. 5.6, underlines the need to keep an open mind about heavy quark distributions – e.g. could the assumption of a small intrinsic b distribution inside the nucleon resolve the current dilemma? Comprehensive phenomenology on heavy quark production, in general, has yet to be carried out using the general formalism.

Quantifying uncertainties of PDFs and their physical predictions

The importance of quantifying the uncertainties of PDFs and their physical predictions for current and future HEP programs is self-evident. Given the complexity of the numerous issues discussed throughout this section, however, the real question is: how should this be done? We first briefly introduce an ideal approach, based on the assumption that perfect experimental inputs are available. Then we describe a less ambitious, but more practical, effort to make quantitative estimates of the uncertainties, given the state of experiments as we have them today.

The ideal approach

In an ideal world, the basic principles of global QCD analysis, including full error calculations, are very simple. As formulated by Ref. [50] in terms of Bayesian statistics, one proceeds as follows:

Inputs to global analysis:

1. A set of “priors”: theory model (NLO QCD, . . . etc.); and non-perturbative PDFs at some scale $\mu = Q_0$, specified by a set of parameters $\{A\}$ or some other means (say histograms);
2. Experiment: it is taken as axiomatic that each experiment is represented by an *experimental response function* $P_{\text{exp}}(\{x_t\}|\{x_e\})$ which specifies the probability density of measuring $\{x_e\}$ given the true nature value $\{x_t\}$. If this function is not directly supplied, then it must be reconstructible from known data points and error specifications.

Predictions:

Given these inputs, one can, in principle, immediately calculate expectation values of any physics quantity \mathcal{O} as

$$\langle \mathcal{O} \rangle = \int d\{A\} \prod_a P_{\text{exp}}^a(\{x_o(A)\}|\{x_e\}) \times \mathcal{O}(A), \quad (67)$$

as well as the associated probability distribution $P_{pdf}(\mathcal{O}_t)$, which contains all information about the uncertainties on \mathcal{O} due to PDFs. Here $\{x_o(A)\}$ denotes the theoretical model values in place of $\{x_t\}$, $\{A\}$ denotes PDF parameters, $\int d\{A\}$ implies an integration over the entire PDF parameter space, and “ a ” labels the experiments included in the analysis.

In this purist of forms, there is no need to “fit” the experiments with PDF sets at all; the experimental response functions provide the weighting factor in the integration over *all possible* PDFs. The need for fitted PDFs only comes in at the technical level, when one wishes to make the functional integration $\int d\{A\}$ more practical (e.g. feasible) by replacing it with a discrete sum over an ensemble of PDF sets $\{A_i\}$ weighed according to a probability distribution determined by the experiments.

PDF Fits

To put it in another way, PDF fits correspond to “Unweighing of PDF integration with respect to a set of experiments”. With such an ensemble of PDFs, the functional integration in Eq. (67) is replaced by an ensemble average

$$\int d\{A\} \prod_a P_{\text{exp}}^a(\{x_o(A)\}|\{x_e\}) \longrightarrow \sum_i$$

such that: $\langle \mathcal{O} \rangle = \sum_i \mathcal{O}(A_i)$

where $\{A_i; i = 1, \dots, N\}$ represents the N sets of PDFs in the ensemble which are distributed according to the constraints imposed by the experiments.

Practical problems:

This program has been pursued by Giele *et al.*⁵⁰ Although the principle is clearly sound, it faces two serious problems for global QCD analysis in the real world.

- Few real experiments satisfy the axiom promulgated above as essential for this approach, hence are admissible for the analysis. For most experiments, the input response function $P_{\text{exp}}(\{x_t\}|\{x_e\})$, or its equivalent, either do not exist; or, when they are constructed from published errors, appear to be inconsistent (e.g. the χ^2 value far exceed the number of data points for any candidate theory);
- When the few admissible experiments are included in a global analysis, they appear to be incompatible with each other, i.e. their response functions have little overlap.

Thus, in this ideal approach, the global analysis is reduced in practice to a number of distinct, apparently incompatible, single- or double-experiment analyses. In addition, the ensemble approach is extremely costly in computing resources. In order to get reliable estimates, a benchmark number of $N = 100,000$ is often mentioned. This is clearly not practical for usual applications. But a much smaller number, say $N = 100$, would undercut the efficacy of the statistical approach. In practice, it would be very cumbersome even to have to carry out calculations with 100 sets of PDFs in each application!

The practical approach

The dilemma exposed by the idealized approach shows that, in any realistic global analysis effort, one must be flexible in seeking ways to deal with real world experimental errors which do not satisfy textbook axioms. This is a problem routinely faced in complex experimental error assessments, as well as in many global analysis efforts such as in the PDG project.⁵¹

Several efforts have been made to address the practical problems. The first such attempts^{46,52} focused on DIS experiments for which more complete error information are available. We outline here a recently proposed three-step procedure,^{53,54,55} which emphasizes preserving the *global* nature of the analysis by retaining all the relevant experimental constraints used in conventional global analysis, such as MRST and CTEQ. The procedure consists of:

- (i) using the effective global χ_g^2 function, Eq. (66), one obtains a global minimum (the “standard fit” S_0) as in conventional global analysis; then, one obtains additional sets of PDFs $\{S_i, i = 1, \dots, n\}$ in the vicinity of the minimum according to some criteria (cf. below for specifics), as “alternate hypotheses” to the true PDFs;
- (ii) one assesses the likelihood of these alternate hypotheses with respect to the individual experiments by utilizing the full statistical information on the errors for each experiment, using *relative probabilities* with respect to the standard set in the calculation; and
- (iii) one then combines this collection of uncertainties with respect to single experiments into an estimated *global uncertainty* for either physically measurable quantities, or the PDF parameters themselves.

In a world with perfect experimental errors, this procedure would yield results similar to those of the conceptually simpler “ideal approach” described above. In practice, this method by-passes the difficulties which prevent the realization of the latter by breaking the procedure into three manageable steps; and by using the relative, rather than the absolute, probability in step (ii).

Two complementary schemes were proposed to generate the alternative hypotheses $\{S_i, i = 1, \dots, n\}$: one, the Lagrange multiplier method, emphasizes accuracy for specific physical predictions; the other, the Hessian method, emphasizes generality in its applicability to all applications. Both schemes begin with the effective χ_g^2 function and the standard set S_0 mentioned in step (i).

Lagrange Multiplier Method

Let X be a particular physical quantity of interest, which depends on the PDFs. The best estimate (or prediction) of X is $X_0 = X(S_0)$. To assess the uncertainty of the predicted value for X , one first determines how the minimum of χ_g^2 increases, *i.e.*, how the quality of the fit to the

global data set decreases, as X is moved away from the best estimate X_0 . This is done^{53,55} by introducing the Lagrange multiplier variable λ , and minimizing the new function

$$\Psi(\lambda, A) = \chi_g^2(A) + \lambda(X(A) - X_0) \quad (68)$$

with respect to the PDF parameters $\{A_i\}$ for fixed values of λ . For a given value of λ , the minimum of $\Psi(\lambda, A)$ yields a set of parameters $\{A_{\min}(\lambda)\}$ that lead to the pair $\{\chi_g^2(\lambda), X(\lambda)\}$. $\chi_g^2(\lambda)$ represents the lowest achievable χ_g^2 for the global data sets if X takes the value $X(\lambda)$, taking into account all possible PDFs in the *full n dimensional PDF parameter space* represented by $\{A_j\}$. By repeating the calculation many times with different choices of λ , one obtains the dependence of χ_g^2 on X , i.e. the function $\chi_g^2(X)$.

One can obtain the maximum range of allowed values of X , say ΔX , for a given tolerance of the goodness of fit $\Delta\chi_g^2 = \chi_g^2 - \chi_0^2$ by, say, reading the numbers off a graph of χ_g^2 vs. X .

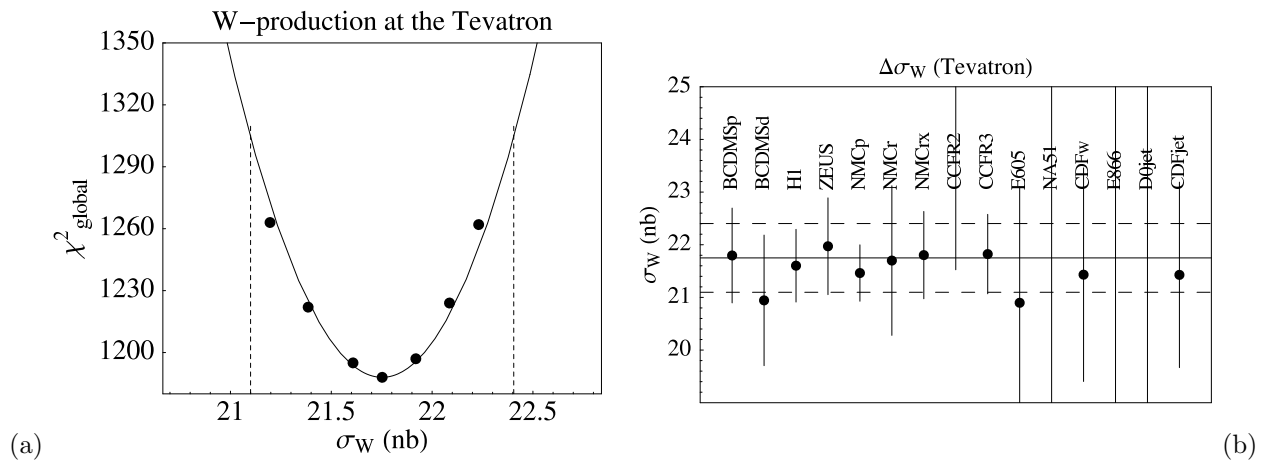


Figure 41: (a) Minimum χ_g^2 versus σ_W ; (b) 90% error bars for the individual experiments. The dashed lines are estimated bounds of the global uncertainty explained in the text.

This is illustrated for the case of W production cross section σ_W at the Tevatron, in Fig. 41a. The points on Fig. 41a are the results of constrained fits with various values of the Lagrange multiplier λ . The solid curve is a quadratic fit to the points to provide a smooth representation of the continuous function $\chi_g^2(X)$. One can see that the fits follow closely an expected parabolic behavior around the minimum. This method is independent of any approximations associated with functional dependence of $\chi_g^2(A)$ and $X(A)$ on the PDF parameters $\{A_i\}$.

The effective χ_g^2 function, unlike an ideal χ^2 function, does not have *a priori* quantitative statistical significance. To assess the uncertainty on X , one goes to step (ii) of the procedure above. one selects points $\{S_m\}$ on the solid curve in Fig. 41a, each representing a PDF set, and regard them as alternate hypotheses to the true PDF set. One then assesses the likelihood of these alternate hypotheses with respect to the individual experiments by utilizing the full error information available. At the individual experiment level, these error estimates are meaningful. The result on σ_W at the Tevatron is summarized in Fig. 41b.⁵⁵

The last step is to combine the individual errors into a global measure of uncertainty of σ_W . One notes that the ranges shown by the error bars in Fig. 41b are not errors determined independently by each experiment; rather they represent the allowed ranges of *constrained fits to the global data sets* $\{S_m\}$ imposed by individual experiments. Based on this figure, one estimates the global uncertainty band, shown by the dashed lines in the figure. In the case of σ_W for the Tevatron, the

percentage error is 3%. These can be turned into an effective “tolerance” value for $\Delta\chi_g^2$ of ~ 100 by Fig. 41a. For LHC, one obtains 5-6% uncertainty, which corresponds to the same $\Delta\chi_g^2$.

Error Matrix Method

We now turn to the more conventional error matrix approach to study uncertainties of the PDFs, as represented by the parameters $\{A_i\}$. To see that the standard method using the effective global χ^2 function makes sense, Fig. 42a shows the distribution of fluctuations $((N_n D_{nI} - T_{nI}(A))/\sigma_{nI}^D)$ in Eq. (66) for all data used in such an analysis. Indeed, a normal Gaussian distribution with no adjustable parameter is seen. This lends some confidence to the approach. The (in principle) straightforward method, however, encounters some serious technical (numerical) difficulties when applied to global QCD analysis, because of complexities mentioned earlier. The main problem is that eigenvalues of the Hessian matrix vary by 5-6 orders of magnitude in most choices of PDF parameters, as shown in Fig. 42b. The highly anisotropic behavior of the χ_g^2 function, as well as non-smooth behavior of the theory values $T_I(A)$ make conventional general purpose programs inadequate in providing physically sensible error estimates. This problem has been overcome with a newly developed iterative method for calculating the Hessian.^{53,54}

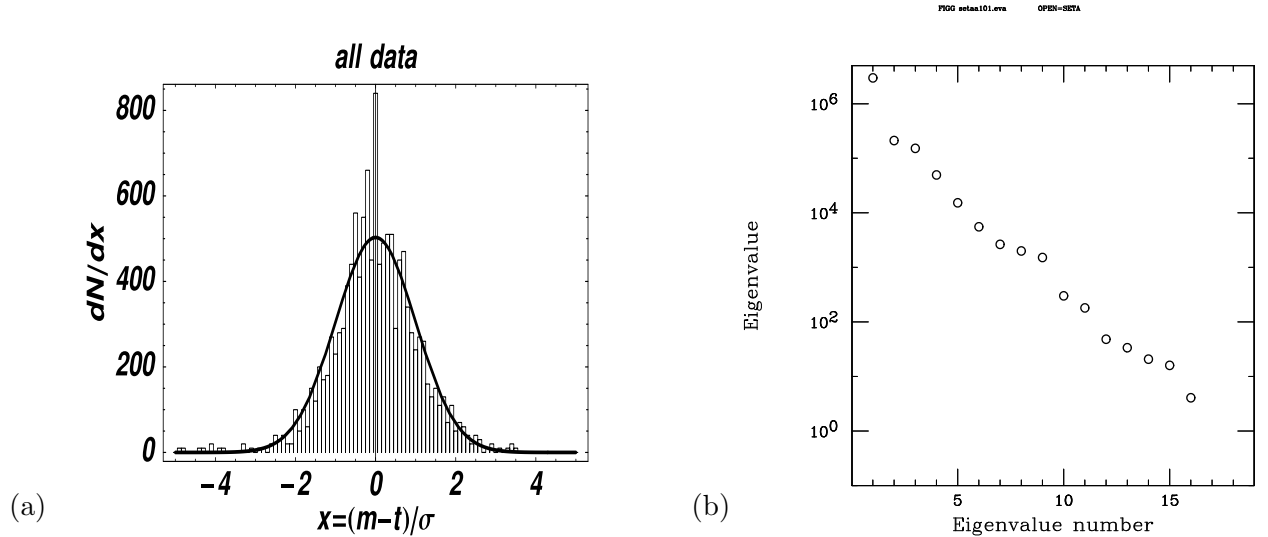


Figure 42: (a) Histogram of fluctuations (measurement - theory)/error for all data points; (b) variation in the order of magnitude of the eigenvectors of the Hessian.

The basic assumption of the error matrix approach is that χ^2 can be approximated by a quadratic expansion in the fit parameters $\{A_i\}$ near the global minimum. It is true if the variation of the theory values T_I with $\{A_i\}$ is approximately linear near the minimum. Letting $\Delta\chi^2 = \chi^2 - \chi_0^2$, one obtains

$$\Delta\chi^2 = \frac{1}{2} \sum_{i,j} H_{ij} (A_i - A_i^0)(A_j - A_j^0). \quad (69)$$

H_{ij} has a complete set of n orthonormal eigenvectors $\{v_{ik}\}$ with eigenvalues ϵ_k : $\sum_j H_{ij} v_{jk} = \epsilon_k v_{ik}$. The eigenvectors provide a natural basis to express arbitrary variations around the minimum. In terms of a new set of parameters defined with respect to the eigenvectors, $z_i = \sqrt{\frac{\epsilon_i}{2}} \sum_j (A_j - A_j^0) v_{ji}$, one obtains $\Delta\chi^2 = \sum z_i^2$, i.e. the surfaces of constant χ^2 are spheres in $\{z_i\}$ space, of radius $\sqrt{\Delta\chi^2}$.

Now consider any *physical quantity* X that depends on PDFs, hence the parameters $\{A_i\}$. In the neighborhood of the global minimum, assuming the first term of the Taylor-series expansion

of X gives an adequate approximation, the deviation of X from its best estimate is given by $\Delta X = X - X_0 \cong \sum_i X_i z_i$ where $X_i \equiv \partial X / \partial z_i$ are the components of the z -gradient evaluated at the global minimum, *i.e.*, at the origin in z -space. One can show that, for a given tolerance in $\Delta\chi^2$, the uncertainty of the physical quantity can be evaluated from the z -gradient vector components by the simple formula

$$(\Delta X)^2 = \Delta\chi^2 \sum_i X_i^2. \quad (70)$$

In practice, X_i is calculated by finite differences. Within the linear approximation, this equation can be reduced to an extremely compact and practical form

$$\Delta X = \sqrt{\sum_i (X(S_i^+) - X(S_i^-))^2} \quad (71)$$

where S_i^\pm are PDF sets which correspond to two points in the z parameter space specified by $\{z_j^\pm = \pm \delta_{ij} \sqrt{\Delta\chi^2/2}\}$. The squared uncertainty is proportional to $\Delta\chi^2$, the tolerance on the global χ^2 function. It can be determined by a procedure similar to the one described in the previous section, now applied to each of the eigenvector directions rather than to a specific variable. The overall tolerance can be an average over the eigenvector directions.

Thus, with the reliable calculation of the Hessian and its eigenvectors, one can obtain $2n + 1$ sets of PDFs, $\{S_0, S_i^\pm, i = 1, \dots, n\}$ (where n is the number of PDF parameters), from which the “user” can evaluate the uncertainty associated with any physical quantity X according to Eq. (71). Preliminary results on application to the W cross section show that they are consistent with those obtained by the Lagrange multiplier method.⁵³

We should point out that many other sources of uncertainty mentioned in the introduction are not yet included in this study. Therefore, the uncertainty estimates described here represent, at best, lower bounds. In any case, this summary is only meant to give a flavor of the very active developments being pursued in quantifying the uncertainties of PDFs and their predictions.

6.5 Global QCD analysis and the future of HEP

We emphasized throughout this review, particularly in Sec. 4.6, the multi-facet nature of the QCD parton model, which underlies its central role in HEP research. It is obvious that the quality of the predictions on standard model and new physics processes in future high energy physics programs depends critically on the reliability of our current knowledge of the parton structure of hadrons. On the other hand, to improve this knowledge, we also need experimental input from future experiments, providing physics constraints complementary to those currently available, to fill existing gaps and narrow the uncertainties. There is no better way to illustrate this unique role of the QCD parton model in HEP than concluding this review with a brief survey of this inter-dependence which represents really two sides of the same story.

Importance of PDFs for future HEP programs

All studies of standard model and new physics processes in future high energy physics programs involving hadrons rely on QCD parton model calculations based on currently known PDFs. We highlight a few, in relation to current work on global QCD analysis, which are particularly relevant for the physics programs of the next generation of hadron colliders: Tevatron Run II and LHC. An important fact about these colliders is that the W/Z vector bosons will be produced very copiously;

hence processes involving W/Z will hold center stage in a variety of studies, from the mundane to the adventurous.

Figure 43a shows the predicted W/Z cross sections as a function of energy, up to that of LHC; Fig. 43b shows the variation of the predicted cross sections at LHC for selected sets of MRST PDFs.⁴²

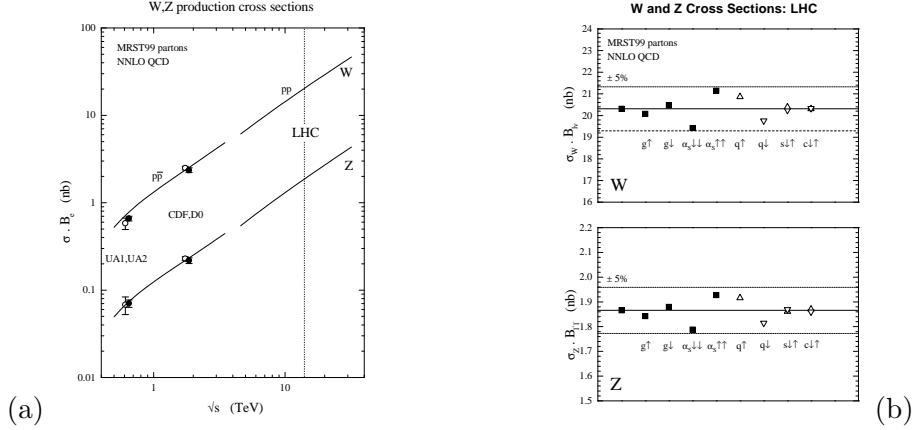


Figure 43: (a) W/Z total cross-sections vs. CM energy; (b) W/Z total cross-sections at the LHC for selected MRST99 PDFs. (Figures from Ref. [43].)

W/Z production as luminosity standard: Since W/Z cross sections can be measured well at the hadron colliders, they have been considered as good candidates as luminosity standards, provided the theoretical calculation is accurate enough.¹⁸ The theoretical uncertainty is dominated by that on PDFs. Fig. 43b explores the variation of the predicted cross sections at LHC using the conventional approach of comparing selected PDF sets. The range shown can be regarded, at best, as an educated guess. The systematic study of this uncertainty, exploring the full PDF space using the Lagrange multiplier method (cf. Fig. 41), gives a much more reliable estimate. The preliminary results for $\Delta\sigma_{W,Z}/\sigma_{W,Z}$ are $\sim 3\%$ at the Tevatron and $\sim 5 - 6\%$ at LHC.⁵³ These numbers turn out to be in agreement with the picture shown in Fig. 43b.

W -mass Measurement: The accurate determination of the W mass is one of the most anticipated measurements at the next generation of hadron collider physics programs, because of its key role in precision phenomenology in the standard model, with implications far beyond the SM. Again, the accuracy of the measurement depends critically on the uncertainties due to the PDF input. But no reliable estimates of this exist. The keen interest in quantifying PDF uncertainties described above has, to a significant part, been generated by the need to pin down their implication on the W mass measurement. Both the Lagrange multiplier and the Hessian methods can be extended to make quantitative estimates on the size of ΔM_W attributable to PDF uncertainties; but the work has only begun.

Signals and backgrounds for new particle searches: The searches for new particles (Higgs, supersymmetric particles and beyond) depend on reliable estimates of the promising signals and the potential backgrounds. Whereas accuracy may not be of primary concern in general, the relative sizes of the signal and background (which may depend on different initial state partons) do matter a great deal in some critical cases. Since many processes at high energies are sensitive to the gluon distribution, which is not well constrained currently, better determination of the PDFs, particularly the gluon, will have important impact on particle searches as well.

¹⁸Like QED processes have been used in lepton-lepton and lepton-hadron accelerators.

How can future experiments help global QCD analysis?

As reviewed in Sec. 6.4, many gaps and uncertainties still remain in our knowledge of the nucleon PDFs. The next generation hadron collider experiments can be very useful in filling these gaps. The main reason is, these new experiments can be considered as “ W/Z Factories”. Using these weak bosons as probes, along with final state real and virtual photons, the new precision QCD measurements will provide experimental constraints quite complementary to those from DIS experiments, in the global analysis of parton distributions. In this sense, the W/Z experiments will be the “DIS experiments” of the next decade. More specifically,

Precision PQCD phenomenology to study u, d, \bar{u}, \bar{d} and G : Beyond the W/Z total cross sections and M_W measurement, there are a full range of precise measurements which will advance the determination of the dominant partons, especially with both $p\bar{p}$ and pp colliders: the rapidity distribution of W/Z $d\sigma_{W,Z}/dy$ (sensitive to u, d, \bar{u}, \bar{d} ; W/Z plus jet(s) (sensitive to G as well as u, d quark); direct photon (sensitive to G , less hindered by k_T broadening at high energies); ... etc.

Unique probe for $s/c/b$ quarks: We mentioned in Sec. 6.4 that current knowledge on $s(x), \bar{s}(x)$ is not conclusive, and on $c(x), b(x)$ is almost non-existent. The hadron collider experiments promise unique opportunities to clarify these situations. If it is possible to tag heavy particle final states in association with vector boson production, then the parton subprocesses depicted in Fig. 44 will enable the selective measurement of each of the $s/c/b$ distributions. In a realistic study, these simple “LO” processes must be considered along with “NLO” (quotations because of considerations discussed in Sec. 5.6) processes such as $gg \rightarrow W + s + c, \dots$ etc.⁵⁶ But those are details which needn’t concern us in this broad review.

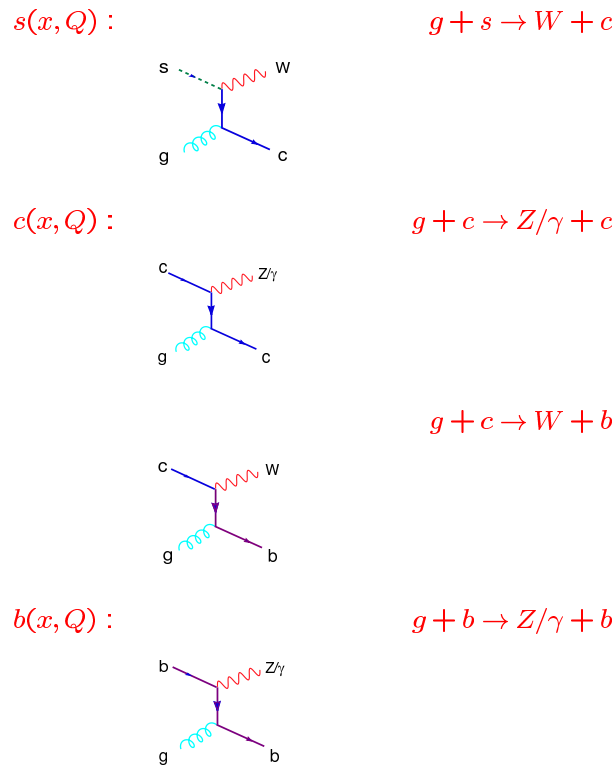


Figure 44: Parton subprocesses which may allow the measurement of the strange, charm and bottom quark distributions in the next generation of hadron colliders.

7 Epilogue

Perturbative QCD was where the amazing story of Quantum Chromodynamics begins. With this modest, but already quite unbelievably rich, beginning, let us see what the world of non-perturbative QCD holds for us.

Acknowledgement I would like to express appreciation to my colleagues John Collins, Joey Huston, Steve Kuhlmann, Fred Olness, Jon Pumplin, Dave Soper, George Sterman, Dan Stump, and other CTEQ members, for collaboration and for sharing their insights on QCD over many years. Thanks are particularly due to D. Soper for permission to use some material from his review lectures, Ref. 6, to J. Collins for numerous illuminating discussions which help shape many of the viewpoints reflected in this presentation, and to Pumplin and Stump for help with the manuscript.

Research on topics covered in this article has been supported by the National Science Foundation.

References

1. T. Muta, *Foundations Of Quantum Chromodynamics: An Introduction to perturbative methods in gauge theories*, 2nd Ed. (World Scientific, 1998).
2. George Sterman, *An Introduction To Quantum Field Theory* (Cambridge Univ. Press, 1993).
3. Michael E. Peskin and Daniel V. Schroeder, *An Introduction To Quantum Field Theory* (Addison-Wesley, 1995).
4. R.K. Ellis, W.J. Stirling, B.R. Webber, *QCD And Collider Physics*, (Cambridge Univ. Press, 1996).
5. R. Brock *et al.* [CTEQ Collaboration], “Handbook of perturbative QCD: Version 1.0,” *Rev. Mod. Phys.* **67**, 157 (1995).
6. D. E. Soper, in *The Strong Interaction, from Hadrons to Partons*, XXIV SLAC Summer Institute on Particle Physics Stanford, August 1996, edited by L. DePorcel (SLAC, Stanford, 1997) hep-ph/9702203.
7. G. Sterman, in *Theoretical advanced study institute in elementary particle physics*, TASI '95, Univ. of Colorado, Ed. by Davison E. Soper (World Scientific, 1996). hep-ph/9606312.
8. U. Aglietti, hep-ph/9705277.
9. L. R. Surguladze and M. A. Samuel, *Rev. Mod. Phys.* **68**, 259 (1996) [hep-ph/9508351].
10. Z. Kunszt and D. E. Soper, *Phys. Rev.* **D46**, 192 (1992).
11. G. Sterman and S. Weinberg, *Phys. Rev. Lett.* **39**, 1436 (1977).
12. Cf. Ref. 4, Sec. 3.3; also see Ref. 31.
13. S. Bethke, Lectures at the international Summer School *Particle Production Spanning MeV and TeV Energies*, Nijmegen, 1999. hep-ex/0001023.
14. K. Abe *et al.* [SLD Collaboration], *Phys. Rev.* **D51**, 962 (1995) [hep-ex/9501003].
15. J. C. Collins, D. E. Soper and G. Sterman, in *Perturbative Quantum Chromodynamics* Edited by A.H. Mueller (World Scientific, 1989).
16. P. Chiappetta, M. Greco, J. P. Guillet, S. Rolli and M. Werlen, *Nucl. Phys.* **B412**, 3 (1994) [hep-ph/9301254].
17. M. A. Aivazis, J. C. Collins, F. I. Olness and W. Tung, *Phys. Rev.* **D50**, 3102 (1994) [hep-ph/9312319].
18. J. C. Collins, *Phys. Rev.* **D58**, 094002 (1998) [hep-ph/9806259].

19. Cf. for instance, R. K. Ellis, H. Georgi, M. Machacek, H. D. Politzer and G. G. Ross, *Nucl. Phys.* **B152**, 285 (1979).
20. G. Curci, W. Furmanski and R. Petronzio, *Nucl. Phys. B* **175**, 27 (1980).
J. C. Collins and D. E. Soper, *Nucl. Phys. B* **194**, 445 (1982).
21. W. L. van Neerven and A. Vogt, *Phys. Lett.* **B490**, 111 (2000) [hep-ph/0007362].
22. T. Gehrmann, R. G. Roberts and M. R. Whalley, *J. Phys. G* **G25**, A1 (1999). A. M. Cooper-Sarkar, R. C. Devenish and A. De Roeck, *Int. J. Mod. Phys.* **A13**, 3385 (1998) [hep-ph/9712301].
23. A. D. Martin, R. G. Roberts, W. J. Stirling and R. S. Thorne, *Eur. Phys. J.* **C4**, 463 (1998) [hep-ph/9803445].
24. H. Contopanagos, E. Laenen and G. Sterman, *Nucl. Phys.* **B484**, 303 (1997) [hep-ph/9604313].
25. H. Li, *Phys. Lett.* **B454**, 328 (1999) [hep-ph/9812363].
S. Catani, M. L. Mangano, P. Nason, C. Oleari and W. Vogelsang, *JHEP* **9903**, 025 (1999) [hep-ph/9903436].
E. Laenen, G. Sterman and W. Vogelsang, hep-ph/0010080.
26. J. Huston, E. Kovacs, S. Kuhlmann, H. L. Lai, J. F. Owens and W. K. Tung, *Phys. Rev.* **D51**, 6139 (1995) [hep-ph/9501230].
27. L. Apanasevich *et al.*, *Phys. Rev.* **D59**, 074007 (1999) [hep-ph/9808467].
28. G. C. Blazey *et al.*, in Ref. 31, hep-ex/0005012.
29. S. Catani *et al.*, in *Proceedings of Workshop on Physics at TeV Colliders*, Les Houches, France, 7-18 Jun 1999. hep-ph/0005114.
30. S. Catani *et al.*, in *Proceedings of LHC Workshop: Standard model physics (and more) at the LHC*, Geneva 1999 (to be published) hep-ph/0005025.
31. *Proceedings of the Physics at RUN II: QCD and Weak Boson Physics Workshop* Batavia, Illinois, 4-6 Nov 1999 (to be published).
32. P. Nason, S. Dawson and R. K. Ellis, *Nucl. Phys.* **B327**, 49 (1989). E. Laenen, S. Riemersma, J. Smith and W. L. van Neerven, *Nucl. Phys.* **B392**, 162 (1993).
33. R. S. Thorne and R. G. Roberts, *Phys. Rev.* **D57**, 6871 (1998) [hep-ph/9709442].
34. A. Chuvakin, J. Smith and W. L. van Neerven, *Phys. Rev.* **D61**, 096004 (2000) [hep-ph/9910250].
35. J. Amundson, C. Schmidt, W. Tung and X. Wang, *JHEP* **0010**, 031 (2000) [hep-ph/0005221].
36. B. W. Harris and J. Smith, *Nucl. Phys.* **B452**, 109 (1995) [hep-ph/9503484].
37. J. Breitweg *et al.* [ZEUS Collaboration], *Eur. Phys. J.* **C12**, 35 (2000) [hep-ex/9908012].
38. S. Frixione, M. L. Mangano, P. Nason and G. Ridolfi, in *Heavy Flavours II*, Edited by A.J. Buras and M. Lindner. World Scientific, 1998. [hep-ph/9702287].
39. F. I. Olness, R. J. Scalise and W. Tung, *Phys. Rev.* **D59**, 014506 (1999) [hep-ph/9712494].
M. Cacciari, M. Greco and P. Nason, *JHEP* **9805**, 007 (1998) [hep-ph/9803400].
40. J. C. Collins and R. K. Ellis, *Nucl. Phys.* **B360**, 3 (1991).
41. H. L. Lai *et al.* [CTEQ Collaboration], *Eur. Phys. J.* **C12**, 375 (2000) [hep-ph/9903282].
42. A. D. Martin, R. G. Roberts, W. J. Stirling and R. S. Thorne, *Eur. Phys. J.* **C14**, 133 (2000) [hep-ph/9907231].
43. A. D. Martin, R. G. Roberts, W. J. Stirling and R. S. Thorne, hep-ph/0007099.
44. M. Gluck, E. Reya and A. Vogt, *Eur. Phys. J.* **C5**, 461 (1998) [hep-ph/9806404]; and *Z. Phys.* **C67**, 433 (1995).
45. P. Aurenche, M. Fontannaz, J. P. Guillet, B. Kniehl, E. Pilon and M. Werlen, *Eur. Phys. J.*

- C9**, 107 (1999) [hep-ph/9811382].
46. M. Botje, *Eur. Phys. J.* **C14**, 285 (2000) [hep-ph/9912439].
 47. V. Barone, C. Pascaud and F. Zomer, *Eur. Phys. J.* **C12**, 243 (2000) [hep-ph/9907512].
 48. S. Kumano, *Phys. Rept.* **303**, 183 (1998) [hep-ph/9702367].
 49. S. Kuhlmann *et al.*, *Phys. Lett.* **B476**, 291 (2000) [hep-ph/9912283].
 50. W. T. Giele and S. Keller, *Phys. Rev.* **D58**, 094023 (1998); and contribution to Ref. 31: L. de Barbaro *et al.*, hep-ph/0006300.
 51. D. E. Groom *et al.*, *Eur. Phys. J.* **C15** (2000) 1.
 52. S. Alekhin, *Eur. Phys. J.* **C10**, 395 (1999) [hep-ph/9611213]; and contribution to Ref. 30.
 53. J. Pumplin, D. Stump, and W.-K. Tung, [hep-ph/0008191]; contribution to Ref. 31: L. de Barbaro *et al.*, hep-ph/0006300; and contribution to *Proceedings of ICHEP conference* (by W.K. Tung), Osaka, Japan, August, 2000 (to be published).
 54. J. Pumplin *et al.*, hep-ph/0101032 (to be published).
 55. D. Stump *et al.*, hep-ph/0101051 (to be published).
 56. W. T. Giele, S. Keller and E. Laenen, *Phys. Lett.* **B372**, 141 (1996) [hep-ph/9511449].